MIGRATION AND INVERSION OF MAGNETIC AND MAGNETIC GRADIOMETRY DATA

by

Hongzhu Cai

A thesis submitted to the faculty of
The University of Utah
in partial fulfillment of the requirements for the degree of

Master of Science

in

Geophysics

Department of Geology and Geophysics

The University of Utah

May 2012

The University of Utah Graduate School

STATEMENT OF THESIS APPROVAL

The thesis of **Hongzhu Cai**

has been approved by the following supervisory committee members:

Michael S. Zhdanov	, Chair	**01/30/2012** Date Approved
Michael S. Thorne	, Member	**01/30/2012** Date Approved
Le Wan	, Member	**01/30/2012** Date Approved

and by **D. Kip Solomon** , Chair of

the Department of **Geology and Geophysics**

and by Charles A. Wight, Dean of The Graduate School.

ABSTRACT

A new method of rapid interpretation of magnetic field and magnetic tensor field data is introduced. It is based on ideas of potential field migration, which extend to the case of the potential field the general principles of seismic and electromagnetic migration. Potential field migration represents a direct integral transformation of the observed magnetic fields into a subsurface susceptibility distribution, which can be used for interpretation or as an a priori model for subsequent 2-D or 3-D regularized inversion. Potential field migration is very stable with respect to noise in the observed data because the transform is reduced to the downward continuation of a function analytical everywhere in the lower half-plane.

Following recent advances in SQUID technology, full tensor magnetic gradiometry (FTMG) is emerging as a practical exploration method. We indroduce 3-D regularized focusing inversion for FTMG data. Our model studies show that inversion of magnetic tensor data can significantly improve resolution compared to inversion of magnetic vector data for the same model.

In this thesis, we present case studies for the imaging of GETMAG magnetic tensor data acquired over a magnetite skarn at Tallawang, Australia using potential field migration technique, 3-D regularized smooth inversion and 3-D regularized focusing inversion. Our results fit very well with the known geology. Three dimensional regularized focusing inversion produces much more compact image than 3-D regularized

smooth inversion. Two dimensional migration shows the advantage of faster image than both 3-D regularized smooth inversion and 3-D regularized focusing inversion.

To my parents

CONTENTS

ACKNOWLEDGEMENTS

I would like to express my deep gratitude to my graduate advisor Michael Zhdanov, for his support and guidance in my research and graduate study. I have benefited a lot from his expertise in geophysics and mathematics. Without his help during my study and research, I could not have finished my research.

Special acknowledgements to Dr. Glenn Wilson from TechnoImaging for his help with the case study of my paper, Dr. Gribenko and Dr. Liu for useful discussion of this study. I'm also grateful to my supervisory committee members, Dr. Le Wan and Professor Michael Thorne.

I'm deeply thankful to Consortium for Electromagnetic Modeling and Inversion (CEMI) which provides an excellent environment for study and research. In the CEMI student office, I met some great friends to work and study together. They gave me a lot of suggestions during my study here and always encouraged me to achieve more in my life.

Finally, I would like to give my special thanks to my parents for their continuous support and encouragement of my study.

CHAPTER 1

INTRODUCTION

Magnetic vector data measured from orthogonal fluxgate magnetometers are dominated by the Earth's background magnetic field, and are thus very sensitive to instrument orientation. Given the relative instabilities of airborne platforms, cesium vapor magnetometers have been preferred as they directly measure the total magnetic intensity (TMI) and are insensitive to instrument orientation. Total field gradients measured from two (or more) cesium vapor magnetometers are still very sensitive to system orientation, and are not "true" potential fields. As such, most magnetic inversion methods are based on TMI data (e.g., Li and Oldenburg, 1996, 2003; Portniaguine and Zhdanov, 2002). However, vector components derived from TMI are often less susceptible to error than their direct measurement from airborne platforms (Schmidt and Clark, 1998) but are rarely used for inversion.

As discussed by Schmidt and Clark (2006), direct measurement of the magnetic tensors are advantageous for a number of reasons. First, magnetic tensors are relatively insensitive to instrument orientation since magnetic gradients arise largely from localized sources and not the Earth's background field or regional trends. Second, magnetic tensor data obviate the need for base stations and diurnal corrections. Third, magnetic tensors contain directional sensitivities which are advantageous for the interpretation of under-

sampled surveys. And finally, remanent magnetization, including the Koenigsberger ratio, can be recovered from magnetic tensor data.

Recently, magnetic gradiometers based on superconducting quantum interference devices (SQUIDs) have been developed and commercially deployed for geophysical surveying (e.g., Schmidt et al., 2004; Stolz et al., 2006; Rompel, 2009). Given that the primary application of magnetic gradiometry has been the real-time tracking of moving objects from stationary instruments (or stationary objects from moving instruments), magnetic tensor data are usually interpreted by some manner of Euler deconvolution (e.g., Wynn et al., 1975). While these methods may provide information about the sources, it is not immediately obvious how that information can be used for constructing a model of the spatial distribution of magnetic susceptibility. In this thesis, we present an alternative approach, which is based on an extension of the idea of 2-D potential field migration as originally introduced by Zhdanov (2002). This new approach provides a rapid method for direct transformation of the observed magnetic vector or tensor data into a spatial susceptibility distribution. This work is analogous to Zhdanov et al. (2010), where potential field migration for gravity gradiometry has been developed. The advantage of potential field migration for geophysical applications is that it does not require any a priori information about the type of the sources.

Mathematically, migration is described by an action of the adjoint operator on the observed data. This concept has been long developed for seismic wavefields (e.g., Schneider, 1978; Berkhout, 1980; Claerbout, 1985), and was also developed for electromagnetic fields (Zhdanov, 1988, 2002, 2009), where the adjoint operators manifest themselves as the (backward) propagation of seismic or electromagnetic fields in reverse

time. When applied to potential fields, migration manifests itself as a special form of downward continuation of the potential field and/or its gradients. A downward continuation is applied to the migration field, which is obtained by relocating the sources of the observed field into the upper half-space as mirror images of the true sources. As a result, the migration field is described by the function analytical everywhere in the lower half-plane. Contrary to conventional downward continuation of the potential field, downward continuation of the migration field is away from the mirror images of the sources. Therefore, migration is a stable transform, similar to upward continuation of the magnetic anomalies. At the same time, the migration field does contain remnant information about the original source distribution, which is why it can be used for subsurface imaging.

In this thesis, we provide a detailed exposition of potential field migration theory as applied to complex intensities of magnetic vector and tensor fields. We also apply the magnetic field migration to GETMAG magnetic tensor data acquired over a magnetite skarn at Tallawang, Australia.

As we presented above, migration of magnetic vector field and magnetic tensor field data is a stable transformation to obtain the distribution of underground magnetic susceptibility. However, one disadvantage of this method for interpreting magnetic data is that the magnetic susceptibility distribution obtained from migration may not provide the accurate prediction of the observed data. In other words, the migration magnetic susceptibility represents just an image of the true magnetic susceptibility. In order to recover true distribution of susceptibility, we still need to apply the regularized inversion, which is usually based on the minimization of Tikhonov parametric functional. Based on

the traditional regularized inversion, we will introduce focusing inversion, which can generate compact and realistic images of the subsurface geology with sharp geological boundaries.

In this thesis, several 3-D magnetic models are presented for traditional smooth inversion and regularized focusing inversion. In order to make our inversion much closer to the real geology, we considered the effect of topography into inversion. In the thesis, we also presented some models of 3-D inversion with topography. Synthetic model studies show that our inversion algorithms also work well in the case of complicated topography. We applied both 3-D regularized smooth inversion and 3-D regularized focusing inversion to the Tallawang magnetic tensor data. All the images we have generated using migration, 3-D smooth inversion, and 3-D focusing inversion fit well to the known geology. Migration technique has the advantage of saving computation time. Three dimensional regularized focusing inversion produces much more focused images, which are much closer to the real geology than both 3-D regularized smooth inversion and migration results.

CHAPTER 2

MIGRATION OF INTENSITY OF MAGNETIZATION

In this section we will introduce the migration theory considering remanent magnetization. Usually, in the process of interpreting magnetic data in geophysics, we assume that the anomalous magnetic field is caused by inducing magnetic field which means that the direction of intensity of magnetization is known. If we do not consider remanent magnetization, the direction of intensity of magnetization is the same as the inducing magnetic field. In some special cases, where the remanent magnetization is too strong, the direction of intensity of magnetization will be different from the inducing magnetic field. In this case, we need to recover the information of intensity of magnetization. Subsection one introduces complex intensity of magnetization. Subsection two introduces complex magnetic potential, complex magnetic field and complex magnetic tensor field. Subsections three and four introduce adjoint operator and their relationship with complex magnetic potential, magnetic field and tensor field. Subsection five introduces migration image of intensity of magnetization for complex magnetic potential, complex magnetic field and complex tensor field. Some model studies are presented in subsection six.

2.1 Complex intensity of magnetization

We consider a model with a two-dimensional (2-D) distribution of magnetic masses with intensity of magnetization , $\mathbf{I}(x,z)=(I_x(x,z),\ I_z(x,z))$, within a domain, Γ (Figure 2.1). According to Zhdanov (1988), the magnetic field can be expressed as follows:

$$\mathbf{H}(x',z') = 2\widetilde{\nabla} \iint \mathbf{I}(x,z)\cdot\frac{(x-x')\mathbf{d_x}+(z-z')\mathbf{d_z}}{(x-x')^2+(z-z')^2}, \tag{2.1}$$

where $\widetilde{\nabla}$ denotes a 2-D differential operator, $\widetilde{\nabla} = (\partial/\partial x\ , \partial/\partial z\ )$, and $\mathbf{d}_x$, and $\mathbf{d}_z$ are the unit basis vectors of the Cartesian system of coordinates.

We can define the complex intensity of magnetization as follows:

$$I(\ ) = I_x(x,z) + iI_z(x,z) \tag{2.2}$$

where $=x+iz$ is a complex variable.

2.2 Complex magnetic potential, complex magnetic field and magnetic tensor field

The complex intensity of a plane magnetic field can be defined, according to Zhdanov (1988), as follows:

$$H(\ ') = -H_x(x,z) + iH_z(x,,z) = A^H(I) = -2\iint_\Gamma \frac{1}{(\ -\ ')^2} I(\ )\,ds \tag{2.2}$$

where A^H denotes the forward modeling operator for a magnetic field.

In accordance with Zhdanov (1988), function $H(\zeta')$ satisfies the following equation:

$$\frac{\partial}{\partial\ ^*}H(\zeta') = 2I(\ ) \tag{2.3}$$

The magnetic field can be expressed by the magnetic potential $U(\mathbf{r})$ as:

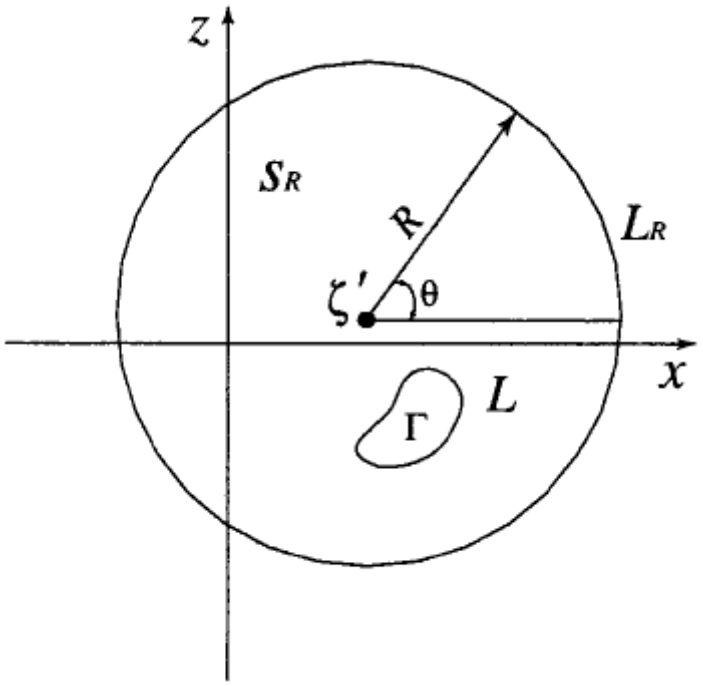

Figure 2.1. A complex plane describing a 2-D magnetic problem。

$$H(x,z) = \widetilde{\nabla} U(x,z). \tag{2.4}$$

We can introduce a complex magnetic potential $U(\zeta)$ as:

$$H(\ ') = \frac{\partial}{\partial'} U(\ '). \tag{2.5}$$

From formula (2.2) and (2.5), we have at once

$$U(\ ) = A^U(I) = -2 \iint \ \frac{1}{\_} I(\ ) ds. \tag{2.6}$$

where A^U denotes the forward modeling operator for a magnetic potential field.

Note that a complex magnetic potential U can be expressed by its real, U_r and imaginary, U_i, parts as

$$U(\ ') = A^U(I) = -2 \iint_\Gamma \ \frac{1}{\_'} I(\ ) ds = U_r + iU_i, \tag{2.7}$$

In the above formula, the real part and imaginary part of complex magnetic potential is given as follows:

$$U_r(x',z') = -2 \iint_\Gamma \ \frac{(x-x')I_x+(z-z')I_z}{(x-x')^2+(z-z')^2} d, \tag{2.8}$$

and

$$U_i(x',z') = -2 \iint_\Gamma \ \frac{(x-x')I_z-(z-z')I_x}{(x-x')^2+(z-z')^2} ds. \tag{2.9}$$

We will use formula (2.8) and formula (2.9) for modeling synthetic magnetic potential data.

According to formula (2.2), after take some algebra, one can find the explicit expression for magnetic vector components H_x and H_z as follows:

$$H_x(x',z') = -2 \iint_\Gamma \ \frac{I_x[(x-x')^2-(z-z')^2]+2I_z(x-x')(z-z')}{[(x-x')^2+(z-z')^2]^2} ds, \tag{2.10}$$

$$H_z(x',z') = -2 \iint_\Gamma \ \frac{I_z\left[(x-x')^2-(z-z')^2\right]-2I_x(x-x')(z-z')}{[(x-x')^2+(z-z')^2]^2} ds. \tag{2.11}$$

Formula (2.10) and (2.11) will be used to model synthetic magnetic vector data in 2-D case.

The second spatial derivatives of the magnetic potential $U(\mathbf{r})$,

$$H_{\alpha\beta} = \frac{\partial^2}{\partial\alpha\beta} U(\mathbf{r}),\ \alpha, \beta = x, z, \tag{2.12}$$

forms a symmetric magnetic tensor:

$$\widehat{\mathbf{H}} = \begin{bmatrix} H_{xx} & H_{xz} \\ H_{zx} & H_{zz} \end{bmatrix}, \tag{2.13}$$

where:

$$H_{\alpha\beta} = \frac{\partial H_\alpha}{\partial \beta},\ \alpha, \beta = x, z. \tag{2.14}$$

Let us define the complex intensity of the magnetic tensor field, $H_T(\ )$, as a complex derivative of the complex intensity of the magnetic field $H(\ )$, introduced by equation (2.2):

$$H_T(\ ) = \frac{\partial H(\ )}{\partial} = \frac{1}{2}\left(\frac{\partial}{\partial x} - i\frac{\partial}{\partial z}\right) H(\ ). \tag{2.15}$$

By substituting equation (2.2) into (2.15), we find that:

$$H_T(\ ) = H_{zz}(x, z) + iH_{zx}(x, z). \tag{2.16}$$

In the last formula we take into account the symmetry of magnetic tensor, H_{zx}=H_{xz}, and the fact that the magnetic potential outside the mass should satisfy Laplace's equation:

$$H_{xx}(x, z) + H_{zz}(x, z) = 0. \tag{2.17}$$

According to equation (2.15), we have the following expression for the complex intensity of the magnetic tensor field:

$$H_T(\ ') = A^T(I) = -2\iint_\Gamma \frac{1}{(\ - \ ')^3} I(\ )\, ds, \qquad \notin \Gamma, \tag{2.18}$$

where A^T denotes the corresponding forward modeling operator in terms of the complex intensity of magnetization. As for the complex magnetic field, we can find the explicit expression for H_{xx} and H_{zz} components as follows:

$$H_{zz}(x',z') = -4\iint_{\Gamma} \frac{I_x[(x-x')^3-3(x-x')(z-z')^2]+I_z[3(x-x')^2(z-z')-(z-z')^3]}{[(x-x')^2+(z-z')^2]^3} ds, \quad (2.19)$$

and

$$H_{zx}(x',z') = -4\iint_{\Gamma} \frac{I_z\left[(x-x')^3-3(x-x')(z-z')^2\right]-I_x[3(x-x')^2(z-z')-(z-z')^3]}{[(x-x')^2+(z-z')^2]^3} ds. \quad (2.20)$$

The last two formulas will be used to model synthetic magnetic tensor field data in 2-D case.

2.3 Adjoint operators for complex magnetic potential, complex magnetic field and complex magnetic tensor field

Adjoint operator plays a pivotal role in migration theory. The closed form of the adjoint operator for a complex magnetic field was first developed by Zhdanov (2002). For completeness, we will summarize his derivation and will subsequently extend it to complex magnetic potential and complex magnetic tensor field.

Let's assume that we have the observed magnetic potential, $U(\zeta')$ along a line of observation L. The domain, Γ, which is filled with the masses generating the observed field, is located in the lower half-plane.

We introduce a complex Hilbert space D of data (magnetic field, magnetic tensor field and/or magnetic potential) with the metric:

$$(f,U)_D = \int_L f(\ )U^*(\ )d\ ;\ f,g\ \in D, \quad (2.21)$$

and a complex Hilbert space *M* of models (function $I(\zeta)$) with the metric:

$$(J,I)_M = \iint_\Gamma J(\ )I^*(\ )ds;\ J,I \in M. \tag{2.22}$$

Let us find an explicit form of the adjoint operator for the magnetic potential problem:

$$(A^U(I),f)_D = (I,A^{U\star}(f))_M \tag{2.23}$$

Using the definitions (2.21) and (2.22) of the inner products and expression (2.6) for the forward operator, we can rewrite formula (2.23) as:

$$(A^U(I),f)_D = \int_L A^U(I)\,f^*dx = -\iint I(\ )\left[2\int_{-} \frac{f^*(x')}{-x'}dx'\right]ds =$$

$$-(I,2\int_{-\infty}^{\infty}\left[\frac{f^*(x\prime)}{-x'}\right]^* dx')_M, \tag{2.24}$$

where, as usual, the asterisk, *, means complex conjugate. Here, we consider a simple case that function *f* just changes with *x'* and *z'*=0. This assumption can be interpreted in geophysics as we do not consider topography and the measurement of the field is conducted in the surface.

By comparing formula (2.23) and (2.24), we see that:

$$(I,\left[A^{U\star}(f) + 2\int_{-\infty}^{\infty}\left[\frac{f^*(x\prime)}{-x}\right]^* dx'\right])_M = 0, \tag{2.25}$$

where the star $\star$ means adjoint operator.

Equation (2.25) holds for any *I*, for example, for

$$I = A^{U\star}(f) + 2\int_{-\infty}^{\infty}\left[\frac{f^*(x\prime)}{-x'}\right]^* dx'. \tag{2.26}$$

By substituting (2.26) into (2.25), we obtain

$$\| A^{U\star}(f) + 2\int_{-\infty}^{\infty}\left[\frac{f^*(x\prime)}{-x}\right]^* dx' \|^2 = 0. \tag{2.27}$$

From the last formula we find that the adjoint operator for magnetic potential problem, $A^{U\star}$, applied to some function *f(x')*, is given by the formula:

$$A^{U\star}(f) = -2\int_{-\infty}^{\infty}\left[\frac{f^*(x\prime)}{-x}\right]^* dx' = 2\int_{-\infty}^{\infty}\frac{f(x')}{x-^*}dx'. \quad (2.28)$$

Similarly, we can find the adjoint operator for magnetic field problem, $A^{H\star}$, applied to some function *f(x')*, is given by the formula:

$$A^{H\star}(f) = -2\int_{-} \frac{f(x')}{(-x)^2}dx'. \quad (2.29)$$

The adjoint operator for magnetic tensor field, $A^{T\star}$, applied to some function *f (x')*, is given by the formula:

$$A^{T\star}(f) = -4\int_{-\infty}^{\infty}\frac{f(x')}{(-x)^3}dx'. \quad (2.30)$$

2.4 Adjoint fields and their relationship with magnetic potential, magnetic field and tensor field migration

Let us analyze the result of applying the adjoint magnetic potential operator to a magnetic potential, U_Γ, observed on the *x* axis:

$$A^{U\star}U_\Gamma = -2\int_{-\infty}^{\infty}\left[\frac{U_\Gamma^*(x\prime)}{-x}\right]^* dx'. \quad (2.31)$$

Let us study the physical meaning of the last equation. First, let us examine the last expression. First, let us examine the expression for U_Γ^*. According to equation (2.6), we can see that:

$$U_\Gamma^*(x') = -2\iint \frac{1}{^*-x}I^*(\ )ds = -2\iint_{\Gamma^*}\frac{1}{-x}I^*(\ ^*)ds = U_{\Gamma^*}(x'), \quad (2.32)$$

where $U_{\Gamma^*}(x')$ can be treated as the magnetic field of the magnetic masses located in domain Γ^*, which is a mirror image of domain Γ with respect to the x axis (Figure 2.2).

We will call $U_{\Gamma^*}(x')$ the adjoint magnetic potential. The complex intensity of magnetization $\tilde{I}(\ )$ within Γ^* is a complex conjugate mirror image of the magnetization distribution $I(\ )$ in Γ, i.e., $\tilde{I}(\ ) = I^*(\ ^*)$. Obviously, the adjoint magnetic potential U_{Γ^*} is an analytical function everywhere in the lower half-plane which can be expressed in equivalent form as:

$$U_{\Gamma^*}(\ ) = -2\iint_{\Gamma} \frac{1}{\tilde{\ }-\ } \tilde{I}(\tilde{\ })d\tilde{s}, \quad \notin \Gamma^*, \tag{2.33}$$

where $\tilde{\ } = \tilde{x} + i\tilde{z'} \in \Gamma^*$ is a variable of integration and $d\tilde{s} = d\tilde{x}d\tilde{z}$.

Consider Figure 2.2. Let $P+$ stand for the upper half-plane of a complex plane bounded by the real axis x, and P^- for the lower half-plane. We consider an arbitrary point $\in \Gamma$ and draw therefrom a circle of radius, R. That part of the real axis x that happens to lie inside the circle will be represented by b_R, while that part of the circle found inside P^- will be denoted by C_R. According to Cauchy integral formula, we have the following relationship:

$$U_{\Gamma^*}(\ ) = \frac{1}{2\pi i}\int_{bR,} \frac{U_{\Gamma^*}(\ ')}{'-\ } d\ ' + \frac{1}{2\pi i}\int_{CR,} \frac{U_{\Gamma^*}(\ ')}{'-\ } d\ ', \quad \in P^-, \tag{2.34}$$

where the integration over the closed contour $b_R \cup C_R$ is taken in the counter-clockwise direction. In particular, the integration over the segment b_R of the real axis is from right to left. Now, let radius R goes to infinity. The integral over semicircle CR wound become zeros as R tends to infinity. Therefore, equation (2.34) takes the following form:

$$U_{\Gamma^*}(\ ) = -\frac{1}{2\pi i}\int_{-\infty,}^{\infty} \frac{U_{\Gamma^*}(x')}{x'-\ } dx', \quad \in P^-, \tag{2.35}$$

where $U_{\Gamma^*}(x')$ is the magnetic field generated along the x axis by the magnetic masses

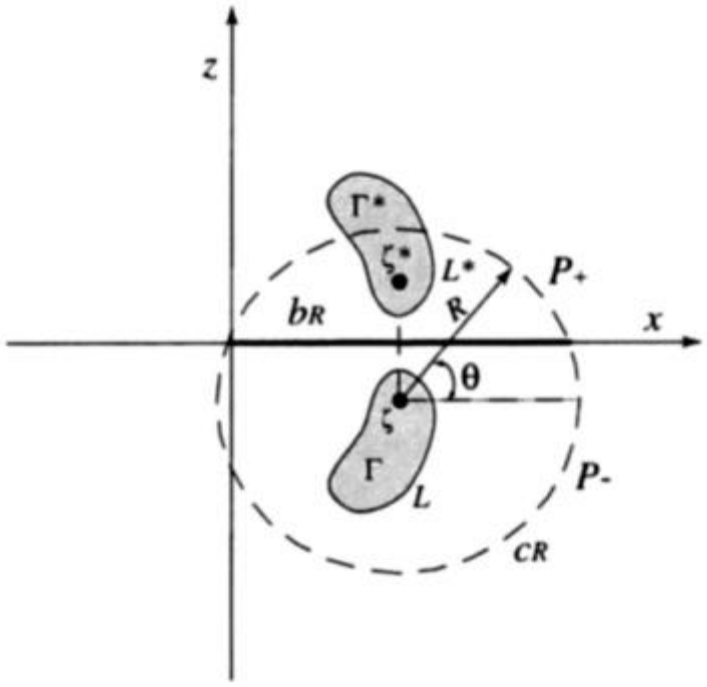

Figure 2.2. Definition of the adjoint magnetic potential, $\boldsymbol{U_{\Gamma^*}}$. The magnetic potential $\boldsymbol{U_{\Gamma^*}}$ is generated by the sources located in $\boldsymbol{\Gamma^*}$. The intensity of magnetization distribution within $\boldsymbol{\Gamma^*}$ is a mirror image of the intensity of magnetization distribution in .

located in domain Γ^*, and the minus sign arises because we have changed the direction of integration; it is now conducted from the left $(-\infty)$ to the right (∞). According to equation (2.32), we have the following relationship:

$$U_{\Gamma}^{*}(x') = U_{\Gamma^*}(x'). \tag{2.36}$$

As a result, equation (2.35) can be rewritten as follows:

$$U_{\Gamma^*}(\ ) = -\frac{1}{2\pi i}\int_{-}{}_{,}\frac{U_{\Gamma}^{*}(x')}{x-}dx\,, \quad \in P^{-}. \tag{2.37}$$

Taking into account equation (2.37), we can represent equation (2.31) in the following form:

$$A^{U\star}U_{\Gamma} = -4\pi i[U_{\Gamma^*}(\ )]^{*} \tag{2.38}$$

From the last formula, we can see that the application of the adjoint operator to an observed magnetic field is equivalent to take the analytical continuation of the adjoint magnetic field in the lower half-plane. Follow Zhdanov (2002), we will call this transformation a magnetic field migration, and use the notation:

$$U_{\Gamma}^{m}(\ ) = A^{U\star}U_{\Gamma}, \tag{2.39}$$

where U_{Γ}^{m} is called the migration magnetic potential.

The migration magnetic field H_{Γ}^{m} is introduced as a result of the application of the adjoint operator, $A^{H\star}$, to the complex intensity of the observed magnetic field:

$$H_{\Gamma}^{m}(\ ) = A^{H\star}H_{\Gamma}, \tag{2.40}$$

The migration magnetic tensor field H_{T}^{m} is introduced as a result of the application of the adjoint operator, $A^{T\star}$ to the complex intensity of the observed magnetic tensor field as follows:

$$H_{T}^{m}(\ ) = A^{T\star}H_{T.} \tag{2.41}$$

2.5 Migration image of intensity of magnetization

It is very well known that the adjoint operator plays an important role in rapid imaging, and in the solution of inverse problem (Zhdanov, 2002). However, direct application of the adjoint operators to observed magnetic vector and/or tensor fields does not produce an adequate image of the subsurface magnetization distribution. It was shown by Zhdanov (2002) that, in order to image the sources of the magnetic field at their correct locations, one should apply an appropriate spatial weighting operator to the migration field. This weighting operator is constructed based on the integrated sensitivity of the magnetic data to the magnetization.

For example, the weighting operator W for magnetic inverse problem is a linear operator of multiplication by a function w that is equal to the square root of the integrated sensitivity of the complex intensity of the magnetic field, S:

$$w = \sqrt{S}. \tag{2.42}$$

The integrated sensitivity of the magnetic vector field is calculated by equation (AI.6) in Appendix I. Substituting this equation into expression (2.42), we have:

$$w_H = H_0 \sqrt{\sqrt{\frac{2\pi}{|z|^3}}}, \ \mathrm{z} < 0. \tag{2.43}$$

The integrated sensitivity of the magnetic tensor field is calculated by equation (AII.6) in Appendix B, By substituting this equation into expression (2.42), we have:

$$w_T = H_0 \sqrt{\sqrt{\frac{2\pi}{|z|^5}}}, \ \mathrm{z} < 0. \tag{2.44}$$

Similarly, for magnetic potential problem, the spatial weighting is computed as a simple form as:

$$w_U = H_0 \sqrt{\sqrt{\frac{2\pi}{|z|}}},\ \mathrm{z} < 0. \tag{2.45}$$

For the complex magnetic potential inverse problem, using the conjugate gradient type method, one can find the first approximation of the intensity of magnetization in the space of weighted model parameters as follows by assume zero initial model:

$$I_1^w = -k_U l_1^w, \tag{2.46}$$

where the direction of the steepest ascent in the space of weighted model parameters is given as follows:

$$l_1^w = -A_w^{u*} U_\Gamma. \tag{2.47}.$$

and the weighted forward operator and the intensity of magnetization, A_w^u, I^w, are related to the original operator and intensity of magnetization, A^u, I, by the following formulas:

$$A_w^u = A^u W^{-1}, I^w(\ ) = WI(\ ). \tag{2.48}$$

The length of step of the first iteration can be computed as follows:

$$k_U = \frac{\|A_w^{u*} U_\Gamma\|_M^2}{\|A_w^u A_w^{u*} U_\Gamma\|_D^2}. \tag{2.49}$$

By considering the above formulas, the fist iteration of the magnetic potential inverse problem with zero initial model in the space of weighted model parameters can be expressed as follows:

$$I_1^w = k_U A_w^{u*} U_\Gamma = k_U w_U^{-1} A^{u*} U_\Gamma. \tag{2.50}$$

Note that we need to recalculate the intensity of magnetization from the weighted intensity of magnetization as follows:

$$I_1(\ ) = w_U^{-1} I_1^w(\ ) = k_U w_U^{-2} A^{u*} U_\Gamma = k_U w_U^{-2} U_\Gamma^m(\ ). \tag{3.51}$$

Expression (3.51) is called a migration intensity of magnetization:

$$I_m^U = w_U^{-1} I_1^w(\ ) = k_U w_U^{-2} A^{u*} U_\Gamma = k_U w_U^{-2} U_\Gamma^m(\ ). \tag{2.52}$$

From the last formula, we find that the migration intensity of magnetization in magnetic potential problem is proportional to the migration magnetic potential and it is also proportional to the application of adjoint to the complex magnetic potential by taking spatial weightings. As we have discussed before, the application of adjoint operator to the complex magnetic potential is equivalent to the downward analytical continuation of the adjoint magnetic potential with the source located in the upper half plane. In such cases, the analytical continuation is done away from the source. As a result, this kind of analytical continuation is a stable transformation from the observed magnetic potential to the distribution of intensity of magnetization.

By substituting equation (2.28) into equation (2.52), we can find an explicit form to compute the migration intensity of magnetization as follows:

$$I_m^U = 2k_U w_U^{-2} \int_{-\infty}^{\infty} \frac{U(x')}{x - {}^*} dx'. \tag{2.53}$$

As we known, the migration intensity of magnetization is a complex function, therefore it could be written as:

$$I_m^U = I_{mr}^U + i I_{mi}^U. \tag{2.54}$$

By substituting equation (2.7) into equation (2.53), we find that

$$I_{mr}^U = 2k_U w_U^{-2} \int_{-\infty}^{\infty} \frac{z U_i(x',0) + (x'-x) U_r(x',0)}{(x-\mathrm{x})^2 + z^2} dx', \tag{2.55}$$

and

$$I_{mi}^U = 2k_U w_U^{-2} \int_{-\infty}^{\infty} \frac{(x'-x) U_i(x',0) - z U_r(x',0)}{(x-\mathrm{x})^2 + z^2} dx'. \tag{2.56}$$

The norm of the migration intensity of magnetization is calculated as follows:

$$|I_m^U| = \sqrt{(I_{mr}^U)^2 + \left(I_{mi}^U\right)^2}. \tag{2.57}$$

By repeating the above steps for complex magnetic field and complex magnetic tensor fiend, we can find that for complex magnetic field, the real part and imaginary of migration intensity of magnetization can be calculated as the following formulas:

$$I_{mr}^H = 2k_H w_H^{-2} \int_{-\infty}^{\infty} \frac{\left[(x-x')^2 - z^2\right] H_x(x',0) + 2(x-x')zH_z(x',0)}{[(x-x)^2+z^2]^2} dx', \tag{2.58}$$

and

$$I_{mi}^H = 2k_H w_H^{-2} \int_{-\infty}^{\infty} \frac{2(x-x')zH_x(x',0) - [(x-x')^2 - z^2]H_z(x',0)}{[(x-x')^2+z^2]^2} dx'. \tag{2.59}$$

For complex magnetic tensor field, we have:

$$I_{mr}^T = -4k_T w_T^{-2} \int_{-\infty}^{\infty} \frac{[(x-x')^3 - 3(x-x')z^2]H_{zz}(x',0) - [3(x-x')^2 z - z^3]H_{zx}(x',0)}{[(x-x')^2+z^2]^3} dx', \tag{2.60}$$

$$I_{mi}^T = -4k_T w_T^{-2} \int_{-\infty}^{\infty} \frac{\left[(x-x')^3 - 3(x-x')z^2\right]H_{zx}(x',0) + [3(x-x')^2 z - z^3]H_{zz}(x',0)}{[(x-x')^2+z^2]^3} dx'. \tag{2.61}$$

Formula (2.55) to (2.61) will be used to compute the distribution of migration intensity of magnetization for magnetic potential field, magnetic vector field and magnetic tensor field. For each case, we can compute the real part and imaginary part of the migration intensity of magnetization. Based on the real part and the imaginary part, one can also compute the norm of the migration intensity of magnetization. This will make it possible for us to find the distribution of anomalous magnetic masses in the case that the anomalous field is caused by both the inducing magnetic field and remanent magnetization. We can also estimate the distribution of anomalous magnetic body without information of the direction of inducing magnetic field in the case of inducing

magnetization only. In the following section, we will present case studies to demonstrate how this method works to locate the anomalous magnetic body.

2.6 Model studies

2.6.1 Model studies for complex magnetic potential migration

2.6.1.1 Model 1

In this model, we consider that there is one anomalous magnetic body located in the subsurface. The size of the anomalous magnetic body is 200 meters by 200 meters and it is buried 250 meters below the surface. We assume the inducing magnetic field is horizontal. In such case, the imaginary part of the complex intensity of magnetization would be equal to zero. In order to demonstrate that migration is a stable integral transformation, we added 30% random noise to the synthetic magnetic potential data. The upper panel of Figure 2.3 shows the synthetic magnetic potential data contaminated by random noise. The lower panel of Figure 2.3 shows the location of the anomalous magnetic body.

Figure 2.4 shows the migration intensity of magnetization. The upper panel shows the real part of migration intensity of magnetization and the lower shows the imaginary part. In each panel, the white outline indicates the location of the true model. From the upper panel we can see that the body is recovered even with 30% random noise added to the data. However, for the lower panel, we cannot find the location of the true model from the migration image. This is a reasonable result for the reason that in the true model we have assumed horizontal magnetization and the imaginary part of the intensity of

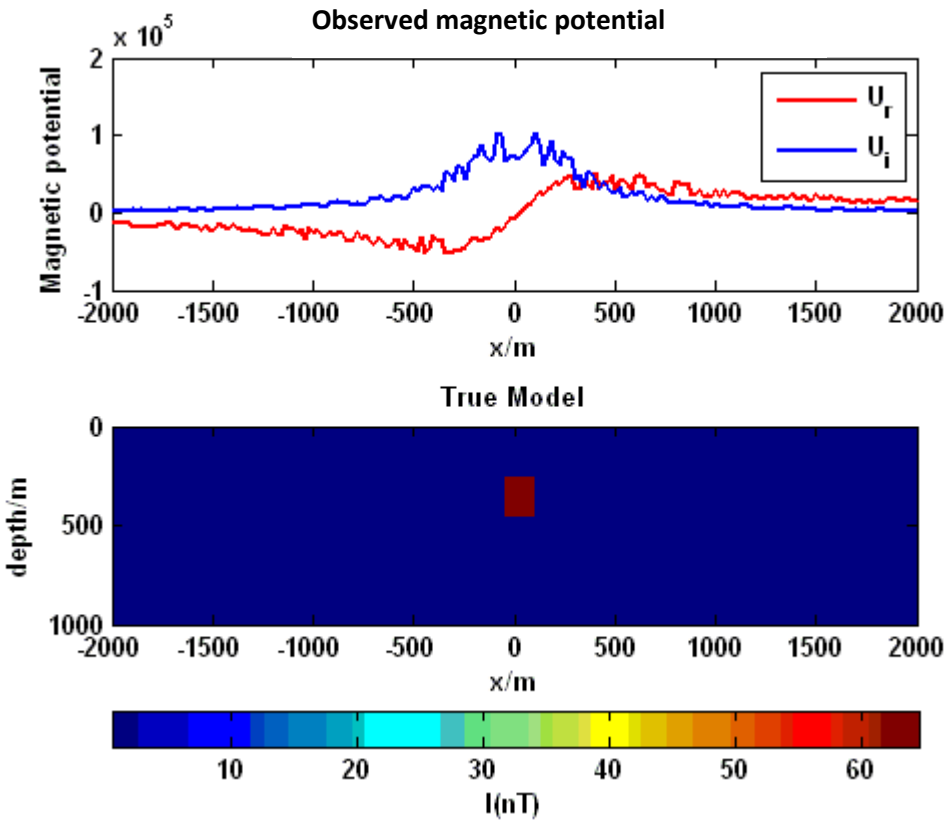

Figure 2.3. The upper panel of this figure shows the real part U_r and imaginary U_i part of magnetic potential data corresponding to model 1 and the lower panel of this figure shows the location of the anomalous body with red color.

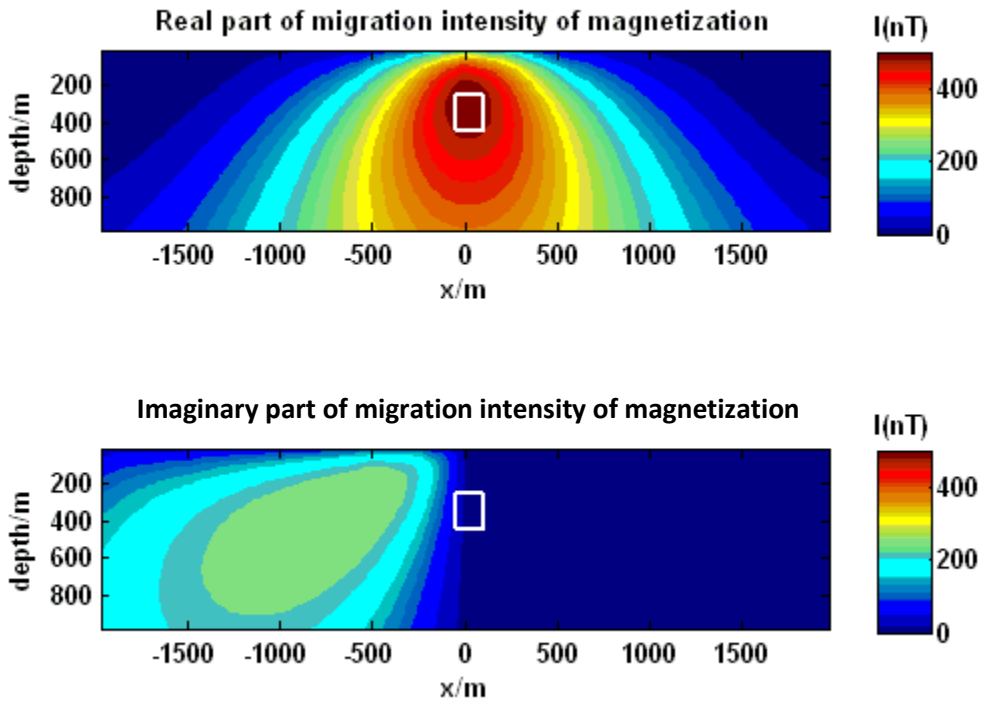

Figure 2.4. The upper panel of this figure shows the real part of the migration intensity of magnetization and the lower panel of this figure shows the imaginary part of the migration intensity of magnetization.

magnetization is zero.

Beside the real part and the imaginary part of the migration intensity of magnetization, we also present the image of the total intensity of magnetization which is calculated as taking the square root of the sum of the square of the real part of migration intensity of magnetization and the square of the imaginary of the migration intensity of magnetization. The image is shown as Figure 2.5. The white outline in Figure 2.5 also indicates the location of the true model. We can see that the model is also recovered from the total migration intensity of magnetization even without any information about what induced the anomalous magnetic potential.

2.6.1.2 Model 2

In this model, we consider that there is one anomalous magnetic body located in the subsurface. For this model, the location and size of the anomalous magnetic body is exactly the same as the previous model. In this model, we assume the inducing magnetic field is vertical. In such case, the real part of the complex intensity of magnetization would be equal to zero. We also added 30% random noise to the synthetic magnetic potential data. The upper panel of figure Figure 2.6 shows the synthetic magnetic potential data contaminated by 30% random noise. The lower panel of Figure 2.6 shows the location of the anomalous magnetic body.

Figure 2.7 shows the migration intensity of magnetization. The upper panel shows the real part of migration intensity of magnetization and the lower shows the imaginary part. In each panel, the white outline indicates the location of the true model. From the lower panel we can see that the body is recovered even with 30% random noise added to

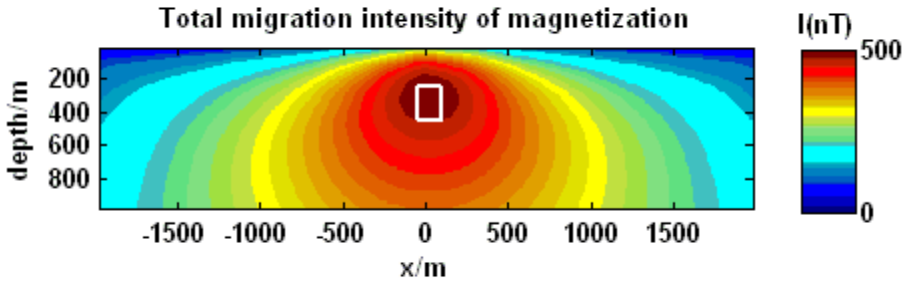

Figure 2.5. This figure shows the total migration intensity of magnetization, for model 1, which is calculated as the norm of the complex intensity of magnetization.

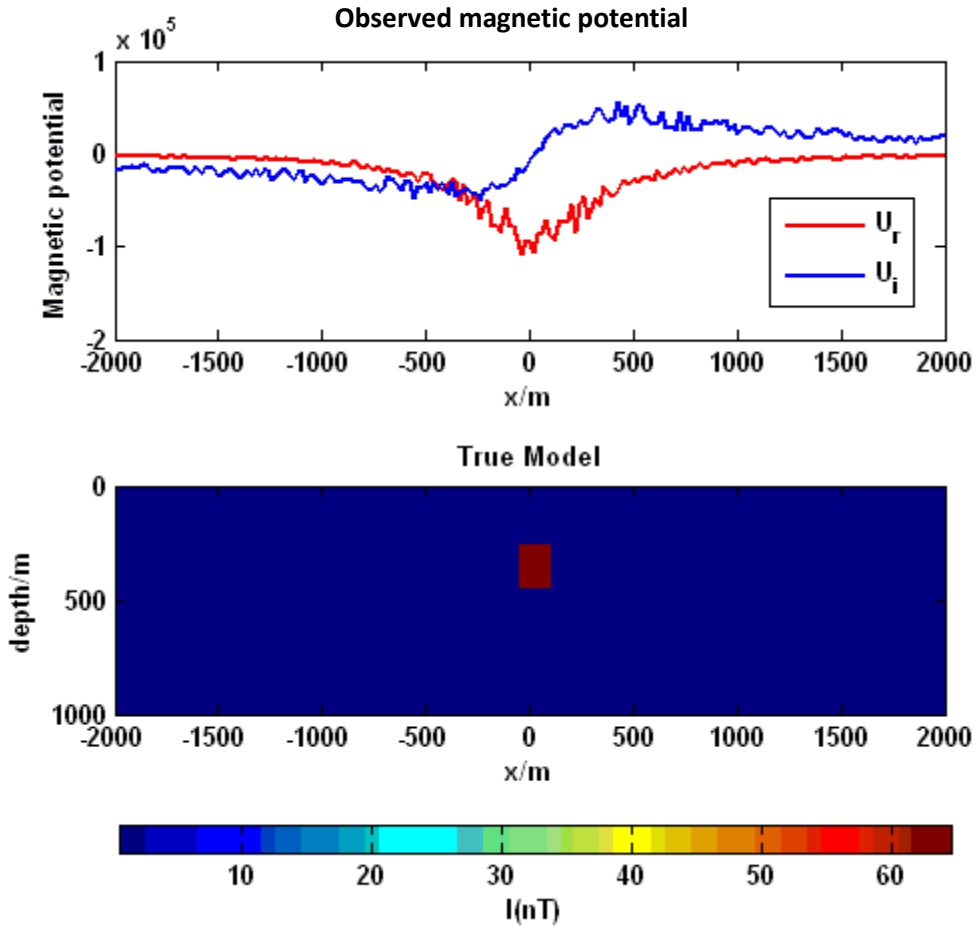

Figure 2.6. The upper panel of this figure shows the real part U_r and imaginary U_i part of magnetic potential data corresponding to model 2 and the lower panel of this figure shows the location of the anomalous body with red color.

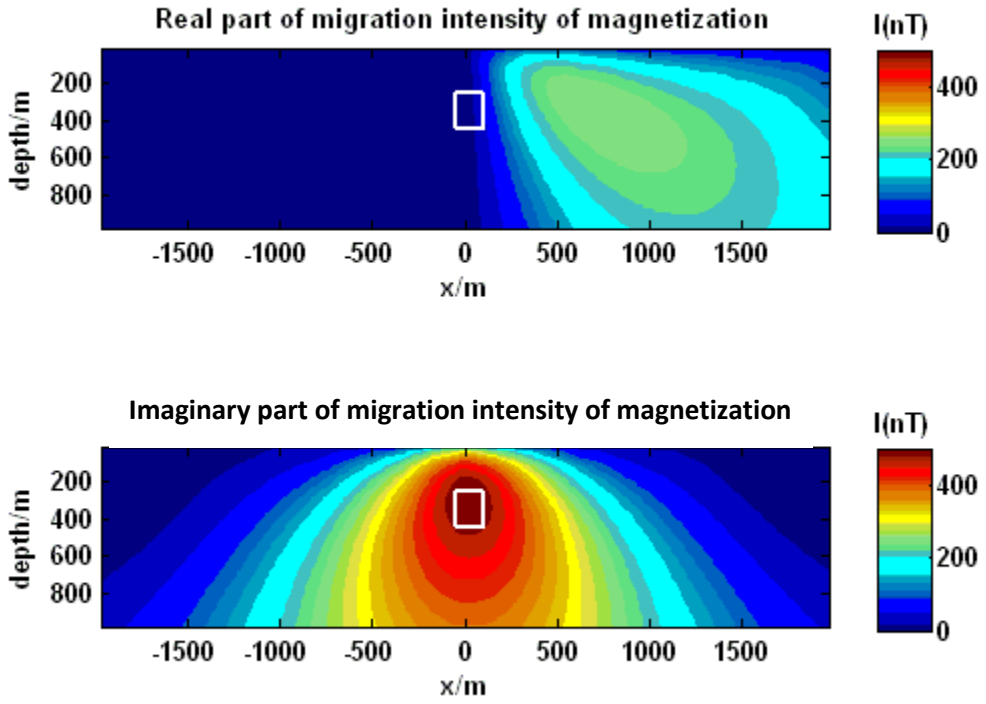

Figure 2.7. The upper panel of this figure shows the real part of the migration intensity of magnetization and the lower panel of this figure shows the imaginary part of the migration intensity of magnetization.

the data. However, for the upper panel, we cannot find the location of the true model from the migration image. This is a reasonable result for the reason that in the true model we have assumed vertical magnetization and the real part of the intensity of magnetization is zero.

The total migration intensity of magnetization is shown in Figure 2.8. The white outline in Figure 2.8 also indicates the location of the true model. We can see that the model is also recovered from the total migration intensity of magnetization even without any information about what induced the anomalous magnetic potential.

2.6.2 Model studies for complex magnetic field migration

2.6.2.1 Model 1

In this model, we consider that there is one anomalous magnetic body located in the subsurface. The size of the anomalous magnetic body is 200 meters by 200 meters and it is buried 250 meters below the surface. We assume the inducing magnetic field is horizontal. In such a case, the imaginary part of the complex intensity of magnetization would be equal to zero. In order to demonstrate that migration is a stable integral transformation, we added 30% random noise to the synthetic magnetic data. The upper panel of Figure 2.9 shows the synthetic magnetic data contaminated by 30% random noise. The lower panel of Figure 2.9 shows the location of the anomalous magnetic body.

Figure 2.10 shows the migration intensity of magnetization. The upper panel shows the real part of migration intensity of magnetization and the lower shows the imaginary part. In each panel, the white outline indicates the location of the true model.

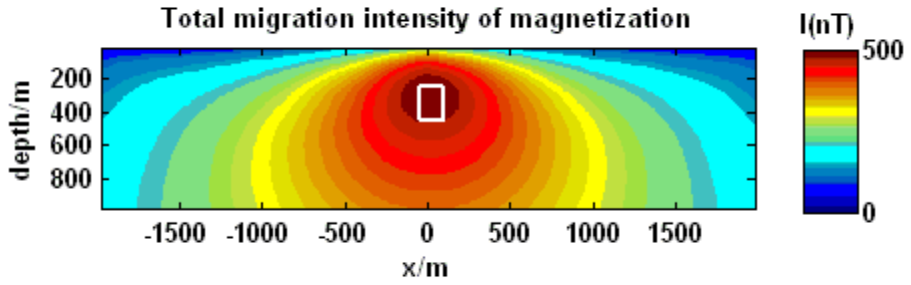

Figure 2.8. This figure shows the total migration intensity of magnetization, for model 2, which is calculated as the norm of the complex intensity of magnetization.

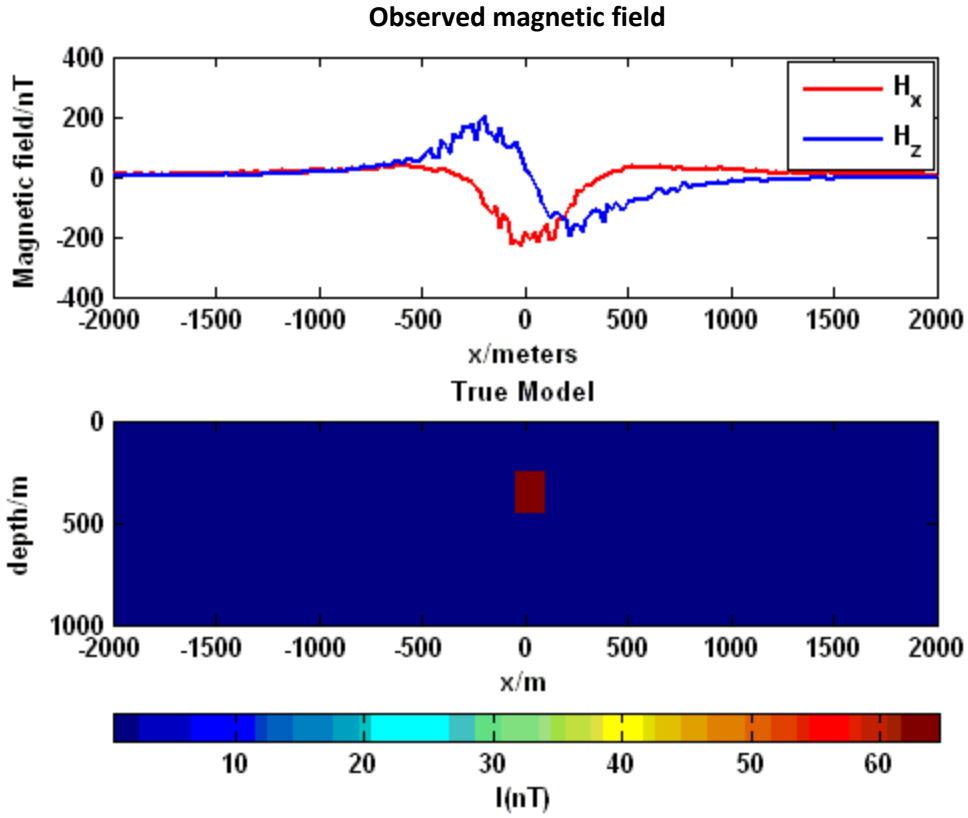

Figure 2.9. The upper panel of this figure shows the real part H_x and imaginary H_z part of magnetic field data corresponding to model 1 and the lower panel of this figure shows the location of the anomalous body with red color.

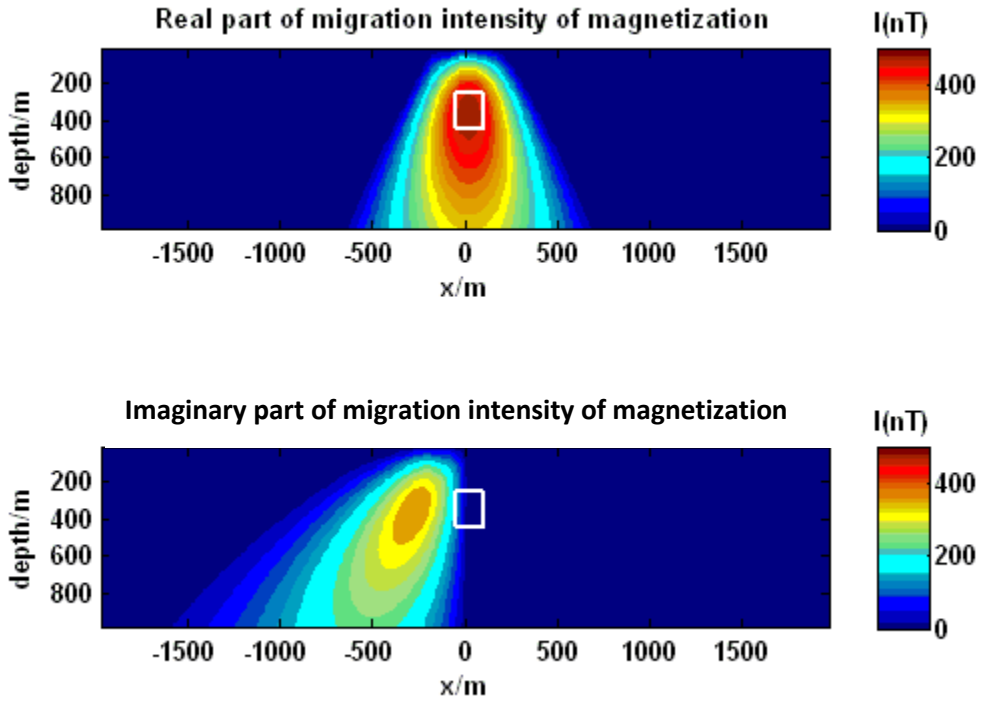

Figure 2.10. The upper panel of this figure shows the real part of the migration intensity of magnetization and the lower panel of this figure shows the imaginary part of the migration intensity of magnetization.

From the upper panel we can see that the body is recovered even with 30% random noise added to the data. However, for the lower panel, we cannot find the location of the true model from the migration image. This is a reasonable result for the reason that in the true model we have assumed horizontal magnetization and the imaginary part of the intensity of magnetization is zero.

Beside the real part and the imaginary part of the migration intensity of magnetization, we also present the image of the total intensity of magnetization which is calculated as taking the square root of the sum of the square of the real part of migration intensity of magnetization and the square of the imaginary of the migration intensity of magnetization. The image is shown as Figure 2.11. The white outline in Figure 2.11 also indicates the location of the true model. We can see that the model is also recovered from the total migration intensity of magnetization even without any information about what induced the anomalous magnetic field.

2.6.2.2 Model 2

In this model, we consider that there is one anomalous magnetic body located in the subsurface. For this model, the location and size of the anomalous magnetic body is exactly the same as the previous model. In this model, we assume the inducing magnetic field is vertical. In such case, the real part of the complex intensity of magnetization would be equal to zero. We also added 30% random noise to the synthetic magnetic field data. The upper panel of Figure 2.12 shows the synthetic magnetic field data contaminated by 30% random noise. The low panel of Figure 2.12 shows the location of the anomalous magnetic body.

Figure 2.13 shows the migration intensity of magnetization. The upper pane

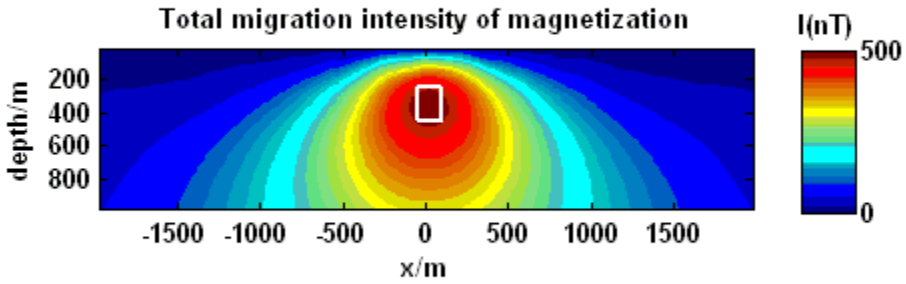

Figure 2.11. This figure shows the total migration intensity of magnetization which is calculated as the norm of the complex intensity of magnetization.

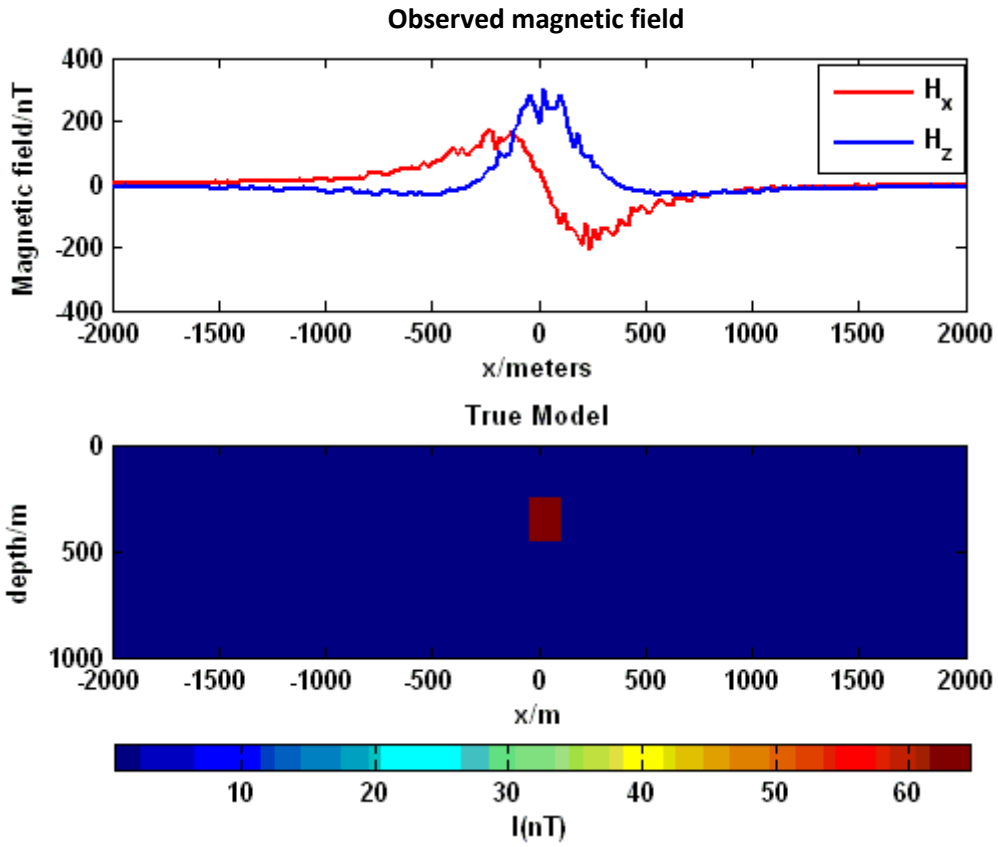

Figure 2.12. The upper panel of this figure shows the real part H_x and imaginary H_z part of magnetic field data corresponding to model 1 and the lower panel of this figure shows the location of the anomalous body with red color.

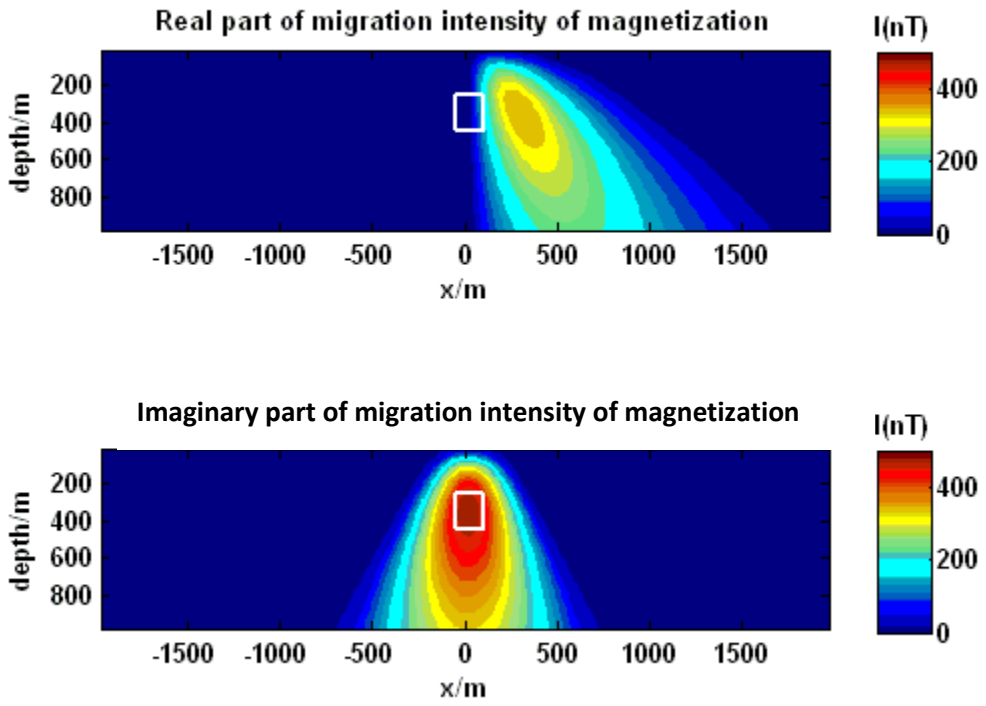

Figure 2.13. The upper panel of this figure shows the real part of the migration intensity of magnetization and the lower panel of this figure shows the imaginary part of the migration intensity of magnetization.

shows the real part of migration intensity of magnetization and the lower shows the imaginary part. In each panel, the white outline indicates the location of the true model. From the lower panel we can see that the body is recovered even with 30% random noise added to the data. However, for the upper panel, we cannot find the location of the true model from the migration image. This is a reasonable result for the reason that in the true model we have assumed vertical magnetization and the real part of the intensity of magnetization is zero.

The total migration intensity of magnetization is shown in Figure 2.14. The white outline in Figure 2.14 also indicates the location of the true model. We can see that the model is also recovered from the total migration intensity of magnetization even without any information about what induced the anomalous magnetic field.

2.6.3 Model studies for complex magnetic tensor field migration

2.6.3.1 Model 1

In this model, we consider that there is one anomalous magnetic body located in the subsurface. The size of the anomalous magnetic body is 200 meters by 200 meters and it is buried 250 meters below the surface. We assume the inducing magnetic field is horizontal. In such a case, the imaginary part of the complex intensity of magnetization would be equal to zero. In order to demonstrate that migration is a stable integral transformation, we added 30% random noise to the synthetic magnetic tensor field data. The upper panel of Figure 2.15 shows the synthetic magnetic tensor field data contaminated by 30% random noise. The lower panel of Figure 2.15 shows the location

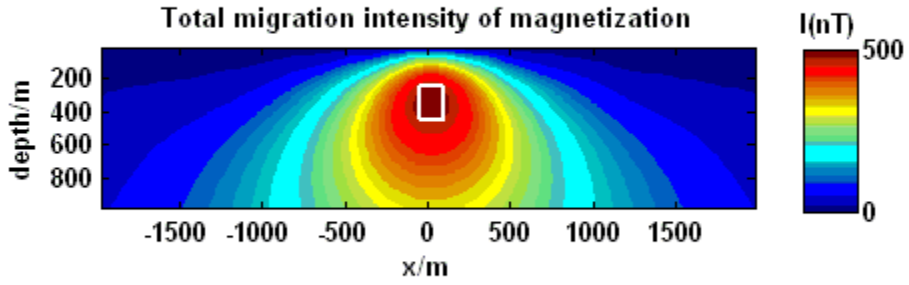

Figure 2.14. This figure shows the total migration intensity of magnetization which is calculated as the norm of the complex intensity of magnetization.

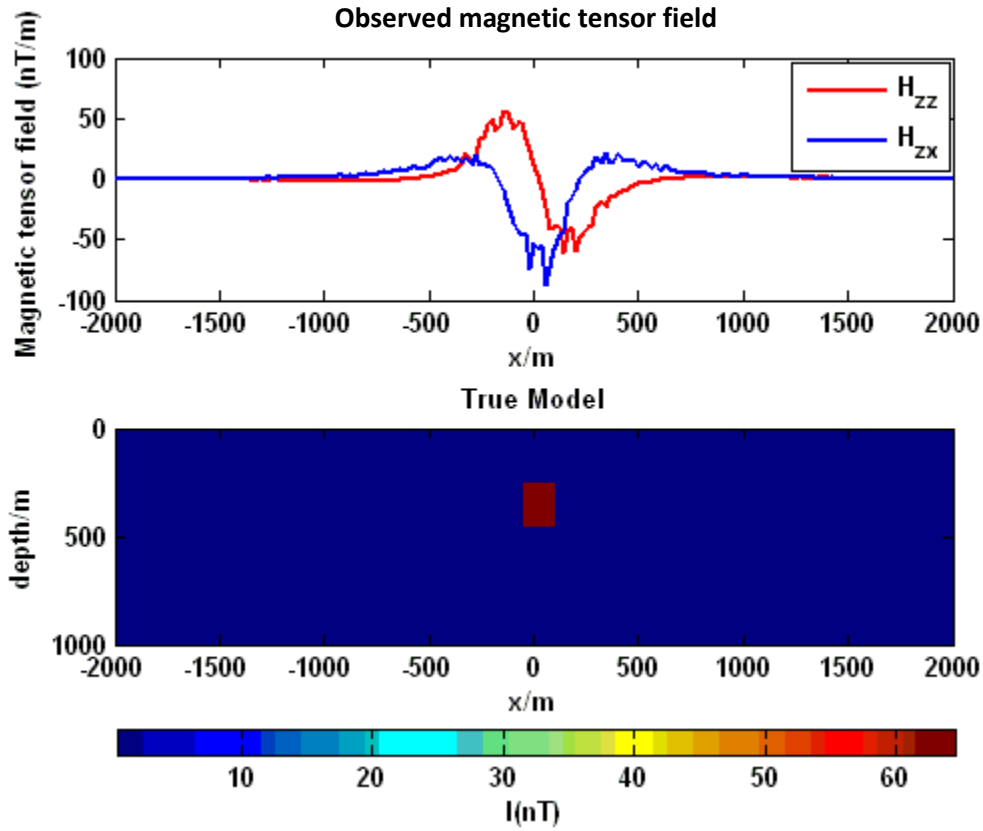

Figure 2.15. The upper panel of this figure shows the real part H_{zz} and imaginary H_{zx} part of magnetic tensor field data corresponding to model 1 and the lower panel of this figure shows the location of the anomalous body with red color.

of the anomalous magnetic body.

Figure 2.16 shows the migration intensity of magnetization. The upper panel shows the real part of migration intensity of magnetization and the lower shows the imaginary part. In each panel, the white outline indicates the location of the true model. From the upper panel we can see that the body is recovered even with 30% random noise added to the data. However, for the lower panel, we cannot find the location of the true model from the migration image. This is a reasonable result for the reason that in the true model we have assumed horizontal magnetization and the imaginary part of the intensity of magnetization is zero.

Beside the real part and the imaginary part of the migration intensity of magnetization, we also present the image of the total intensity of magnetization which is calculated as taking the square root of the sum of the square of the real part of migration intensity of magnetization and the square of the imaginary of the migration intensity of magnetization. The image is shown as Figure 2.17. The white outline in Figure 2.17 also indicates the location of the true model. We can see that the model is also recovered from the total migration intensity of magnetization even without any information about what induced the anomalous magnetic tensor field.

2.6.3.2 Model 2

In this model, we consider that there is one anomalous magnetic body located in the subsurface. For this model, the location and size of the anomalous magnetic body is exactly the same as in the previous model. In this model, we assume the inducing magnetic field is vertical. In such a case, the real part of the complex intensity of magnetization would be equal to zero. We also added 30% random noise to the synthetic

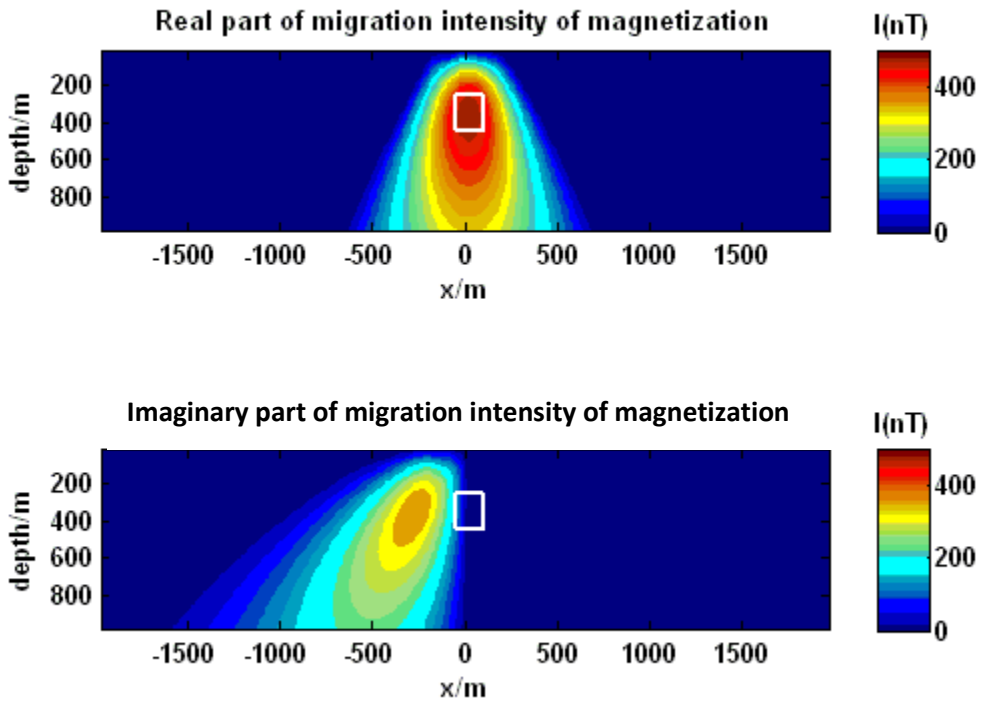

Figure 2.16. The upper panel of this figure shows the real part of the migration intensity of magnetization and the lower panel of this figure shows the imaginary part of the migration intensity of magnetization.

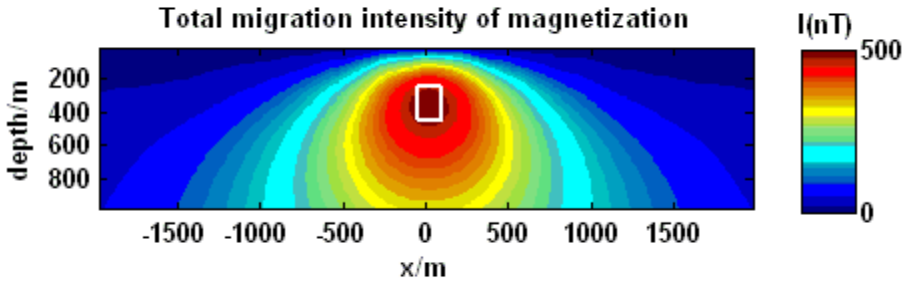

Figure 2.17. This figure shows the total migration intensity of magnetization which is calculated as the norm of the complex intensity of magnetization.

magnetic tensor field data. The upper panel of Figure 2.18 shows the synthetic magnetic tensor field data contaminated by 30% random noise. The lower panel of Figure 2.18 shows the location of the anomalous magnetic body.

Figure 2.19 shows the migration intensity of magnetization. The upper panel shows the real part of migration intensity of magnetization and the lower panel shows the imaginary part. In each panel, the white outline indicates the location of the true model. From the lower panel we can see that the body is recovered even with 30% random noise added to the data. However, for the upper panel, we cannot find the location of the true model from the migration image. This is a reasonable result for the reason that in the true model we have assumed vertical magnetization and the real part of the intensity of magnetization is zero.

The total migration intensity of magnetization is shown in Figure 2.20. The white outline in Figure 2.20 also indicates the location of the true model. We can see that the model is also recovered from the total migration intensity of magnetization even without any information about what induced the anomalous magnetic tensor field.

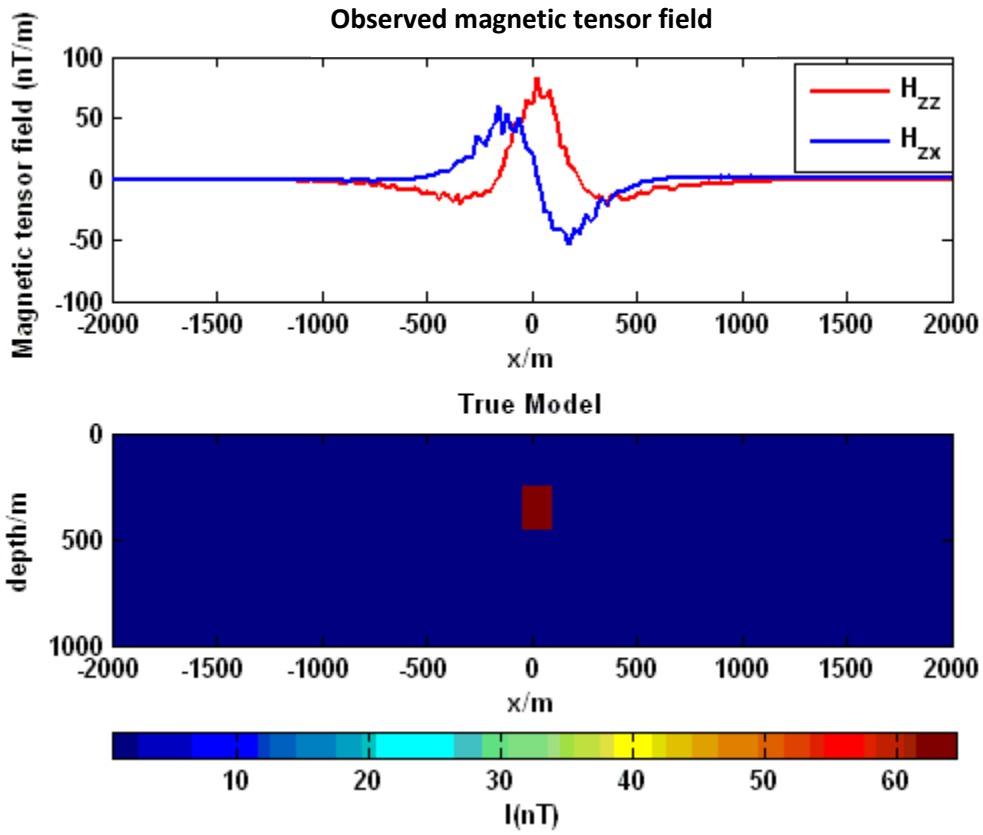

Figure 2.18. The upper panel of this figure shows the real part H_{zz} and imaginary H_{zx} part of magnetic tensor field data corresponding to model 1 and the lower panel of this figure shows the location of the anomalous body with red color.

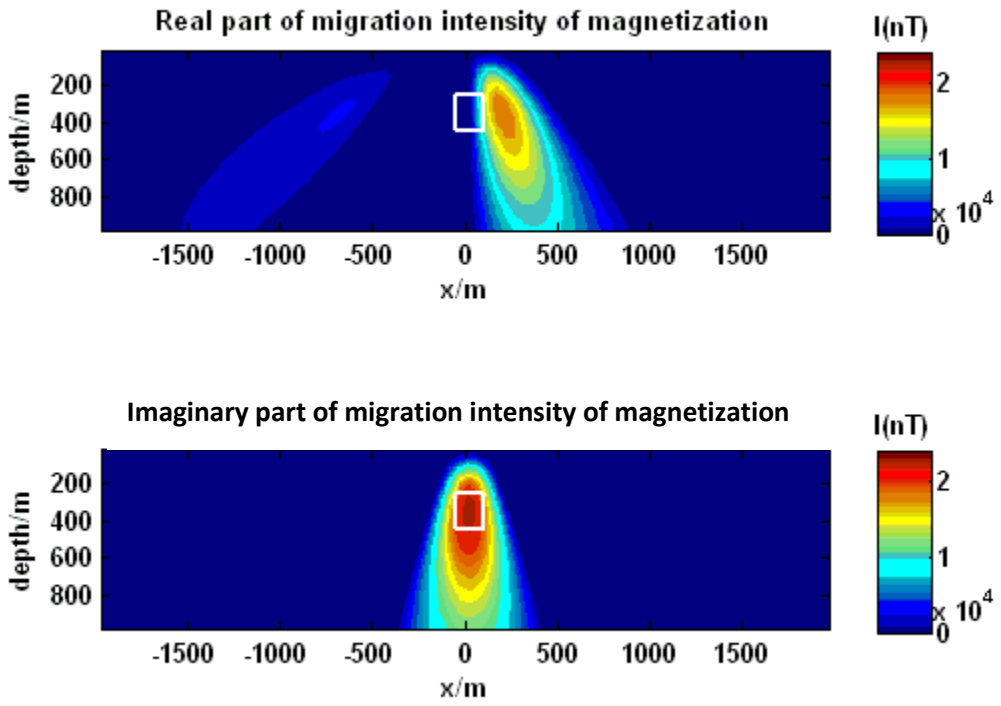

Figure 2.19. The upper panel of this figure shows the real part of the migration intensity of magnetization and the lower panel of this figure shows the imaginary part of the migration intensity of magnetization.

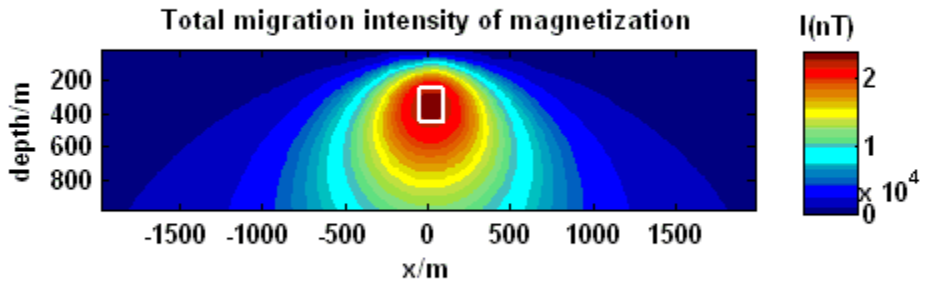

Figure 2.20. This figure shows the total migration intensity of magnetization which is calculated as the norm of the complex intensity of magnetization.

CHAPTER 3

MIGRATION OF MAGNETIC SUSCEPTIBILITY

In the previously chapter, we did the migration of complex intensity of magnetization. In such a case, we assume that we do not know the angle of magnetization which means the ratio between the real part of the complex intensity of magnetization and the imaginary part of the complex intensity of magnetization is unknown. After migration, one can get the image of the complex intensity of magnetization with the real part and imaginary part. The migration of magnetization intensity is equivalent to solving the inverse problem with regard to two different unknown model parameters. However, in most cases, the effect of remanent magnetization can be ignored. As a result, the complex intensity of magnetization with both the real part and imaginary part can be related to the inducing magnetic field by magnetic susceptibility. Under these circumstances, we only need to solve the inverse problem for magnetic susceptibility. In subsection one of Chapter 3 we will present the theory of forward modeling for complex magnetic field and complex magnetic tensor field. In subsection two, we will show the explicit form of adjoint operator for complex magnetic field and complex magnetic tensor field. Similar to the previous chapter, in subsection three we will introduce adjoint field for complex magnetic field and complex magnetic tensor field. In subsection four, we

will introduce migration image of magnetic susceptibility. Model studies for migration of complex magnetic field and complex magnetic tensor field with respect to magnetic susceptibility is presented in subsection five.

3.1 Forward problem for the models described by magnetic susceptibility

As shown in formula (2.2), the complex magnetic field can be expressed as follows:

$$H(\ ) = -H_x(x,z) + iH_z(x,,z) = A^H(I) = -2\iint \frac{1}{(\ -\ )^2} I(\ )\, ds, \tag{3.1}$$

where $I(\ )$ is the complex intensity of magnetization which is expressed as $I(\ ) = I_x(x,z) + iI_z(x,z)$.

In the previous chapter, we have assumed that we did not have any information about the direction of magnetization, which means that the relationship between I_x and I_z is uncertain. In this section we will introduce the intensity of inducing magnetic field as H_0 and the magnetic susceptibility as χ. In 2-D case, we also introduce the unit vector of magnetization, which denotes the direction of magnetization as follows:

$$l = (l_x, l_z). \tag{3.2}$$

The complex intensity of magnetization can be related to magnetic susceptibility and inducing magnetic field as follows:

$$I_x(x,z) = H_0\chi(x,z)l_x, \tag{3.3}$$

and

$$I_z(x,z) = H_0\chi(x,z)l_z. \tag{3.4}$$

By substituting formula (3.3) and (3.4) into formula (3.1), we can find that:

$$H(\ ) = -2\iint \frac{l_x + il_z}{(x - x' + iz)^2} H_0 \chi \, ds, \tag{3.5}$$

where we assume that we observe the magnetic field on the flat surface and, as a result, the z coordinate of the observation point can be set to zero for simplicity.

By separating the real and the imaginary parts of the complex magnetic field, we can find the expression for H_x and H_z as:

$$H_x(x', z') = -2\iint_\Gamma \frac{l_x[(x-x')^2 - z^2] + 2l_z(x-x')z}{[(x-x')^2 + z^2]^2} H_0 \chi ds, \tag{3.6}$$

$$H_z(x', z') = -2\iint_\Gamma \frac{l_z\left[(x-x')^2 - z^2\right] - 2l_x(x-x')z}{[(x-x')^2 + z^2]^2} H_0 \chi \, ds. \tag{3.7}$$

We will use equations (3.6) and (3.7) for modeling synthetic magnetic field data with anomalous magnetic susceptibility.

Similarly, by repeating the above process for complex magnetic tensor field, we can find that:

$$H_T(\ ') = -2\iint_\Gamma \frac{1}{(\ - \ ')^3} I(\ ) \, ds = -2\iint_\Gamma \frac{l_x + il_z}{(x - x' + iz)^2} H_0 \chi \, ds. \tag{3.8}$$

By separating the real and imaginary parts in the last equation, we find explicit expression for H_{zz} and H_{zx} as:

$$H_{zz}(x', z') = -4\iint_\Gamma \frac{l_x[(x-x')^3 - 3(x-x')(z-z')^2] + l_z[3(x-x')^2(z-z') - (z-z')^3]}{[(x-x')^2 + (z-z')^2]^3} H_0 \chi \, ds, \tag{3.9}$$

and

$$H_{zx}(x', z') = -4\iint_\Gamma \frac{l_z\left[(x-x')^3 - 3(x-x')(z-z')^2\right] - l_x[3(x-x')^2(z-z') - (z-z')^3]}{[(x-x')^2 + (z-z')^2]^3} H_0 \chi ds. \tag{3.10}$$

Equation (3.9) and (3.10) will be used for modeling synthetic magnetic tensor data.

Note that both the magnetic vector field $H(\ )$ and the magnetic tensor field data $H_T(\ ')$ are described by analytical functions outside the masses, i.e., $\notin \Gamma$ (Zhdanov,

1988). It will be shown in subsequent sections of this chapter that the analytical representations derived above for anomalous magnetic and magnetic tensor fields provide a useful tool for the solution of inversion and migration problems.

3.2 Adjoint operators for complex magnetic vector and tensor fields

As we have explained before, adjoint operators play a pivotal role in migration theory. In the previous chapter, we summarized the derivation for the adjoint operator for complex magnetic potential, complex magnetic field and complex magnetic tensor field with respect to model parameter of intensity of magnetization.

Consider a complex magnetic field, for example. Let's assume that we have the observed magnetic field, $H(\zeta')$ along a line of observation L. The domain, Γ, which is filled with the masses generating the observed field, is located in the lower half-plane.

We introduce a complex Hilbert space D of data (magnetic field, magnetic tensor field and/or magnetic potential) with the metric:

$$(f,U)_D = \int_L f(\ )\,U^*(\ )d\ ;\ f,g\ \in D, \tag{3.11}$$

and a real Hilbert space M of models (function $\chi(\ )$ with the metric:

$$(\eta,\chi)_M = \iint_\Gamma \eta(\ )\chi(\ )ds;\ \eta,\chi \in M. \tag{3.12}$$

Let us find an explicit form of the adjoint operator $A^{H\star}$ for the magnetic field problem:

$$(A^H(\chi),f)_D = (\chi,A^{H\star}(f))_M. \tag{3.13}$$

Using the definitions (3.11) and (3.12) of the inner products and expression (3.5) for the forward operator, we can rewrite formula (3.13) as:

$$(A^H(\chi), f)_D = \int_L A^H(\chi) f^* dx = \int_- \left[-2 \iint \frac{l_x + il_z}{(-x')^2} \mathrm{H}_0 \chi \, ds\right] f^*(x') dx' =$$

$$-\left(\chi, 2 \int_{-\infty}^{\infty} \frac{l_x + il_z}{(-x')^2} \mathrm{H}_0 f^*(x') dx'\right)_M = \left(\chi, A^{H\star}(f)\right)_M, \tag{3.14}$$

where, as usual, the asterisk, *, denotes the complex conjugate. From equation (3.14), we can find the following identity:

$$\left(\chi, A^{H\star}(f) + 2 \int_{-\infty}^{\infty} \frac{l_x + il_z}{(-x')^2} H_0 f^*(x') dx'\right)_M = 0. \tag{3.15}$$

Since equation (3.15) holds for any ( ), e.g.,

$$\chi = A^{H\star}(f) + 2 \int_{-\infty}^{\infty} \frac{l_x + il_z}{(-x')^2} H_0 f^*(x') dx', \tag{3.16}$$

then by substituting equation (3.16) into equation (3.15), we obtain:

$$\| A^{H\star}(f) + 2 \int_{-\infty}^{\infty} \frac{l_x + il_z}{(-x')^2} H_0 f^*(x') dx' \|^2 = 0. \tag{3.17}$$

From the last equation, we find that the adjoint magnetic operator, $A^{H\star}$ applied to any function $f(x')$ is given by:

$$A^{H\star}(f) = -2 \int_{-\infty}^{\infty} \frac{(l_x + il_z)\mathrm{H}_0 f^*(x')}{(-x')^2} dx'. \tag{3.18}$$

From a derivation similar to the one above, we can find that the adjoint magnetic tensor operator, $A^{T\star}$, applied to any function $f(x')$ is given by the following expression:

$$A^{T\star}(f) = -4 \int_{-\infty}^{\infty} \frac{(l_x + il_z)\mathrm{H}_0 f^*(x')}{(-x')^3} dx'. \tag{3.19}$$

3.3 Adjoint fields and their relationship with magnetic field and magnetic tensor field

Similar to the case we described in the previous chapter, we assume that there is an imaginary source located in the upper half-space which is a mirror image of the original source located in the lower half-space with respect to the real axis of the complex plane (Figure 2.1). We will call the magnetic field and magnetic tensor field generated by the imaginary source an adjoint magnetic field and an adjoint magnetic tensor field, respectively.

Consider the magnetic field for example. Using Cauchy integral formula, after some algebra, one can find the following expression for the analytical continuation of the adjoint magnetic field in the lower half-space as:

$$H_{\Gamma^\star}(\ ) = -\frac{1}{2\pi i}\int_{-\infty,}^{\infty} \frac{H_{\Gamma^\star}(x')}{x'-}\,dx'. \tag{3.20}$$

There exists the following identity for adjoint magnetic field:

$$H_{\Gamma}^{*}(x') = H_{\Gamma^\star}(x'). \tag{3.21}$$

As a result, equation (3.20) can be rewritten as follows:

$$H_{\Gamma^\star}(\ ) = -\frac{1}{2\pi i}\int_{-\infty,}^{\infty} \frac{H_{\Gamma}^{*}(x')}{x'-}\,dx'. \tag{3.22}$$

Taking into account equation (3.22), we can represent equation (3.18) in the following form:

$$A^{H\star}H_{\Gamma} = -2(l_x + il_z)\int_{-\infty}^{\infty} \frac{\mathrm{H}_0 H_{\Gamma}^{*}(x')}{(\ -x')^2}\,dx' = 2(l_x + il_z)H_0\frac{\partial}{\partial}\int_{-\infty}^{\infty} \frac{H_{\Gamma}^{*}(x')}{(\ -x')}\,dx' =$$

$$-4\pi i(l_x + il_z)\mathrm{H}_0\frac{\partial}{\partial}H_{\Gamma^\star}. \tag{3.23}$$

Thus, we see that the application of the adjoint operator to an observed magnetic field is equivalent to taking a derivative of the analytical continuation of the adjoint magnetic field in the lower half-plane. Following Zhdanov (2002), we will call this transformation a magnetic field migration, and use the notation:

$$H_{\Gamma}^{m}(\ ) = A^{H\star}H_{\Gamma}, \tag{3.24}$$

where H_{Γ}^{m} is called the migration magnetic field.

By repeating the above process for complex magnetic tensor field, we can introduce the migration magnetic tensor field as follows:

$$H_{T}^{m}(\ ) = A^{T\star}H_{T} = A^{T\star}(f) = -4\int_{-\infty}^{\infty}\frac{(l_x+il_z)\mathrm{H}_0 H_T^*(x')}{(\ -x')^3}dx' =$$

$$-(l_x+il_z)\mathrm{H}_0\frac{\partial^2}{\partial^{\ 2}}\int_{-\infty}^{\infty}\frac{H_T^*(x')}{(\ -x')}dx' = 2\pi i(l_x+il_z)H_0\frac{\partial^2}{\partial^{\ 2}}H_{T^\star}. \tag{3.25}$$

Thus, we can see that the migration of the observed magnetic tensor field H_{Γ} is equivalent to taking the second derivative of the analytical continuation of the adjoint magnetic tensor field $H_{T^\star}$ in the lower half-plane. This property indicates that the tensor field migration has a higher sensitivity to the magnetization than the magnetic field migration.

3.4 Migration image of magnetic susceptibility

Direct application of the adjoint operators to observed magnetic vector and/or tensor fields does not produce an adequate image of the subsurface magnetization distribution. It was shown by Zhdanov (2002) that, in order to image the sources of the magnetic field at their correct locations, one should apply an appropriate spatial

weighting operator to the migration field. This weighting operator is constructed based on the integrated sensitivity of the magnetic data to the magnetization. One can refer to section 2.5 for the integrated sensitivity for magnetic field and magnetic tensor field problem. The detailed derivation of integrated sensitivity for magnetic field and magnetic tensor field is given in Appendix I and Appendix II.

In a general case, the iteration process of the reweighted conjugate gradient method for magnetic inverse problem is described in the following formulas:

$$\chi_{n+1}^{w} = \chi_{n}^{w} + \delta\chi^{w} = \chi_{n+1}^{w} - k_n \tilde{l}_{w}^{\alpha}, \tag{3.26}$$

$$\tilde{l}_{w}^{\alpha}(\chi_{n}^{w}) = \tilde{l}_{wn}^{\alpha} = l_{wn}^{\alpha} + \beta_{n}^{\alpha}\tilde{l}_{w(n-1)}^{\alpha},\ \tilde{l}_{w0}^{\alpha} = l_{w0}^{\alpha}, \tag{3.27}$$

$$\beta_{n}^{\alpha} = \| l_{wn}^{\alpha} \|_{M}^{2} / \| l_{w(n-1)}^{\alpha} \|_{M,}^{2} \tag{3.28}$$

$$k_n = \frac{(\tilde{l}_{wn}^{\alpha}, l_{wn}^{\alpha})_M}{\|A_w^H \tilde{l}_{wn}^{\alpha}\|_D^2 + \alpha\|\tilde{l}_{wn}^{\alpha}\|_M^2}. \tag{3.29}$$

where the regularized direction of the steepest ascent is given by the expression:

$$l_{w}^{\alpha}(\chi_{n}^{w}) = ReA_{w}^{H\star}(A_{w}^{H}(\chi_{n}^{w}) - H_{\Gamma}) + \alpha_n \chi_{n}^{w}. \tag{3.30}$$

The weighted operator, A_w^H, and migration susceptibility, χ_n^w, are related to the original operator A^H, and susceptibility χ_n by the following equations:

$$A_{w}^{H} = A^{H}W^{-1}, \chi_{n}^{w}(\ ) = w_H(z)\chi_n(\ ). \tag{3.31}$$

Note that in every iteration, we have to recalculate the susceptibility from the weighted susceptibility:

$$\chi_n(\ ) = w_H^{-1}(z)\chi_{n}^{w}(\ ). \tag{3.32}$$

According to equations (3.26) and (3.32), the first iteration of the magnetic inverse problem at the initial model with zero magnetic susceptibility can be expressed as follows:

$$\chi_1(\ ) = w_H^{-1}(z)\chi_1^w(\ ) = k_0 w_H^{-1}(z)\ ReA_w^{H\star}(H_\Gamma) = k_0 w_H^{-2}(z) ReA^{H\star}(H_\Gamma), \tag{3.33}$$

where:

$$k_0 = k_H = \frac{\|A_w^{H\star} U_\Gamma\|_M^2}{\|A_w^H A_w^{H\star} H_\Gamma\|_D^2}. \tag{3.34}$$

Equation (3.33) is called migration susceptibility, χ_m^H:

$$\chi_m^H = k_0 w_H^{-2}(z) Re A^{H\star}(H_\Gamma) = k_0 w_H^{-2}(z) Re H_\Gamma^m. \tag{3.35}$$

It is proportional to the weighted real part of the migration magnetic vector field, H_Γ^m. Thus, migration transformation with spatial weighting provides a stable algorithm for calculating the migration susceptibility. Substituting equation (3.18) into (3.35), after some algebra, we finally find the following:

$$\chi_m^H = 2k_0 w_H^{-2}(z) \int_{-\infty}^{\infty} \frac{(l_x H_x - l_z H_z)[(x-x')^2 - z^2]}{[(x-x')^2 + z^2]^2} H_0 \, dx'$$

$$+4k_0 w_H^{-2}(z) \int_{-\infty}^{\infty} \frac{(l_z H_x + l_x H_z)(x-x')z}{[(x-x')^2+z^2]^2} H_0 \, dx'. \tag{3.26}$$

In a similar way, we can repeat the above process for complex magnetic tensor field. We can find the analytical expression of migration magnetic susceptibility for magnetic tensor field as:

$$\chi_m^T = -4k_0 w_T^{-2}(z) \int_{-\infty}^{\infty} \frac{(l_x H_{zz} + l_z H_{zx})[(x-x')^3 - 3(x-x')z^2]}{[(x-x')^2+z^2]^3} \mathrm{H}_0 \, dx' -$$

$$4k_0 w_T^{-2}(z) \int_{-\infty}^{\infty} \frac{(l_z H_{zz} - l_x H_{zx})[3(x-x')^2 z - z^3]}{[(x-x')^2+z^2]^3} H_0 \, dx'. \tag{3.37}$$

3.5 Model studies

3.5.1 Model studies for complex magnetic field migration

3.5.1.1 Model 1

In this model, we consider there is one anomalous magnetic body located in the subsurface. The size of the anomalous body is 100 meters by 300 meters. The body is buried 400 meters below the surface and extends from -50 meters to 50 meters in a horizontal direction. The angle of magnetization is 45 degree which means that the real part and the imaginary part of the complex intensity of magnetization are equal to each other. In order to demonstrate that magnetic field migration is a stable transformation from the observed magnetic field data to the magnetic susceptibility distribution, we added 30% random noise to the synthetic data.

The upper panel of Figure 3.1 shows the observed magnetic field data contaminated by 30% random nose. The lower panel of Figure 3.1 shows the distribution of migration magnetic susceptibility. The black outline in the lower panel indicates the location of the true model. From this figure we can find the location of the anomalous magnetic body is well recovered even if the data are contaminated by a high level of random noise.

3.5.1.2 Model 2

In this model, we consider there are two anomalous magnetic bodies both buried 300 meters below the surface. The two anomalous bodies have the same size of 200 meters by 200 meters. The first anomalous body extends from -1100 meters to -900

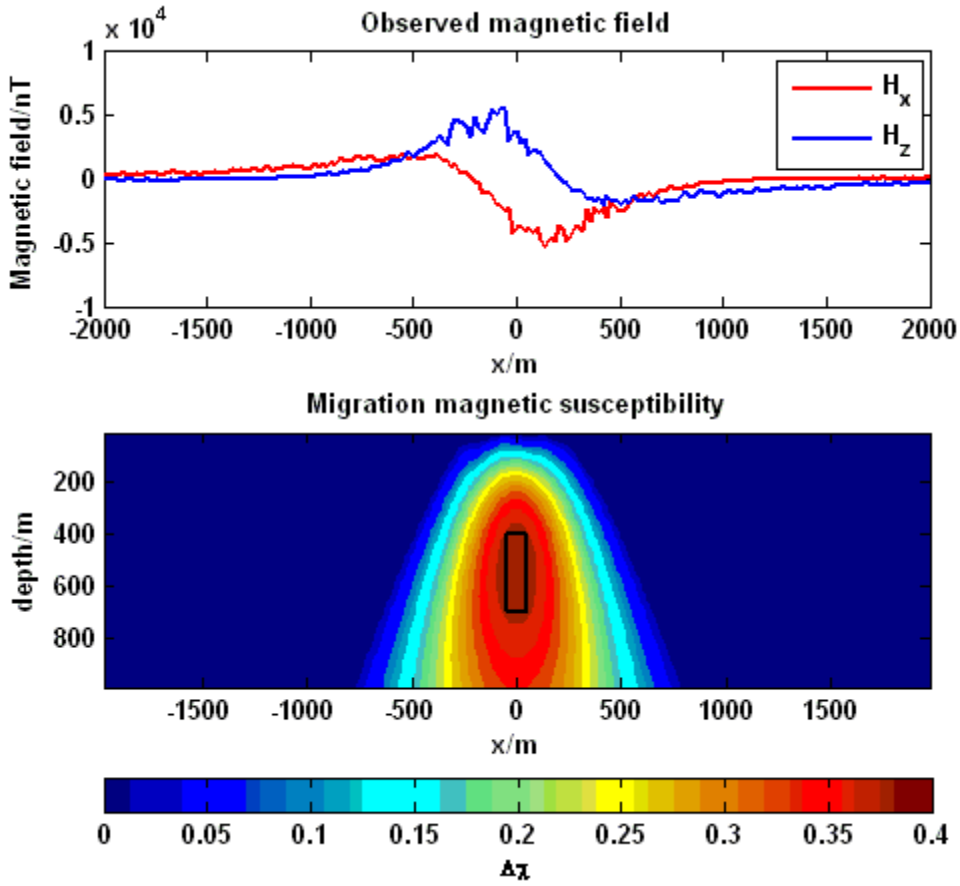

Figure 3.1. The upper panel of this figure shows the real part H_x and imaginary part H_z of magnetic tensor field data corresponding to model 1 and the lower panel of this figure shows the migration magnetic susceptibility distribution. The black outline indicates the true model.

meters horizontally and the second anomalous body extends from 900 meters to 1100 meters in a horizontal direction. The two anomalous bodies depart from each other with 800 meters. The angle of magnetization is 45 degrees which means that the real part and the imaginary part of the complex intensity of magnetization are equal to each other. We added 30% random noise to the synthetic data.

The upper panel of Figure 3.2 shows the observed magnetic field data contaminated by 30% random nose. The lower panel of Figure 3.2 shows the distribution of migration magnetic susceptibility. The black outline in the lower panel indicates the location of the true model. From this figure we see that both of these two anomalous magnetic bodies are well recovered by magnetic field migration. Even if the observed magnetic field data are contaminated by a high level of noise.

3.5.1.3 Model 3

In this model, we consider there are two anomalous magnetic bodies with the first body buried 300 meters below the surface and the second body buried 400 meters below the surface. The two anomalous bodies have the same size of 200 meters by 200 meters. The first anomalous body extends from -1100 meters to -900 meters in a horizontal direction and the second anomalous body extends from 900 meters to 1100 meters in a horizontal direction. The two anomalous bodies depart from each with 800 meters. The angle of magnetization is 45 degrees which means that the real part and the imaginary part of the complex intensity of magnetization are equal to each other. We added 30% random noise to the synthetic data.

The upper panel of Figure 3.3 shows the observed magnetic field data contaminated by 30% random nose. The lower panel of Figure 3.3 shows the distribution

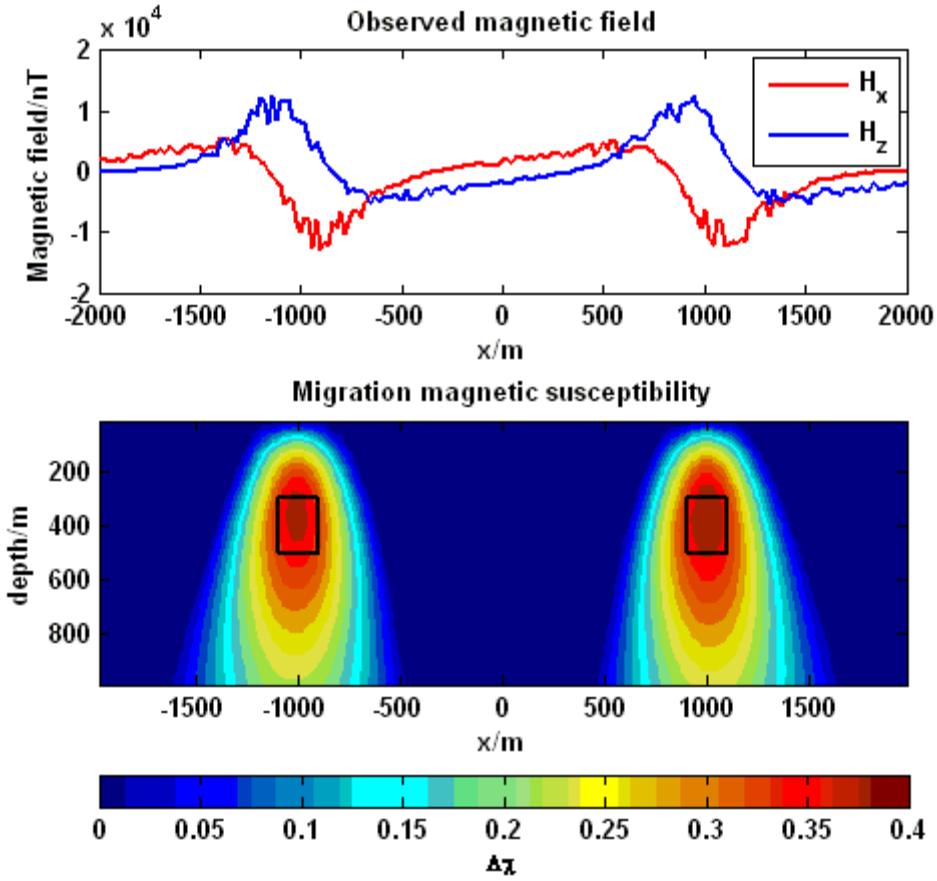

Figure 3.2. The upper panel of this figure shows the real part H_x and imaginary part H_z of magnetic tensor field data corresponding to model 2 and the lower panel of this figure shows the migration magnetic susceptibility distribution. The black outline indicates the true model.

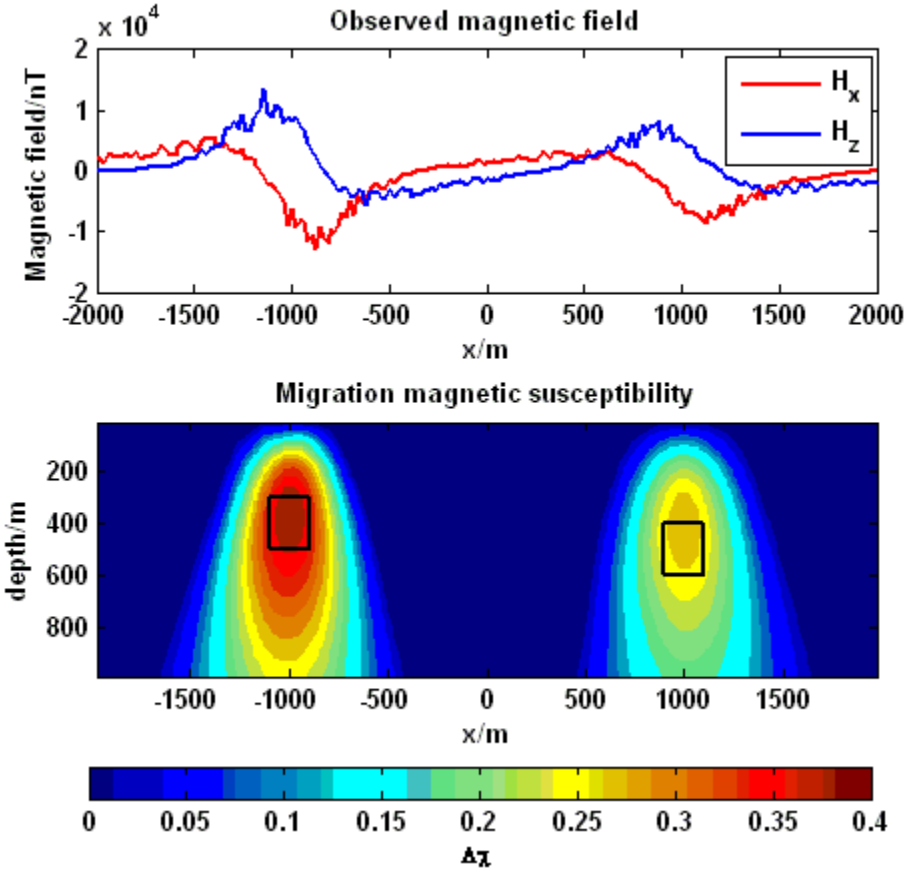

Figure 3.3. The upper panel of this figure shows the real part H_x and imaginary part H_z of magnetic tensor field data corresponding to model 3 and the lower panel of this figure shows the migration magnetic susceptibility distribution. The black outline indicates the true model.

of migration magnetic susceptibility. The black outline in the lower panel indicates the location of the true model. From this figure we see that when both of these two anomalous magnetic bodies are recovered by magnetic field migration, even the observed magnetic field data are contaminated by a high level of noise. For the second anomalous body which is buried 100 meters deeper than the first body, our migration image shows a little bit shallow anomalous compared to the true model.

3.5.2 Model studies for complex magnetic tensor field migration

3.5.2.1 Model 1

In this model, we consider there is one anomalous magnetic body located in the subsurface. The size of the anomalous body is 100 meters by 300 meters. The body is buried 400 meters below the surface and extends from -50 meters to 50 meters in a horizontal direction. The angle of magnetization is 45 degree which means that the real part and the imaginary part of the complex intensity of magnetization are equal to each other. In order to demonstrate that magnetic field migration is a stable transformation from the observed magnetic field data to the magnetic susceptibility distribution, we added 30% random noise to the synthetic data.

The upper panel of Figure 3.4 shows the observed magnetic tensor field data contaminated by 30% random nose. The lower panel of Figure 3.4 shows the distribution of migration magnetic susceptibility. The black outline in the lower panel indicates the location of the true model. From this figure we can find the location of the anomalous magnetic body is well recovered even if the data are contaminated by a high level of random noise and the image of migration magnetic susceptibility is pretty compact.

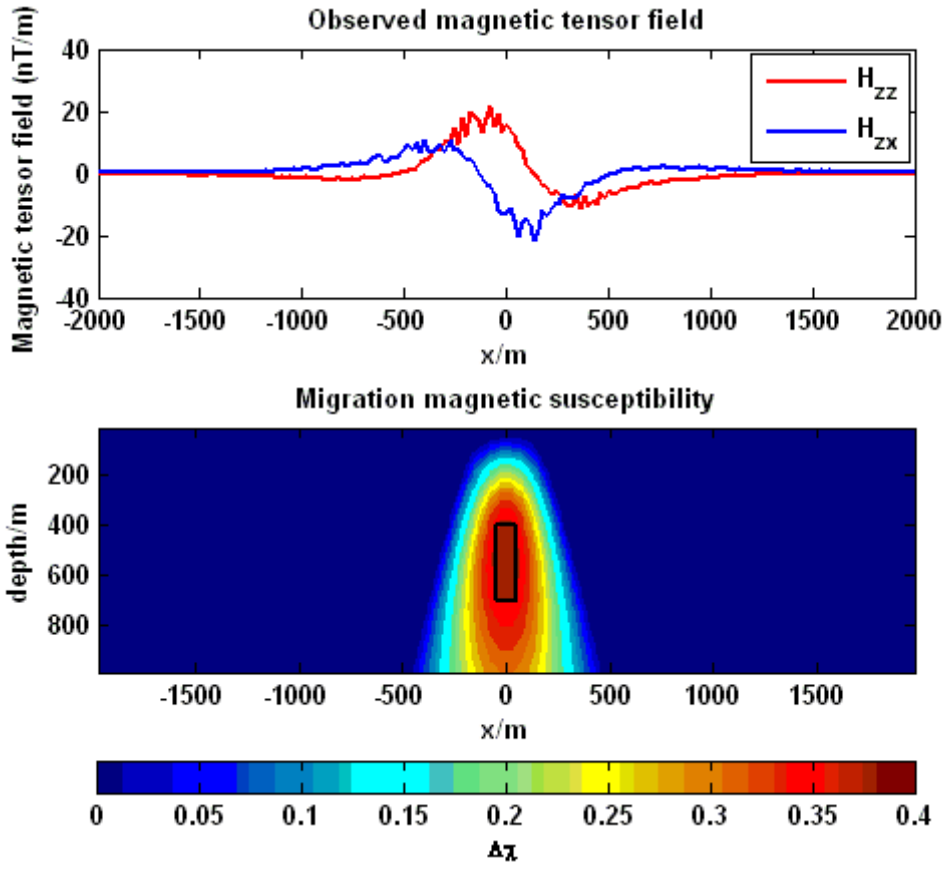

Figure 3.4. The upper panel of this figure shows the real part H_{zz} and imaginary part H_{zx} of magnetic tensor field data corresponding to model 1 and the lower panel of this figure shows the migration magnetic susceptibility distribution. The black outline indicates the true model.

3.5.2.2 Model 2

In this model, we consider there are two anomalous magnetic bodies both buried 300 meters below the surface. The two anomalous bodies have the same size of 200 meters by 200 meters. The first anomalous body extends from -1100 meters to -900 meters in a horizontal direction and the second anomalous body extends from 900 meters to 1100 meters in a horizontal direction. The two anomalous bodies depart from each with 800 meters. The angle of magnetization is 45 degrees which means that the real part and the imaginary part of the complex intensity of magnetization are equal to each other. We added 30% random noise to the synthetic data.

The upper panel of Figure 3.5 shows the observed magnetic tensor field data contaminated by 30% random nose. The lower panel of Figure 3.5 shows the distribution of migration magnetic susceptibility. The black outline in the lower panel indicates the location of the true model. From this figure we see that both of these two anomalous magnetic bodies are well recovered by magnetic field migration even if the observed magnetic field data are contaminated by a high level of noise and the image is very focused.

3.5.2.3 Model 3

In this model, we consider there are two anomalous magnetic bodies with the first body buried 300 meters below the surface and the second body buried 400 meters below the surface. The two anomalous bodies have the same size of 200 meters by 200 meters. The first anomalous body extends from -1100 meters to -900 meters in horizontal direction and the second anomalous body extends from 900 meters to 1100 meters in horizontal direction. The two anomalous bodies depart from each with 800 meters. The

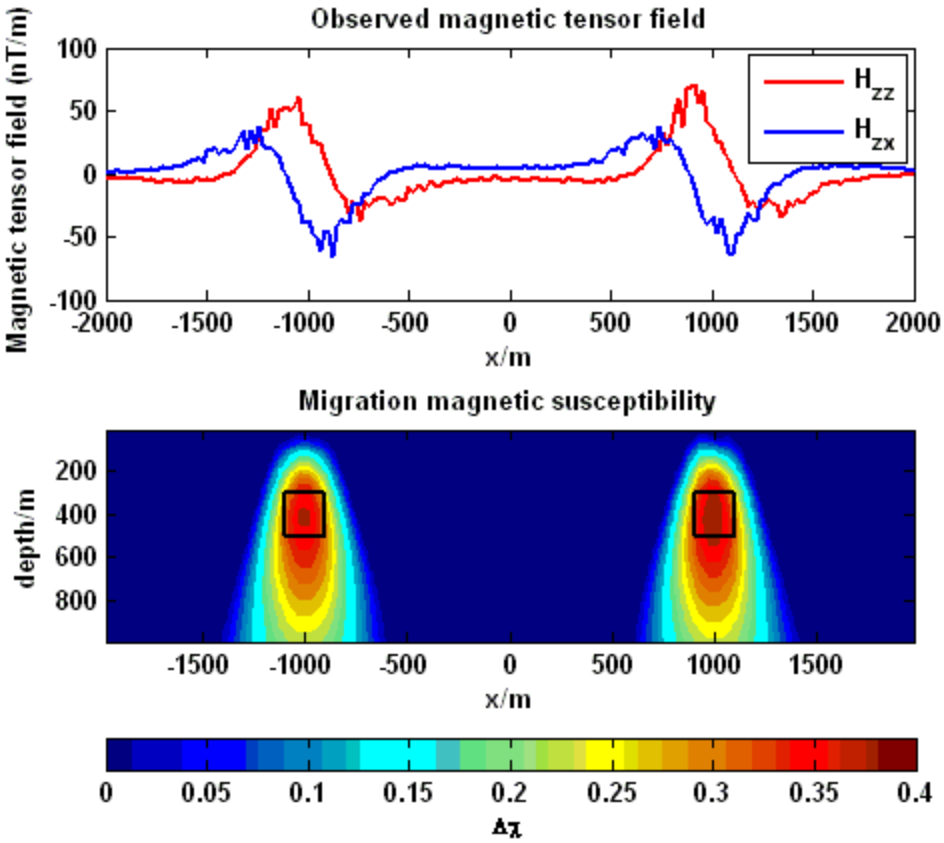

Figure 3.5. The upper panel of this figure shows the real part H_{zz} and imaginary part H_{zx} of magnetic tensor field data corresponding to model 2 and the lower panel of this figure shows the migration magnetic susceptibility distribution. The black outline indicates the true model.

angle of magnetization is 45 degrees which means that the real part and the imaginary part of the complex intensity of magnetization are equal to each other. We added 30% random noise to the synthetic data.

The upper panel of Figure 3.6 shows the observed magnetic tensor field data contaminated by 30% random nose. The lower panel of Figure 3.6 shows the distribution of migration magnetic susceptibility. The black outline in the lower panel indicates the location of the true model. From this figure we see that both of these two anomalous magnetic bodies are recovered by magnetic field migration even if the observed magnetic field data are contaminated by a high level of noise and the image we obtained for migration magnetic susceptibility is very compact.

3.5.3 Comparison between magnetic field and magnetic tensor field migration for synthetic models

In this section we will compare the migration results we get from magnetic field and magnetic tensor field for synthetic models. The left panel of Figure 3.7 shows the distribution of migration magnetic susceptibility we get from magnetic field migration and the right panel shows the distribution of migration magnetic susceptibility we get from magnetic field migration. The synthetic models we used for magnetic vector field migration are exactly the same as the models we used for magnetic tensor field migration. From the figure we can see that the anomalous magnetic body can be recovered by both magnetic field migration and magnetic tensor field migration. For the same models, the image of migration magnetic susceptibility we obtain from magnetic tensor field

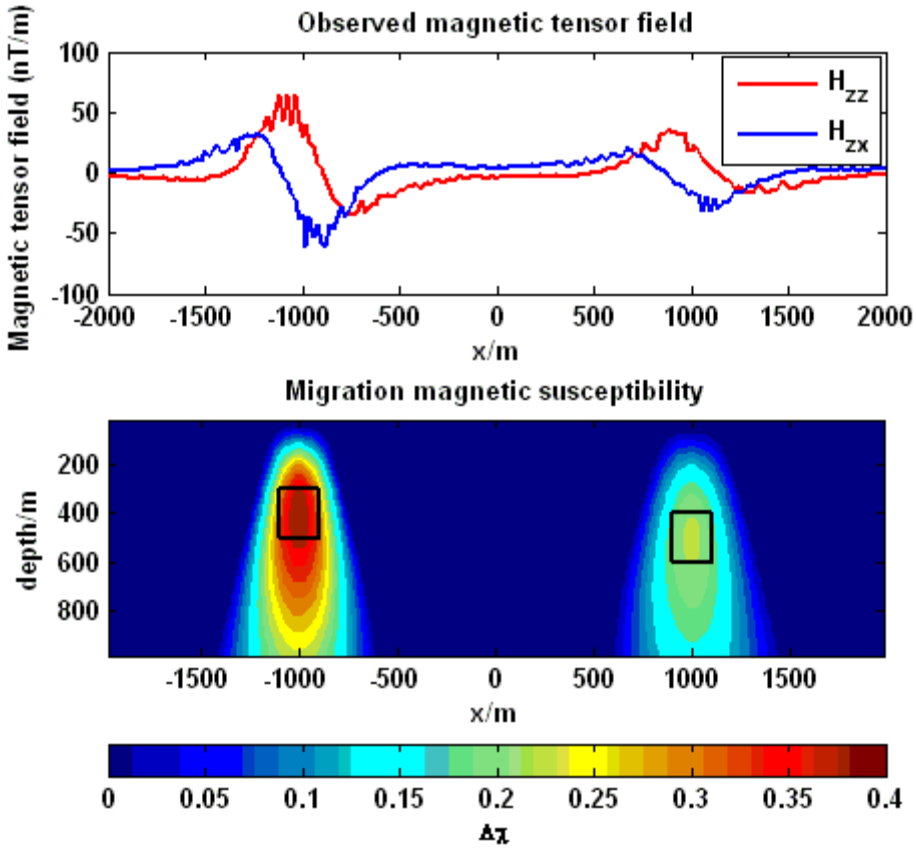

Figure 3.6. The upper panel of this figure shows the real part H_{zz} and imaginary part H_{zx} of magnetic tensor field data corresponding to model 3 and the lower panel of this figure shows the migration magnetic susceptibility distribution. The black outline indicates the true model.

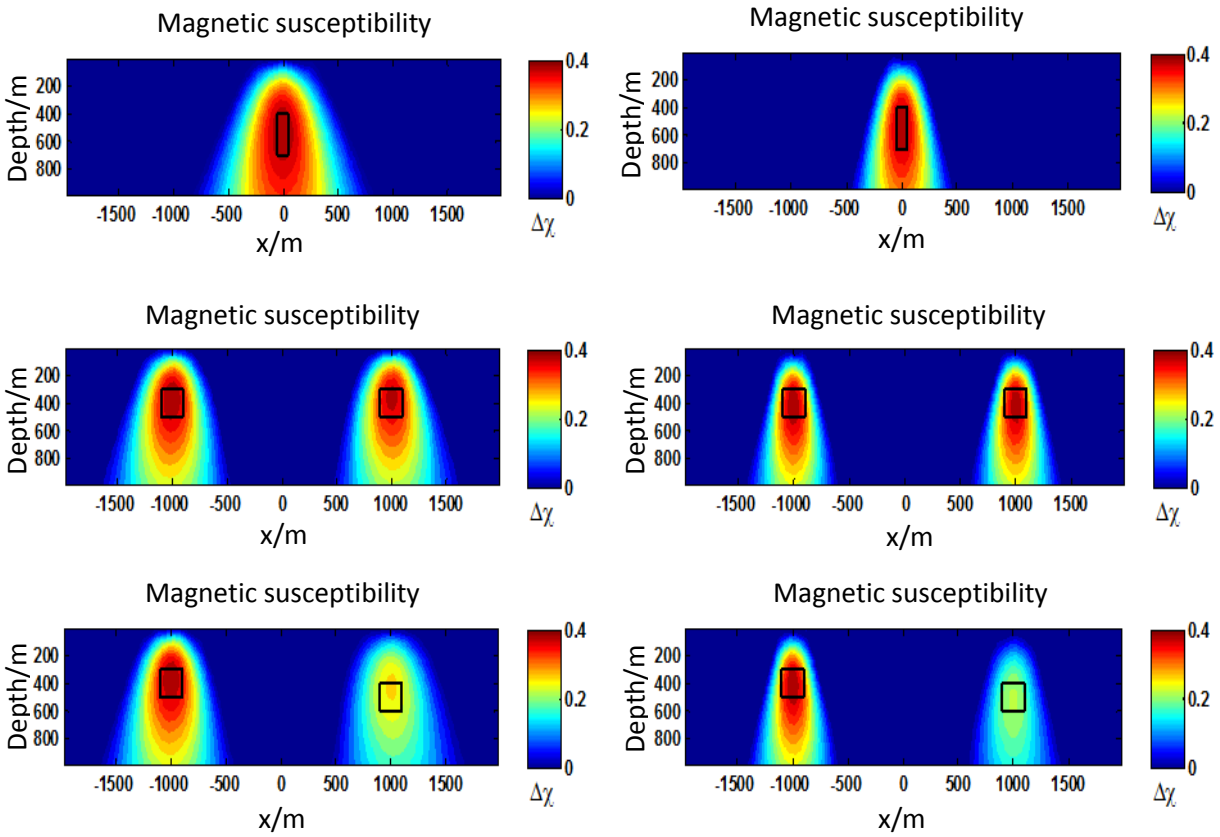

Figure 3.7. The left panel of this figure shows the migration magnetic susceptibility we get from magnetic field migration for three synthetic models and the right panel shows the migration magnetic susceptibility distribution we get from magnetic tensor field migration for the same three synthetic models.

migration is more focusing than that we get from magnetic vector field migration. Especially for the last model with two anomalous magnetic bodies at different depth, the migration image of the second body after applying magnetic vector field migration shows shallow anomaly compared to the true model. However, after applying magnetic tensor field migration, the location of the second anomalous body is well recovered. As a result, magnetic tensor field migration shows some advantage to get higher resolution image comparing to magnetic vector migration.

CHAPTER 4

3-D REGULARIZED INVERSION OF MAGNETIC DATA

In this chapter, we will introduce the basic theory for 3-D magnetic forward modeling and regularized inversion problems. In the first section, we will talk about the 3-D forward modeling for magnetic field and magnetic tensor field. In section two, we will introduce the inversion methodology, which is based on the minimization of Tikhonov parametric functional. The effects of topography on forward modeling and inversion of magnetic problem are discussed in section three. In section four, we will present some model studies.

4.1 3-D forward modeling for magnetic field and magnetic tensor field

Magnetic data are related to magnetic susceptibility by a linear operator. In discrete form, we can express this as follows:

$$\mathbf{d} = \mathbf{Am}, \tag{4.1}$$

where $\mathbf{d}$ is an N_d length vector of magnetic data, $\mathbf{A}$ is the $N_d \times N_m$ matrix of the linear operator, and $\mathbf{m}$ is an N_m length vector of model parameters, i.e., magnetic susceptibility.

As a linear problem, matrix **A** also serves as the sensitivity matrix for the corresponding inverse problem, and this will be discussed subsequently.

We adopt the common assumption that there is no remanent magnetization, that the self-demagnetization effect is negligible, and that the magnetic susceptibility is isotropic. Under such assumptions, the intensity of magnetization **I**(**r**) is linearly related to an inducing magnetic field, $H_0(\mathbf{r})$, through the magnetic susceptibility, $\chi(\mathbf{r})$:

$$\mathbf{I}(\mathbf{r}) = \chi(\mathbf{r})H_0. \tag{4.2}$$

We discretize the 3-D earth model into a grid N_m cells, each of constant magnetic susceptibility. Following Zhdanov (2002), the magnetic potential can be expressed in discrete form as:

$$U(\mathbf{r}') = \sum_{k=1}^{N_m} \chi_k \iiint_{D_k} \psi(\mathbf{r}', \mathbf{r})\, dv, \tag{4.3}$$

where $\psi(\mathbf{r}', \mathbf{r})$ is the whole space Green's function for the magnetic potential. As we will show, all magnetic fields can be computed as the spatial derivative of equation (4.3). For example, the magnetic field, **H**(**r**) is the first derivative of the magnetic potential

$$\mathbf{H}(\mathbf{r}) = \nabla U(\mathbf{r}), \tag{4.4}$$

and takes the following discrete form:

$$\mathbf{H}(\mathbf{r}') = -H_0 \sum_{k=1}^{N_m} \chi_k \iiint_{D_k} \frac{1}{|\mathbf{r}-\mathbf{r}'|^3} \left[\mathbf{l} - \frac{3(\mathbf{l}\cdot(\mathbf{r}-\mathbf{r}'))(\mathbf{r}-\mathbf{r}')}{|\mathbf{r}-\mathbf{r}'|^2}\right] dv, \tag{4.5}$$

where $\mathbf{r}' = (x', y', z')$ denotes the point of observation, $\mathbf{r} = (x, y, z)$ denotes the point of source, $\mathbf{l} = (l_x, l_y, l_z)$ is the direction of magnetization, and H_0 is the absolute value of the inducing magnetic field.

Closed-form solutions for the volume integral in equation (4.5) over right rectangular prisms of magnetic susceptibility have been previously presented (e.g., Bhattacharyya, 1980). We prefer to evaluate the volume integral numerically using

single-point Gaussian integration with pulse basis functions. In this case, $\mathbf{r} = (x, y, z)$ denotes the cell center. We assume constant discretization of Δx, Δy, Δz in the x, y, and z directions, respectively.

It follows that equation (4.5) can be simplified as follows:

$$\mathbf{H}(\mathbf{r}') = -H_0 \sum_{k=1}^{N_m} \chi_k \frac{1}{|\mathbf{r}-\mathbf{r}'|^3} [\mathbf{l} - \frac{3(\mathbf{l}\cdot(\mathbf{r}-\mathbf{r}'))(\mathbf{r}-\mathbf{r}')}{|\mathbf{r}-\mathbf{r}'|^2}] \Delta x \Delta y \Delta z. \tag{4.6}$$

For our coordinate system, we assume positive y is northing, positive x is easting, and positive z is downward. For any magnetic survey, the inclination (I), declination (D) and azimuth (A) of the inducing magnetic field (in degrees) can be predicted from the International Geomagnetic Reference Filed (IGRF) model. Assuming the inclination is positive below the horizontal, the declination is positive east of the true north, and the azimuth is positive east of the north, the directional cosines of the inducing magnetic field are as follows:

$$l_x = \cos(I)\cos(D - A), \tag{4.7}$$

$$l_y = \cos(I)\sin(D - A), \tag{4.8}$$

$$l_z = \sin(I). \tag{4.9}$$

From equation (4.6), we can derive discrete expressions for the vector components of the magnetic field:

$$H_x(\mathbf{r}') = -H_0 \sum_{k=1}^{N_m} \chi_k \frac{1}{|\mathbf{r}-\mathbf{r}'|^3} [l_x - \frac{3t(x_k - x')}{|\mathbf{r}-\mathbf{r}'|^2}] \Delta x \Delta y \Delta z, \tag{4.10}$$

$$H_y(\mathbf{r}') = -H_0 \sum_{k=1}^{N_m} \chi_k \frac{1}{|\mathbf{r}-\mathbf{r}'|^3} [l_y - \frac{3t(y_k - y')}{|\mathbf{r}-\mathbf{r}'|^2}] \Delta x \Delta y \Delta z, \tag{4.11}$$

$$H_z(\mathbf{r}') = -H_0 \sum_{k=1}^{N_m} \chi_k \frac{1}{|\mathbf{r}-\mathbf{r}'|^3} [l_z - \frac{3t(z_k - z')}{|\mathbf{r}-\mathbf{r}'|^2}] \Delta x \Delta y \Delta z, \tag{4.12}$$

where $t = l_x(x_k - x') + l_y(y_k - y') + l_z(z_k - z')$.

The second spatial derivatives of the magnetic potential,

$$H_{\alpha\beta} = \frac{\partial^2}{\partial\alpha\beta} U(\mathbf{r}),\ \alpha,\beta = x,y,z, \tag{4.13}$$

forms a symmetric magnetic tensor:

$$\widehat{\mathbf{H}} = \begin{bmatrix} H_{xx} & H_{xy} & H_{xz} \\ H_{yx} & H_{yy} & H_{yz} \\ H_{zx} & H_{zy} & H_{zz} \end{bmatrix},$$

with zero trace where:

$$H_{\alpha\beta} = \frac{\partial H_\alpha}{\partial\beta},\ \alpha,\beta = x,y,z, \tag{4.14}$$

and it is implied that the nine tensor components, only five are independent.

By introducing $t = l_x(x_k - x') + l_y(y_k - y') + l_z(z_k - z')$ and $r = [(x_k - x')^2 + (y_k - y')^2 + (z_k - z')^2]^{1/2}$, and after some algebra, we find discrete forms for each components of the magnetic tensor:

$$H_{xx}(\mathbf{r}') =$$

$$3H_0 \sum_{k=1}^{N_m} \chi_k \left\{ \frac{[-l_x(x_k - x') - t]r^2 + 2(x' - x_k)^2 t}{r^7} + [l_x - \frac{3t(x_k - x')}{r^2}] \frac{(x' - x_k)}{r^5} \right\} \Delta x \Delta y \Delta z, \tag{4.15}$$

$$H_{xy}(\mathbf{r}') =$$

$$3H_0 \sum_{k=1}^{N_m} \chi_k \left\{ \frac{-l_y(x_k - x')r^2 - 2(y' - y_k)(x_k - x')t}{r^7} + [l_x - \frac{3t(x_k - x')}{r^2}] \frac{(y' - y_k)}{r^5} \right\} \Delta x \Delta y \Delta z, \tag{4.16}$$

$$H_{xz}(\mathbf{r}') =$$

$$3H_0 \sum_{k=1}^{N_m} \chi_k \left\{ \frac{-l_z(x_k - x')r^2 - 2(z' - z_k)(x_k - x')t}{r^7} + [l_x - \frac{3t(x_k - x')}{r^2}] \frac{(z' - z_k)}{r^5} \right\} \Delta x \Delta y \Delta z, \tag{4.17}$$

$$H_{yx}(\mathbf{r}') =$$

$$3H_0 \sum_{k=1}^{N_m} \chi_k \left\{ \frac{-l_x(y_k - y')r^2 - 2(x' - x_k)(y_k - y')t}{r^7} + [l_y - \frac{3t(y_k - y')}{r^2}] \frac{(x' - x_k)}{r^5} \right\} \Delta x \Delta y \Delta z, \tag{4.18}$$

$$H_{yy}(\mathbf{r}') =$$

$$3H_0 \sum_{k=1}^{N_m} \chi_k \left\{ \frac{[-l_y(y_k - y') - t]r^2 + 2(y' - y_k)^2 t}{r^7} + [l_y - \frac{3t(y_k - y')}{r^2}] \frac{(y' - y_k)}{r^5} \right\} \Delta x \Delta y \Delta z, \tag{4.19}$$

$$H_{yz}(\mathbf{r}') =$$

$$3H_0 \sum_{k=1}^{N_m} \chi_k \left\{ \frac{-l_z(y_k - y')r^2 - 2(z' - z_k)(y_k - y')t}{r^7} + [l_y - \frac{3t(y_k - y')}{r^2}] \frac{(z' - z_k)}{r^5} \right\} \Delta x \Delta y \Delta z, \quad (4.20)$$

$$H_{zx}(\mathbf{r}') =$$

$$3H_0 \sum_{k=1}^{N_m} \chi_k \left\{ \frac{-l_x(z_k - z')r^2 - 2(x' - x_k)(z_k - z')t}{r^7} + [l_z - \frac{3t(z_k - z')}{r^2}] \frac{(x' - x_k)}{r^5} \right\} \Delta x \Delta y \Delta z, \quad (4.21)$$

$$H_{zy}(\mathbf{r}') =$$

$$3H_0 \sum_{k=1}^{N_m} \chi_k \left\{ \frac{-l_y(z_k - z')r^2 - 2(y' - y_k)(z_k - z')t}{r^7} + [l_z - \frac{3t(z_k - z')}{r^2}] \frac{(y' - y_k)}{r^5} \right\} \Delta x \Delta y \Delta z, \quad (4.22)$$

$$H_{zz}(\mathbf{r}') =$$

$$3H_0 \sum_{k=1}^{N_m} \chi_k \left\{ \frac{[-l_z(z_k - z') - t]r^2 + 2(z' - z_k)^2 t}{r^7} + [l_z - \frac{3t(z_k - z')}{r^2}] \frac{(z' - z_k)}{r^5} \right\} \Delta x \Delta y \Delta z. \quad (4.23)$$

Equations (4.10) to (4.12) will be used to model magnetic vector data and equations (4.15) to (4.23) will be used for modeling magnetic tensor components.

4.2 Inversion methodology

The regularized inversion is based on the minimization of Tikhonov parametric functional $P^{\alpha}(\mathbf{m})$ as follows:

$$P^{\alpha}(\mathbf{m}) = \phi(\mathbf{m}) + \alpha s(\mathbf{m}) \rightarrow \min, \quad (4.24)$$

where $\phi(\mathbf{m})$ is a misfit functional calculated as L2 norm of the difference between the observed data and the predicted data, $s(\mathbf{m})$ is a stabilizing functional, and α is the regularization parameter, which balances the misfit and stabilizing functionals (Zhdanov, 2002). The data and model weights are introduced in equation (4.24) using data and model weighting matrices. These weighting matrices reweight the original inverse problem in logarithmic space so as to reduce the dynamic range of both the data and

model parameters. As previously discussed, we consider induced magnetization only. We also assume that anomalous magnetization is caused by paramagnetic material located within nonmagnetic host rocks. It follows that we need enforce positivity constraints on the susceptibility so as to obtain physically meaningful solutions.

In our implementation, all data and model weights are based upon their integrated sensitivity (Zhdanov, 2002). Our weighting functions provide equal sensitivity of the different components of observed data to the cells located at different depths and horizontal positions. Thus, our weighting functions automatically introduce appropriate corrections for the vertical and horizontal distribution of the susceptibility. This is one of the main differences between our approach, and the geometric weighting functions developed by Li and Oldengurg (1996).

All geological constraints manifest themselves as regularization that can be quantified through a choice of data weights, model upper and lower bounds, model weights, a priori models, and the type of stabilizing functional. The latter incorporates information about the class of models used in inversion. The choice of stabilizing functional should be based on the user's geological knowledge and prejudice. In this section we will briefly describe different smooth and focusing stabilizers in order to demonstrate the results from the 3-D inversion of magnetic vector and tensor data produced by each.

A minimum norm (MN) stabilizer will seek to minimize the norm of the difference between the current model and an a priori model:

$$s_{MN}(\mathbf{m}) = \iiint_V (\mathbf{m} - \mathbf{m}_{apr})^2 dv, \tag{4.25}$$

and usually produce a relatively smooth model.

The first derivative (FD) stabilizer implicitly introduces smoothness as the first spatial derivatives of the model parameters:

$$s_{FD}(\mathbf{m}) = \iiint_V (\nabla\mathbf{m} - \nabla\mathbf{m}_{apr})^2 dv, \tag{4.26}$$

and can result spurious oscillations and artifacts when the model parameters are discontinuous. A combination of stabilizers (4.25) and (4.26) are often used (e.g., Li and Oldenburg, 1996).

However, very little geology exhibits smooth susceptibility distributions. Geology is typically characterized by sharp boundaries of contrasting susceptibility, for example, between and ore deposit and host rock, or across a discontinuity. As such, stabilizer (4.25) and (4.26) or their combinations produce results that bear no physical relevance to the actual geology. Portniaguine and Zhdanov (1999) introduced focusing stabilizers that made it possible to recover models with sharper boundaries and contrasts. In this thesis, we consider the minimum support (MS) stabilizer:

$$s_{MS}(\mathbf{m}) = \iiint_V \frac{(\mathbf{m}-\mathbf{m}_{apr})^2}{(\mathbf{m}-\mathbf{m}_{apr})^2+e^2} dv, \tag{4.27}$$

where e is a focusing parameter introduced to avoid singularity when $\mathbf{m} = \mathbf{m}_{apr}$. The minimum support stabilizer minimizes the volume with nonzero departures from the a priori model, effectively recovering compact bodies. Thus, a smooth distribution of all model parameters with a small deviation from the a priori model is penalized.

While variations of equation (4.27) were derived in Zhdanov (2002, 2009), we base our solution on the reweighted regularized conjugate gradient method (RRCG) (Zhdanov, 2002), which is easier to implement numerically.

In numerical dressing, the corresponding parametric functional can be written as follows:

$$P^{\alpha}(\mathbf{m}) = (\mathbf{W}_{\mathrm{d}}\mathbf{A}\mathbf{m} - \mathbf{W}_{\mathrm{d}}\mathbf{d})^{T}(\mathbf{W}_{\mathrm{d}}\mathbf{A}\mathbf{m} - \mathbf{W}_{\mathrm{d}}\mathbf{d})$$

$$+\alpha\left(\mathbf{W}_{e}\mathbf{W}_{m}\mathbf{m} - \mathbf{W}_{e}\mathbf{W}_{m}\mathbf{m}_{apr}\right)^{T}\left(\mathbf{W}_{e}\mathbf{W}_{m}\mathbf{m} - \mathbf{W}_{e}\mathbf{W}_{m}\mathbf{m}_{apr}\right), \quad (4.28)$$

where $\mathbf{W}_{\mathrm{d}}$ is the weighting matrix for the data, and $\mathbf{W}_{m}$ is the diagonal matrix for weighting the model parameters based on integrated sensitivity:

$$\mathbf{W}_{m} = \mathbf{diag}(\mathbf{F}^{T}\mathbf{F})^{1/4}. \quad (4.29)$$

Matrix $\mathbf{W}_{e}$ is a diagonal matrix, determined by the discrete values of the model parameters, m_i, representing the action of the minimum support stabilizer (Zhdanov, 2002):

$$\mathbf{W}_{e} = \mathbf{diag}[w_{e}] = \mathbf{diag}\left[\frac{1}{(m_i^2+e^2)^{1/2}}\right], \quad (4.30)$$

where e is a small number (focusing parameter).

The minimization problem (4.24) can be reformulated using a space of weighted parameters:

$$\mathbf{m}^{w} = \mathbf{W}\mathbf{m} = \mathbf{W}_{e}\mathbf{W}_{m}\mathbf{m}. \quad (4.31)$$

Equation (4.28) can be rewritten as follows:

$$P^{\alpha}(\mathbf{m}) = (\mathbf{A}^{w}\mathbf{m}^{w} - \mathbf{d})^{T}(\mathbf{A}^{w}\mathbf{m}^{w} - \mathbf{d}) + \alpha\left(\mathbf{m}^{w} - \mathbf{m}_{apr}^{w}\right)^{T}\left(\mathbf{m}^{w} - \mathbf{m}_{apr}^{w}\right), \quad (4.32)$$

where $\mathbf{A}^{w}$ is a new forward operator in the space of weighted parameters, which can be related to the forward operator $\mathbf{A}$ in the original space as

$$\mathbf{A}^{w} = \mathbf{A}\mathbf{W}^{-1} = \mathbf{A}\mathbf{W}_{m}^{-1}\mathbf{W}_{e}^{-1}. \quad (4.33)$$

The algorithm of the reweighted regularized conjugate gradient method to solve the minimization of parametric functional (4.32) is given as follows:

$$\mathbf{r}_{n}^{w} = \mathbf{A}^{w}\mathbf{m}_{n}^{w} - \mathbf{d} = \mathbf{A}\mathbf{m}_{n} - \mathbf{d}, \quad (4.34)$$

$$\mathbf{l}_{wn}^{\alpha_n} = \mathbf{F}_{wn}^{T}\mathbf{r}_{n}^{w} + \alpha_{n}(\mathbf{m}_{n}^{wn} - \mathbf{m}_{apr}^{wn}), \quad (4.35)$$

$$\beta_n^{\alpha_n} = \| \boldsymbol{l}_{wn}^{\alpha_n} \|_M^2 / \| \boldsymbol{l}_{w(n-1)}^{\alpha_{n-1}} \|_M^2, \tilde{\boldsymbol{l}}_{wn}^{\alpha_n} = \boldsymbol{l}_{wn}^{\alpha_n} + \beta_n^{\alpha_n} \boldsymbol{l}_{w(n-1)}^{\alpha_{n-1}}, \tilde{\boldsymbol{l}}_{w0}^{\alpha_0} = \boldsymbol{l}_{w0}^{\alpha_0}, \quad (4.36)$$

$$k_n^{\alpha_n} = (\tilde{\boldsymbol{l}}_{wn}^{\alpha_n\,T} \tilde{\boldsymbol{l}}_{wn}^{\alpha_n}) / \left[\tilde{\boldsymbol{l}}_{wn}^{\alpha_n\,T} (\mathbf{F}_{wn}^T \mathbf{F}_{wn} + \alpha_n \mathbf{I}) \tilde{\boldsymbol{l}}_{wn}^{\alpha_n} \right], \quad -$$

(4.37)

$$\mathbf{m}_{n+1}^{w_n} = \mathbf{m}_n^{w_n} - k_n^{\alpha_n} \tilde{\boldsymbol{l}}_{wn}^{\alpha_n}, \mathbf{m}_{n+1} = \mathbf{W}_n^{-1} \mathbf{m}_{n+1}^{w_n} = \mathbf{W}_m^{-1} \mathbf{W}_e^{-1} \mathbf{m}_{n+1}^{w_n}, \quad (4.38)$$

$$\mathbf{m}_{n+1}^{w_{n+1}} = \mathbf{W}_{e(n+1)} \mathbf{W}_m \mathbf{m}_{n+1}, \mathbf{s}_{n+1}^{w_{n+1}} = \left(\mathbf{m}_{n+1}^{w_{n+1}} - \mathbf{m}_{apr}^{w_{n+1}} \right), \mathbf{s}_{n+1}^{w_n} = \left(\mathbf{m}_{n+1}^{w_n} - \mathbf{m}_{apr}^{w_n} \right), \quad (4.39)$$

$$\gamma = \left\| \mathbf{s}_{n+1}^{w_{n+1}} \right\|^2 / \left\| \mathbf{s}_{n+1}^{w_n} \right\|^2, \alpha_{n+1} = \alpha_n, if\ \gamma \leq 1, and\ \alpha_{n+1} = \alpha_n / \gamma, if \gamma > 1. \quad (4.40)$$

The inversion proceeds to iterate until the residual error reaches a preset threshold, the decrease in error between multiple iteration is less than the preset threshold, or a maximum number of iterations is reached. Upon completion, the quality of the inversion is appraised by the data misfit and visual inspection of the model.

As we discussed above, in practical applications of the inversion method, some boundary conditions must be imposed on the variations of the model parameters:

$$m_i^- \leq m_i \leq m_i^+, \quad (4.41)$$

where m_i^- and m_i^+ are the lower and the upper limits of the model parameter m_i. However, during the process of minimization of the Tikhonov parametric functional, we can get the values of the model parameters outside the above boundaries. One way to solve this problem is to find the value of model parameters outside the interval and set them to some reasonable value inside the boundaries. Another way which is commonly used is by introducing the logarithmic transformation to arrive new model parameters:

$$\tilde{m}_i = ln \frac{m_i - m_i^-}{m_i^+ - m_i}. \quad (4.42)$$

The corresponding inverse transformation is given by the following formula:

$$m_i = \frac{m_i^- + m_i^+ \exp(\tilde{m}_i)}{1 + \tilde{m}_i}. \quad (4.43)$$

It is obvious that if we run the inversion process in the space of logarithmic model parameters, no matter how large or how small the value of $\tilde{m}_i$ will be, the inverse transformation by formula (4.43) will always keep the value of m_i exactly within the intervals formed by m_i^- and m_i^+. The RRCG algorithm for solving the inverse problem in the log space of the model parameters is presented in Appendix C.

4.3 Effects of topography on forward modeling and inversion

In practice of geophysical exploration, the real topography of observation surface is complicated. In some cases the surface is flat and in other cases it is often characterized by complex topography. Due to the development of technology, the accurate measurement of topography is not a big problem for us; for example we can obtain the topography data in a large area using GPS.

Most of magnetic inversion software available did not consider topography into inversion for simplicity. However, the assumption that the topography is flat will generate some artifacts in inversion when the topography is actually not flat. As discussed above, topography data are available now in cases of land, marine and air measurement. One important way to archive successful inversion is to add as much known information to the inversion as possible. Obviously, topography is important known information. As a result, the consideration of topography into inversion becomes both necessary and technically possible.

In synthetic examples of forward modeling and inversion, we will discrete the 3-D earth model into a grid of *N* cells. In the case that the surface is flat, we can just simply

divide the domain below the flat surface into a rectangular grid of cells. The idea of implementing topography into inversion is based on division of the domain below the curved surface into a grid of cells. The domain above this curved surface will not be involved in the forward modeling and inversion. In the computer program, we developed algorithms which can automatically divide the domain below the observed surface into the cells for inversion. In the subsequent model studies, we will present some inversion results considering topography both for magnetic vector data and magnetic tensor data.

4.4 Model studies

4.4.1 Model studies without topography

In this subsection, we will present several model studies for magnetic vector field inversion and magnetic tensor field inversion without considering topography. In the first part of this subsection, three models will be presented for magnetic vector field inversion. In the second part of this subsection, the same models for magnetic vector field will be tested for magnetic tensor field inversion.

4.4.1.1 Model studies for magnetic vector field

4.4.1.1.1 Model 1

This is a 3-D model with one anomalous body located 30 meters below the flat surface. The size of the anomalous body is 10m×60m×10m which extends from 90 m to 100 m in *x* (easting) direction, 20 m to 80 m in *y (northing)* direction and 30m to 40 m in *z (downward)* direction. The size of the research domain is 200m×100m×100m in *x, y* and *z* direction, respectively. The anomalous magnetic susceptibility is 1 in SI units. We

consider that inclination of inducing magnetic field is 90 degrees and the declination of the inducing magnetic field is 0. Figure 4.1 is an illustration of this model.

For this model, we simulated the corresponding magnetic vector field data H_x, H_y and H_z, we used these three independent components to do joint inversion. Figure 4.2 shows the 3-D image of the joint inversion result from H_x, H_y and H_z for model 1. Figure 4.3 shows the vertical section of the magnetic vector field inversion result at y=45 meters and the black outline in this figure indicates the true model. From this figure, we can see that the magnetic body is well recovered from magnetic vector field inversion. Also one can see that the inversion image is very compact by applying focusing inversion technique. Figure 4.4 shows the data fitting for this inversion where the left panel indicates the observed magnetic vector component and the right panel denotes the predicted data. The final normalized misfit between the observed data and the predicted data is 5%. Figure 4.5 is the convergence plot where the upper panel shows the behavior of normalized misfit and the lower panel indicates how Tikhonov parametric functional and misfit functional decreases with iteration number.

4.4.1.1.2 Model 2

This is a 3-D model with two anomalous bodies both located 30 meters below the flat surface. The size of the first anomalous body is 20m×60m×10m which extends from 40 m to 60 m in *x* (easting) direction, 20 m to 80 m in *y (northing)* direction and 30m to 40 m in *z (downward)* direction. The size of the second anomalous body is 20m×40m×10m which extends from 140 m to 160 m in *x* (easting) direction, 30 m to 70 m in *y (northing)* direction and 30m to 40 m in *z (downward)* direction. The size of the research domain is 200m×100m×100m in *x, y* and *z* direction, respectively. The

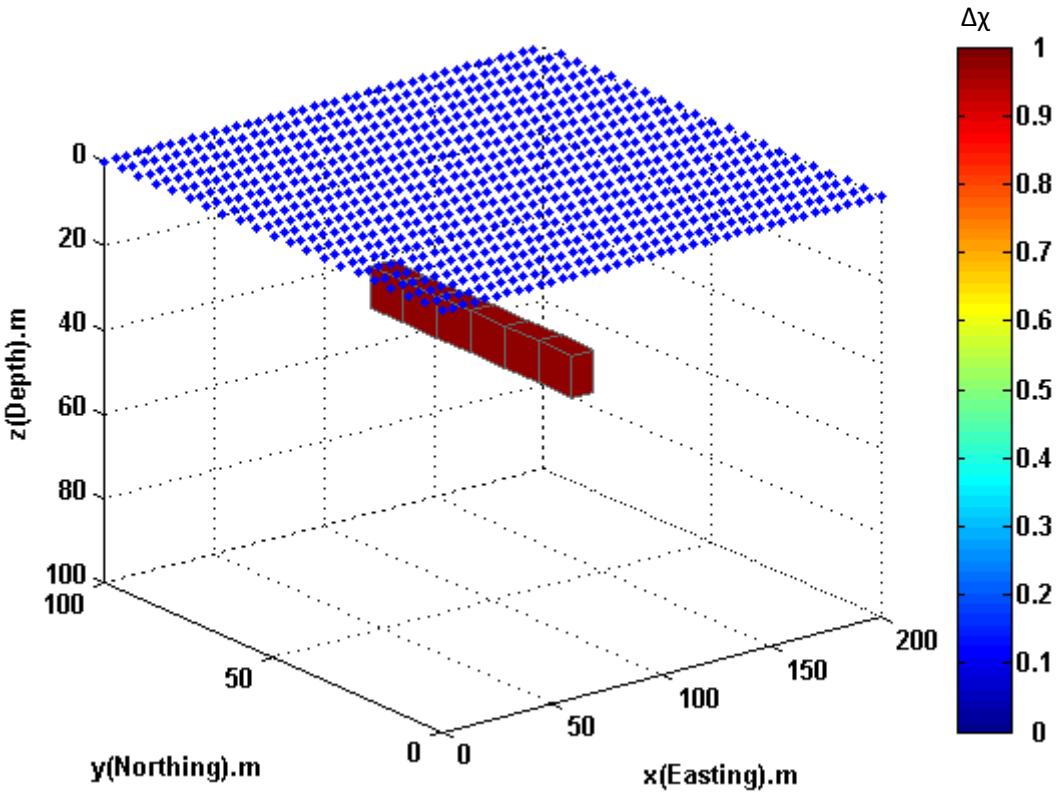

Figure 4.1. This figure shows model 1 with one anomalous magnetic body located below the subsurface. The blue dots in the surface denote the stations for magnetic vector field data measurement.

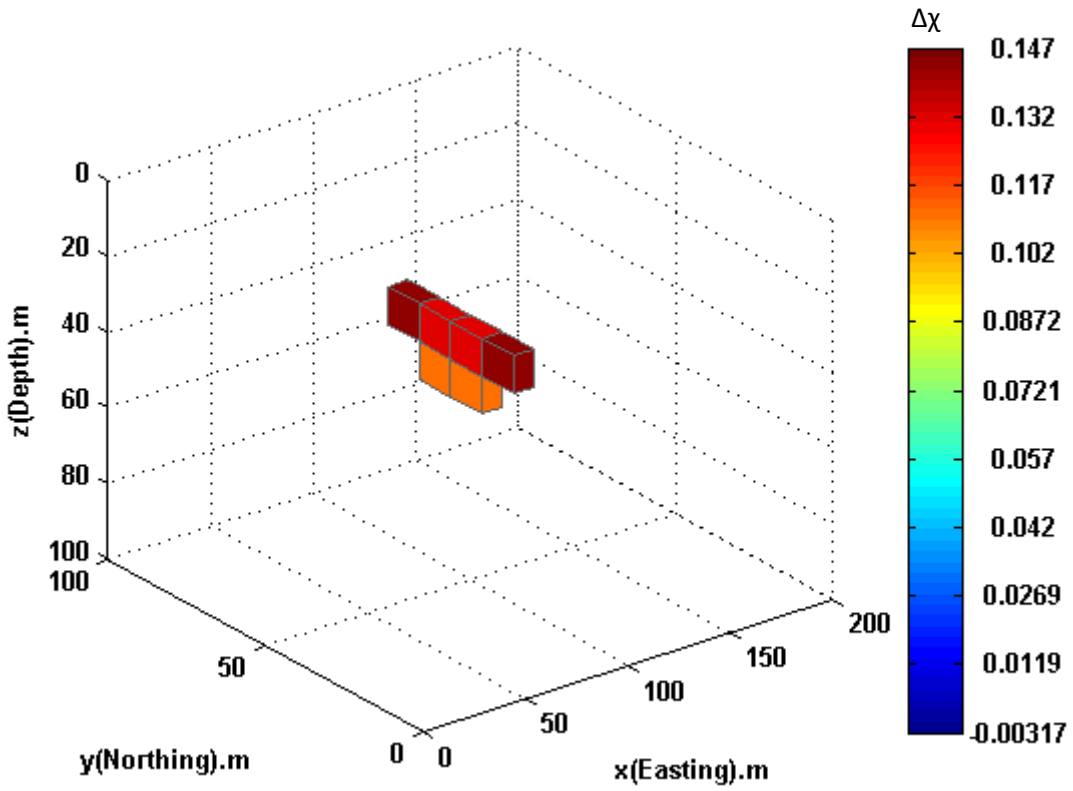

Figure 4.2. 3-D view of inversion result for magnetic vector inversion, model 1.

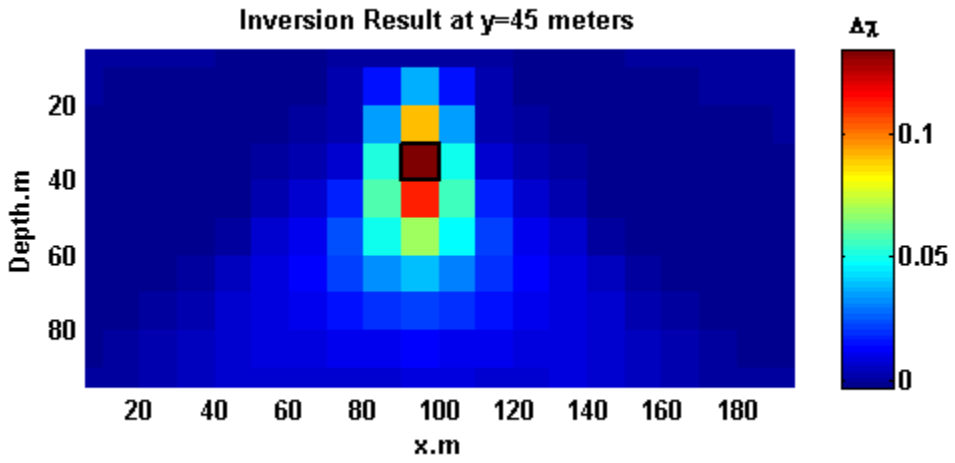

Figure 4.3. Vertical section of inversion result at y=45 meters for magnetic vector inversion, model 1.

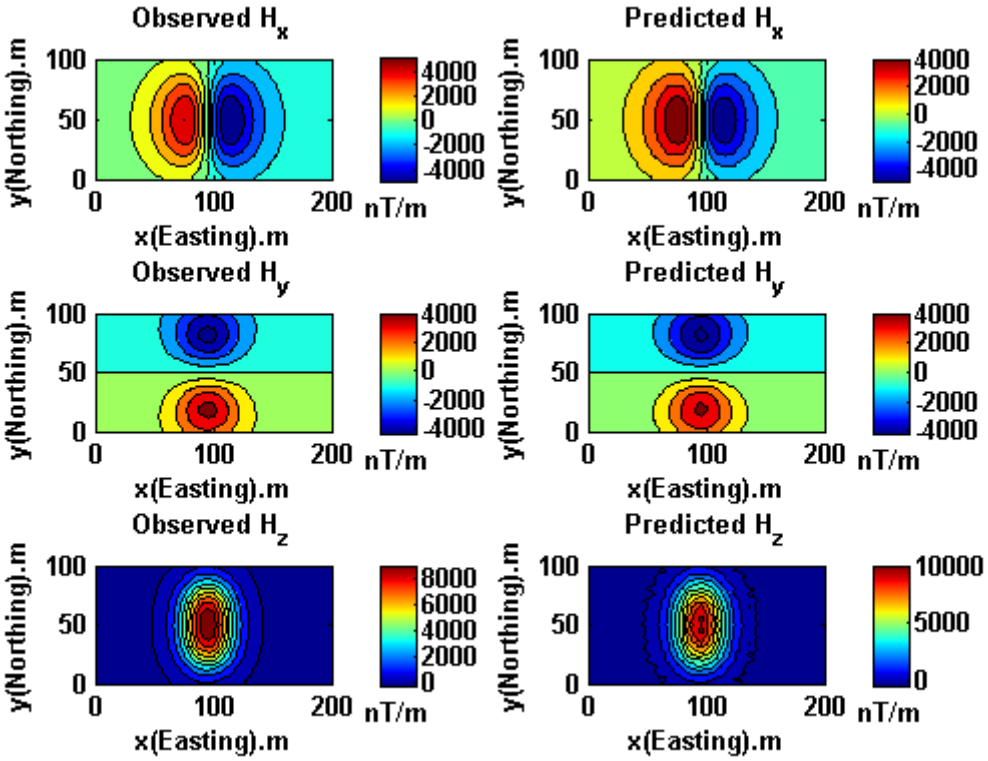

Figure 4.4. Data fitting of magnetic vector field components for model 1.

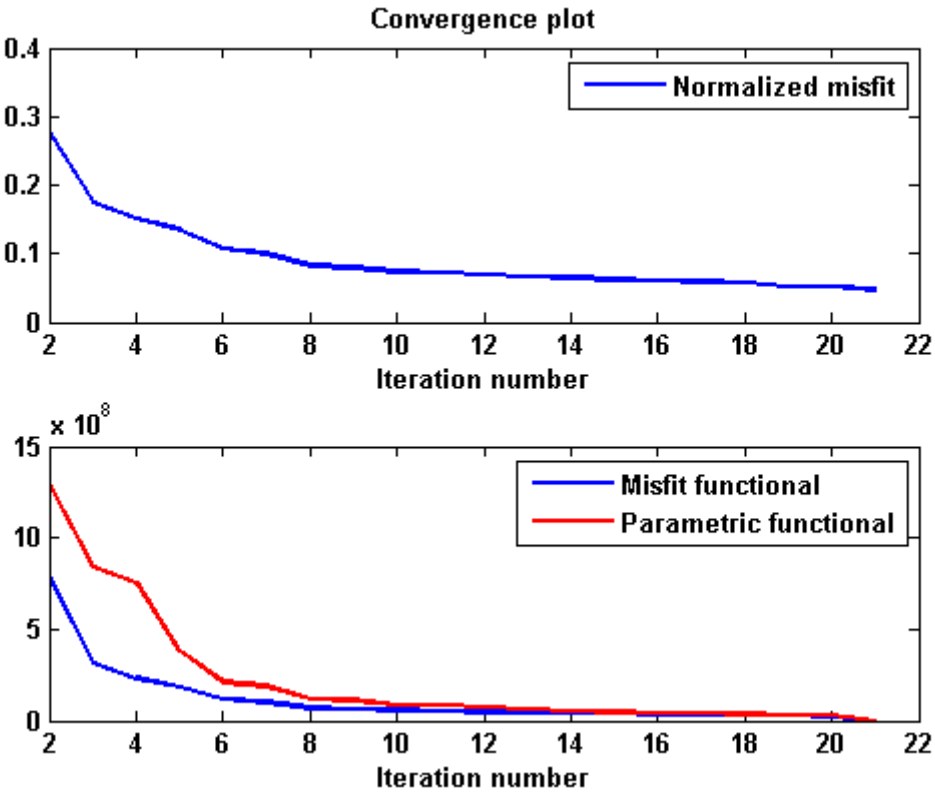

Figure 4.5. Convergence plot for magnetic vector field inversion, model 1.

anomalous magnetic susceptibility is 1 in SI units. We consider that inclination of inducing magnetic field is 90 degrees and the declination of the inducing magnetic field is 0. Figure 4.6 is an illustration of this model.

For this model, we simulated the corresponding magnetic vector field data H_x, H_y and H_z. We used these three independent components to do joint inversion. Figure 4.7 shows the 3-D image of the joint inversion result from H_x, H_y and H_z for model 2. Figure 4.8 shows the vertical section of the magnetic vector field inversion result at y=45 meters and the black outline in this figure indicates the true model. From this figure, we can see that both of these two magnetic bodies are well recovered from magnetic vector field inversion. Also one can see that the inversion image is very compact by applying focusing inversion technique. Figure 4.9 shows the data fitting for this inversion where the left panel indicates the observed magnetic vector component and the right panel denotes the predicted data. The final normalized misfit between the observed data and the predicted data is 5%. Figure 4.10 is the convergence plot where the upper panel shows the behavior of normalized misfit and the lower panel indicates how Tikhonov parametric functional and misfit functional decreases with iteration number.

4.4.1.1.3 Model 3

This is a 3-D model with one anomalous dyke locates 20 meters below the flat surface. The magnetic dyke extends from 60 m to 110 m in *x* (easting) direction, 20 m to 80 m in *y (northing)* direction and 20m to 70 m in *z (downward)* direction. The size of the research domain is 200m×100m×100m in *x, y* and *z* direction, respectively. The anomalous magnetic susceptibility is 1 in SI units. We consider that inclination of inducing magnetic field is 90 degrees and the declination of the inducing magnetic field

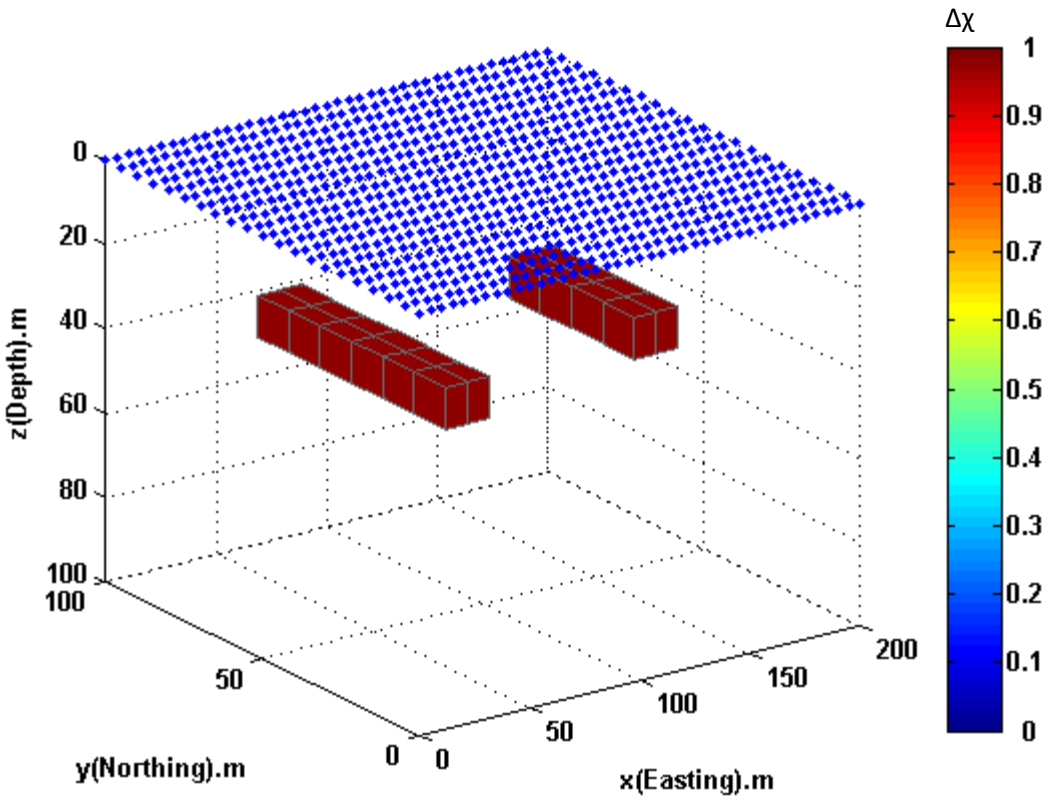

Figure 4.6. This figure shows model 2 with two anomalous magnetic bodies located below the subsurface. The blue dots in the surface denote the stations for magnetic vector field data measurement.

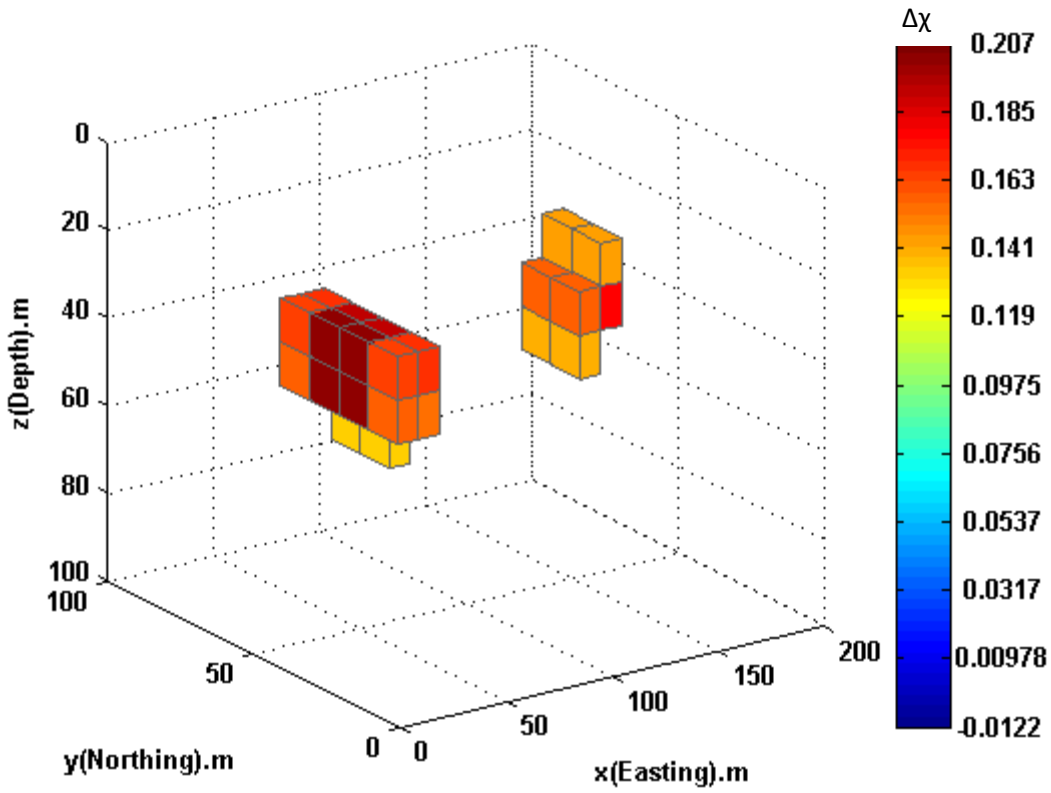

Figure 4.7. 3-D view of inversion result for magnetic vector inversion, model 2.

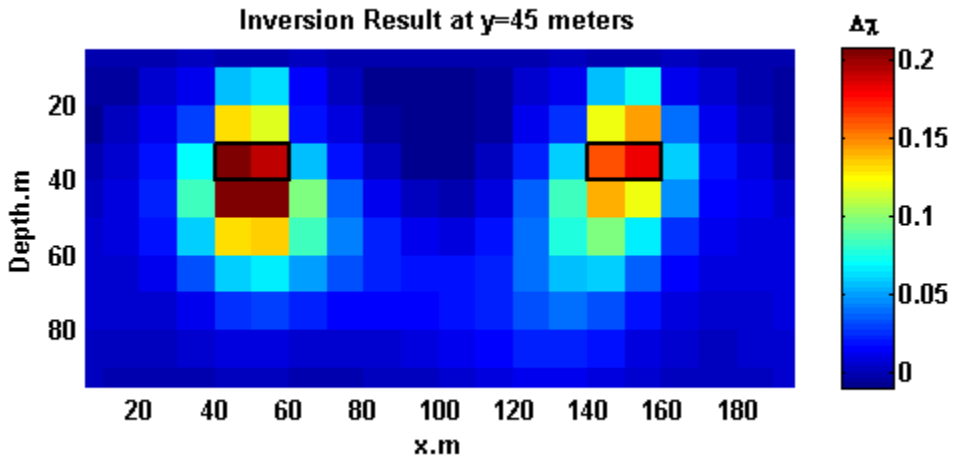

Figure 4.8. Vertical section of inversion result at y=45 meters for magnetic vector inversion, model 2.

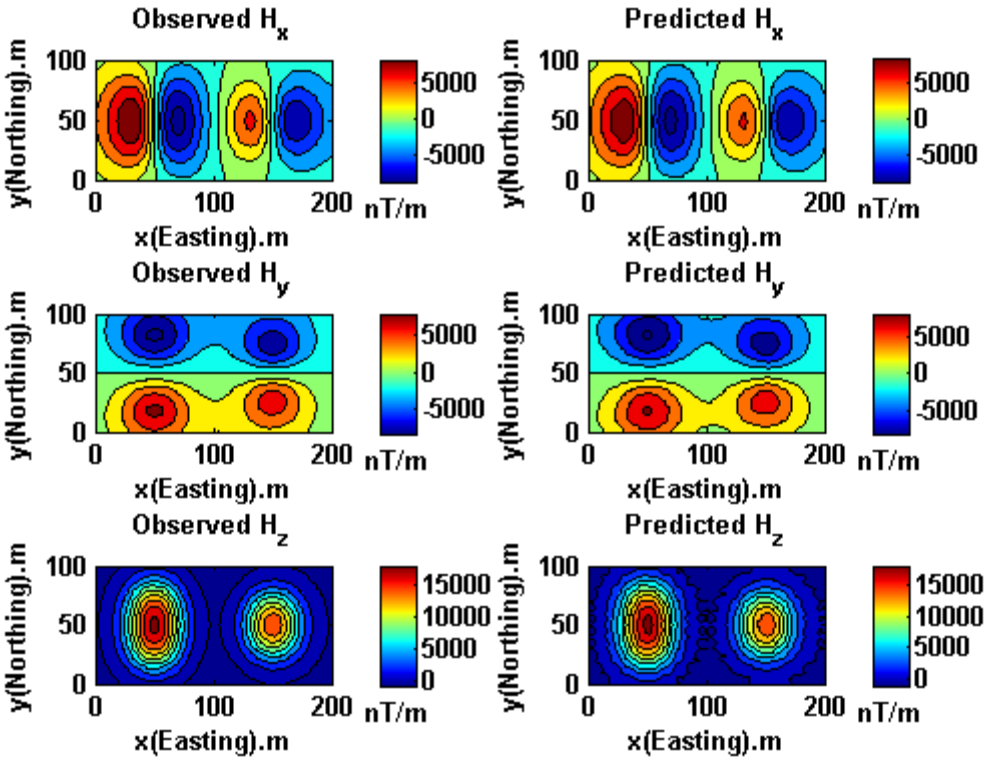

Figure 4.9. Data fitting of magnetic vector field components for model 2.

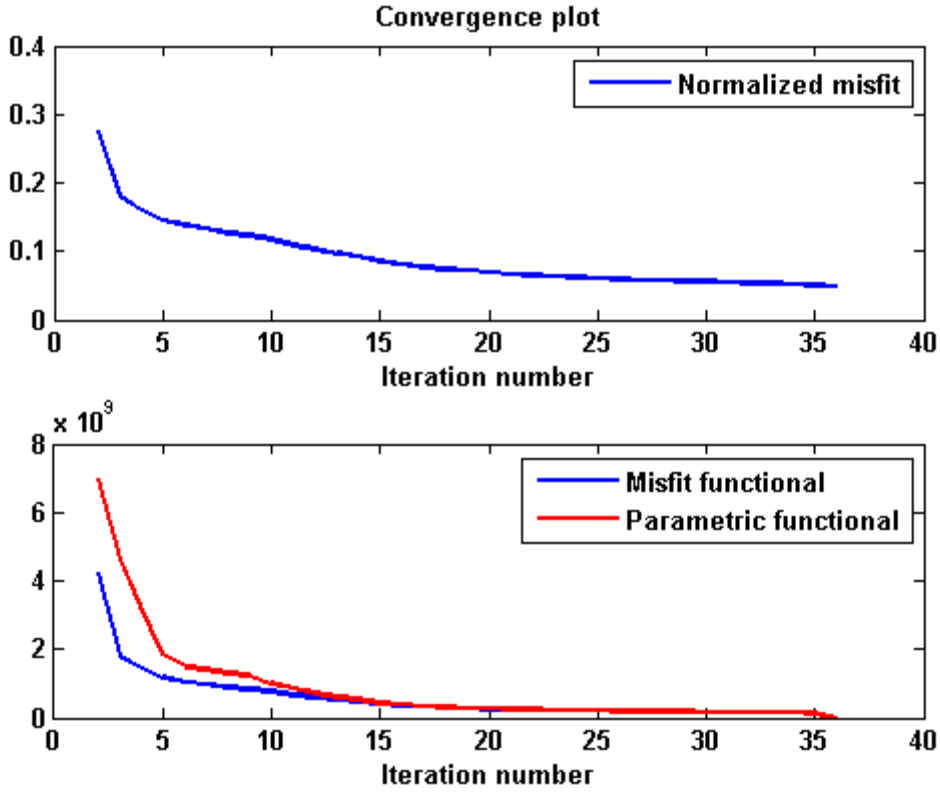

Figure 4.10. Convergence plot for magnetic vector field inversion, model 2.

is 0. Figure 4.11 is an illustration of this model.

For this model, we simulated the corresponding magnetic vector field data H_x, H_y and H_z, we used these three independent components to do joint inversion. Figure 4.12 shows the 3-D image of the joint inversion result from H_x, H_y and H_z for model 3. Figure 4.13 shows the vertical section of the magnetic vector field inversion result at y=45 meters and the black outline in this figure indicates the true model. From this figure, we can see that the magnetic dyke is well recovered from magnetic vector field inversion. Figure 4.14 shows the data fitting for this inversion where the left panel indicates the observed magnetic vector component and the right panel denotes the predicted data. The final normalized misfit between the observed data and the predicted data is 5%. Figure 4.15 is the convergence plot where the upper panel shows the behavior of normalized misfit and the lower panel indicates how Tikhonov parametric functional and misfit functional decreases with iteration number.

4.4.1.2 Model studies for magnetic tensor field

4.4.1.2.1 Model 1

This model is exactly the same as model 1 we used in the previous model study for magnetic vector field and the research domain is also the same. Figure 4.1 is an illustration of this model.

For this model, we simulated all magnetic tensor components. We used five independent components H_{xx}, H_{yx}, H_{zx}, H_{zy} and H_{zz} to do joint inversion. Figure 4.16 shows the 3-D image of the joint inversion result for model 1. Figure 4.17 shows the vertical section of the magnetic tensor field inversion result at y=45 meters and the black outline in this figure indicates the true model. From this figure, we can see that the

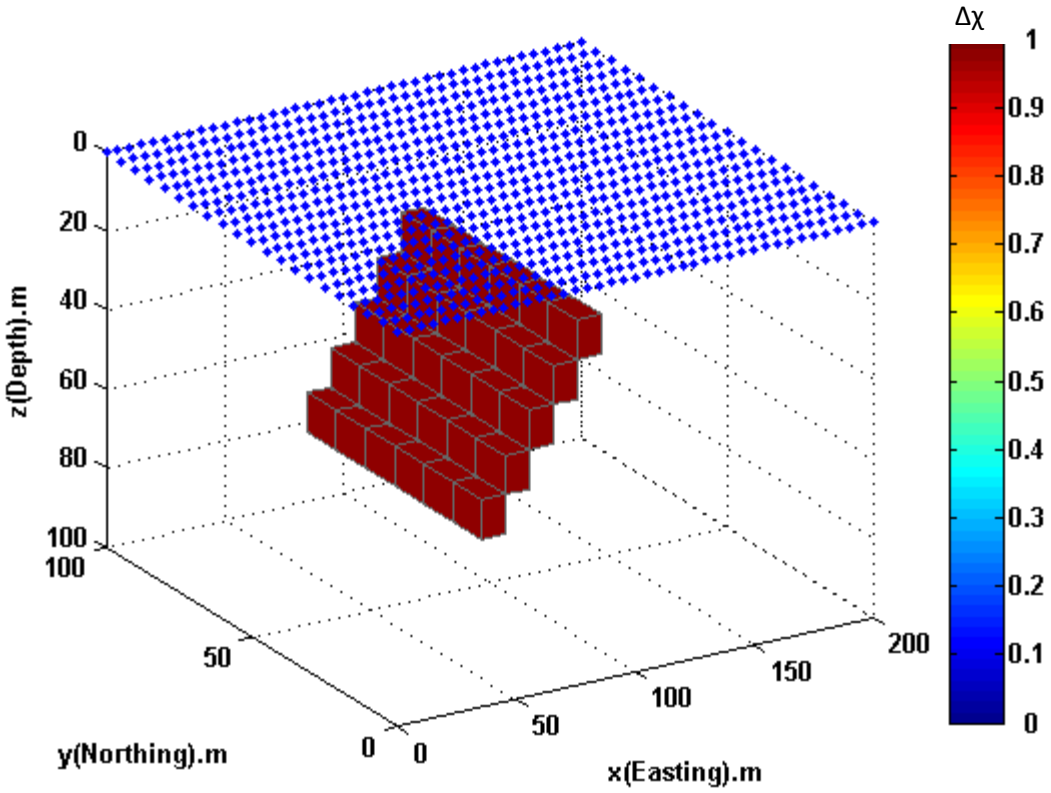

Figure 4.11. This figure shows model 3 with one magnetic dyke located below the subsurface. The blue dots in the surface denote the stations for magnetic vector field data measurement.

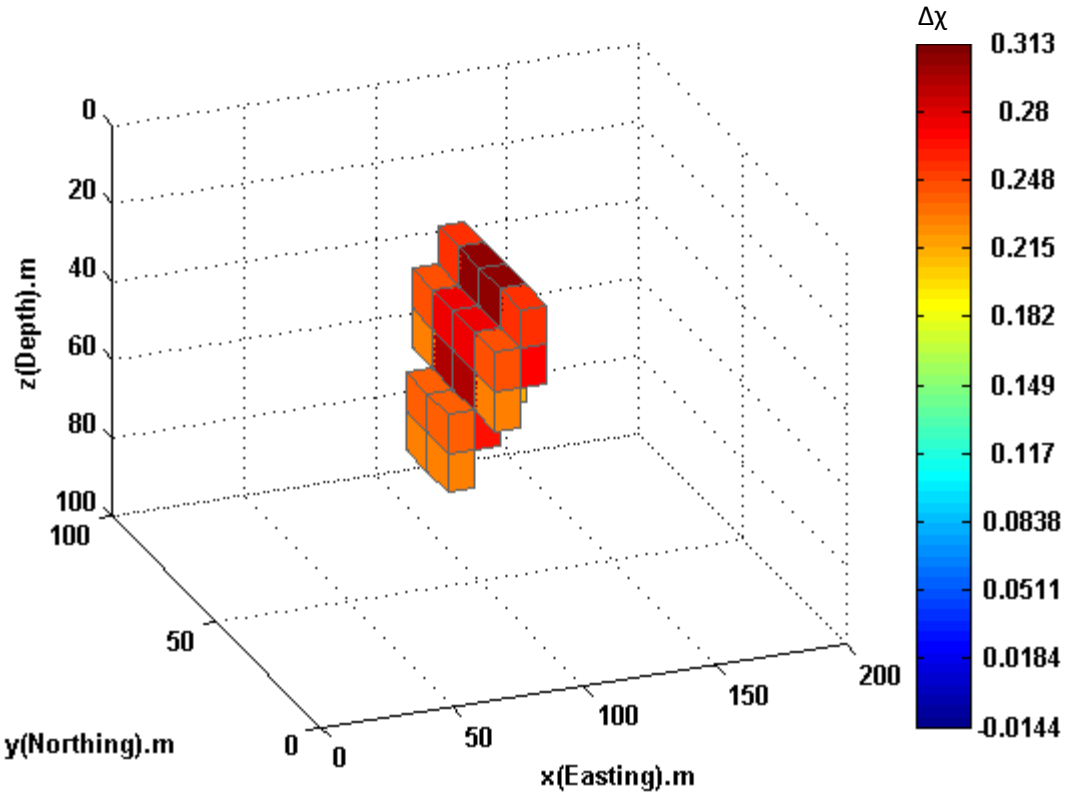

Figure 4.12. 3-D view of inversion result for magnetic vector inversion, model 3.

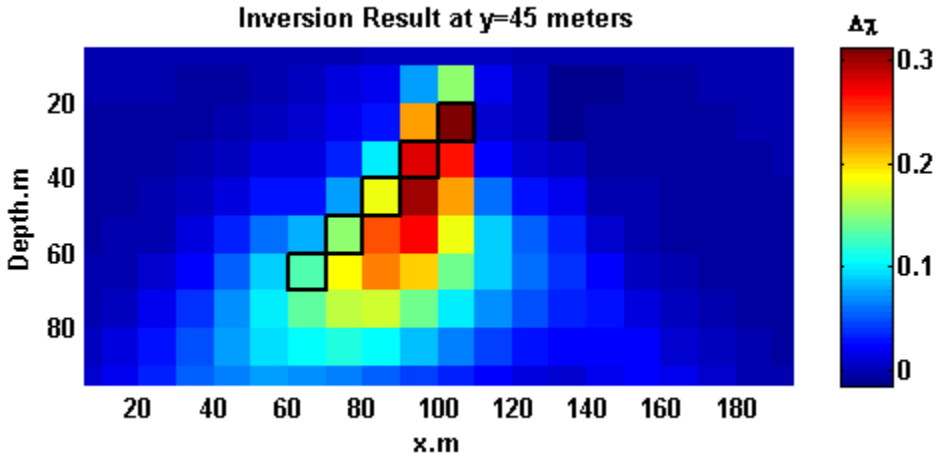

Figure 4.13. Vertical section of inversion result at y=45 meters for magnetic vector inversion, model 3.

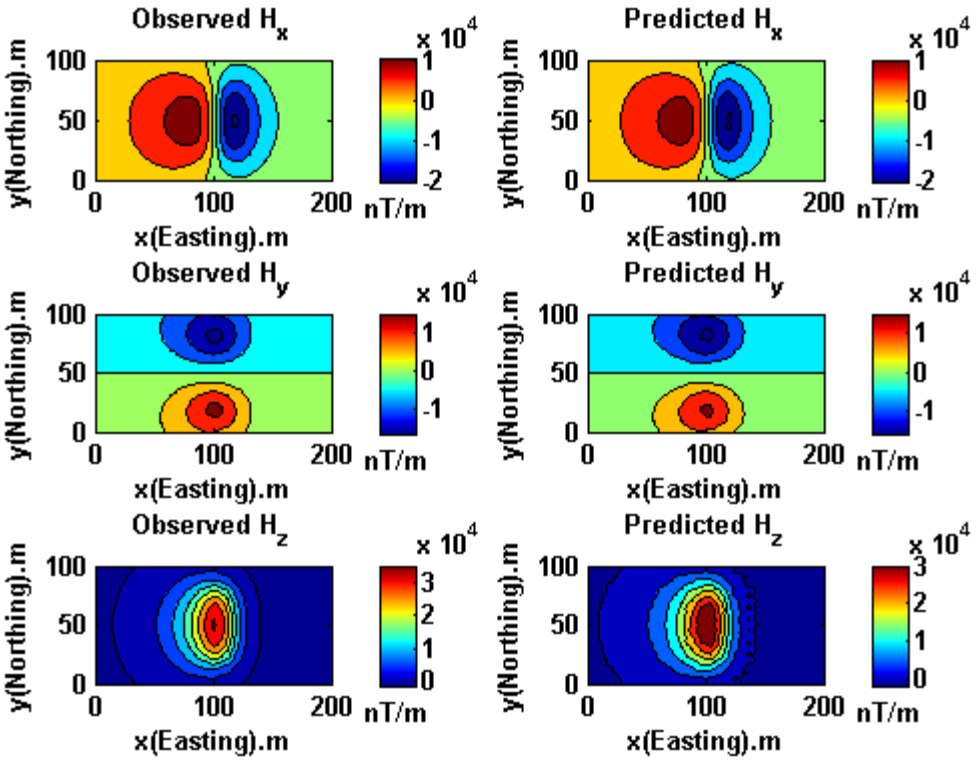

Figure 4.14. Data fitting of magnetic vector field components for model 2.

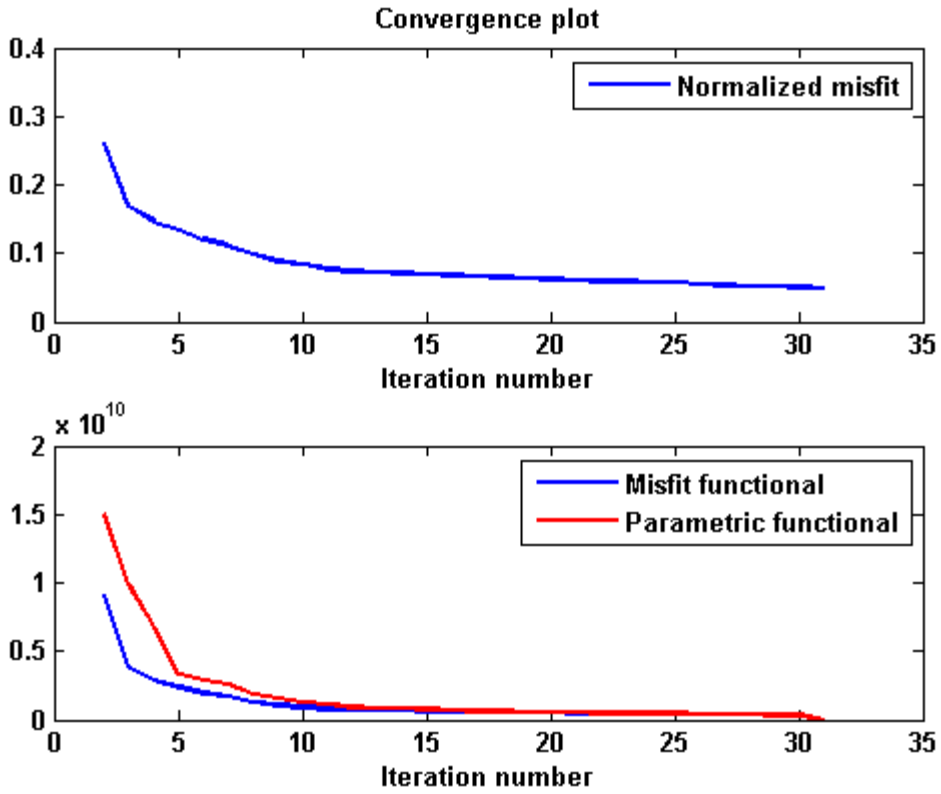

Figure 4.15. Convergence plot for magnetic vector field inversion, model 3.

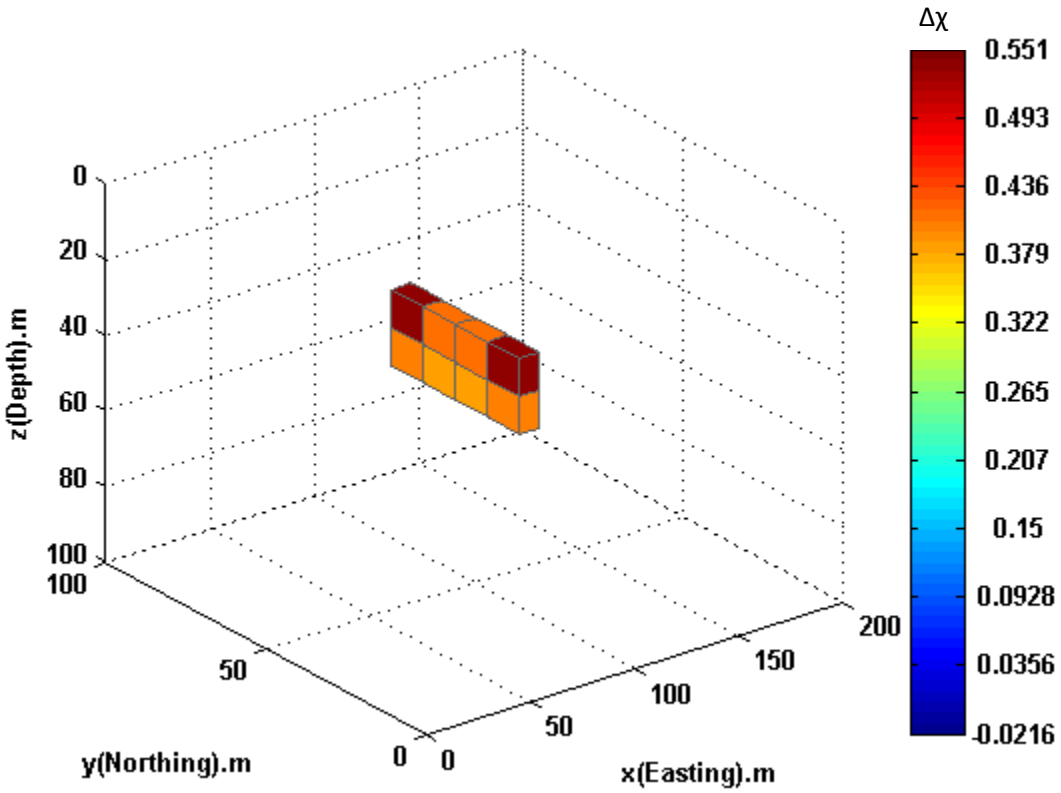

Figure 4.16. 3-D view of inversion result for magnetic tensor inversion, model 1.

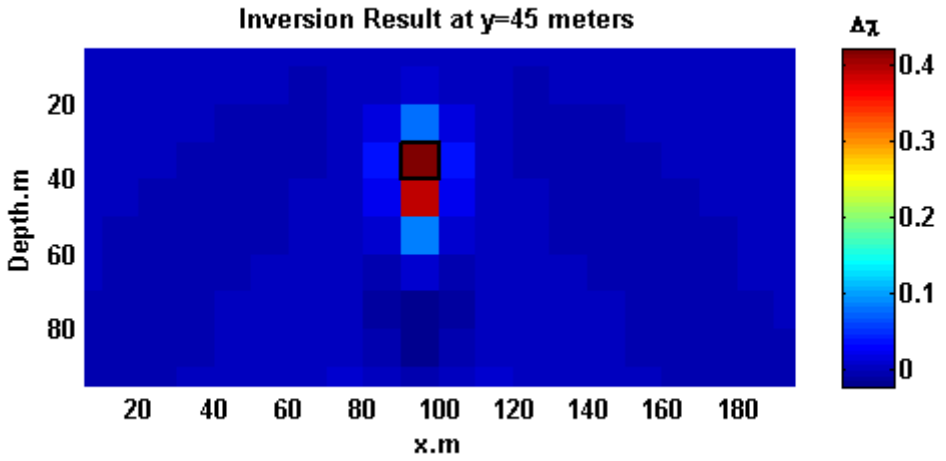

Figure 4.17. Vertical section of inversion result at y=45 meters for magnetic tensor field inversion, model 1.

magnetic body is well recovered from magnetic tensor field inversion. Also one can see that the inversion image is very compact by applying focusing inversion technique. Figure 4.18 and Figure 4.19 show the data fitting for this inversion where the left panel indicates the observed magnetic tensor component and the right panel denotes the predicted data. The final normalized misfit between the observed data and the predicted data is 5%. Figure 4.20 is the convergence plot where the upper panel shows the behavior of normalized misfit and the lower panel indicates how Tikhonov parametric functional and misfit functional decreases with iteration number.

4.4.1.2.2 Model 2

This model is exactly the same as model 2 we used in the previous model study for magnetic vector field and the research domain is also the same. Figure 4.6 is an illustration of this model.

For this model, we simulated all magnetic tensor components. We used five independent components H_{xx}, H_{yx}, H_{zx}, H_{zy} and H_{zz} to do joint inversion. Figure 4.21 shows the 3-D image of the joint inversion result for model 2. Figure 4.22 shows the vertical section of the magnetic tensor field inversion result at y=45 meters and the black outline in this figure indicates the true model. From this figure, we can see that the magnetic body is well recovered from magnetic tensor field inversion. Also one can see that the inversion image is very compact by applying focusing inversion technique. Figure 4.23 and Figure 4.24 show the data fitting for this inversion where the left panel indicates the observed magnetic tensor component and the right panel denotes the predicted data. The final normalized misfit between the observed data and the predicted data is 5%. Figure 4.25 is the convergence plot where the upper panel shows the behavior

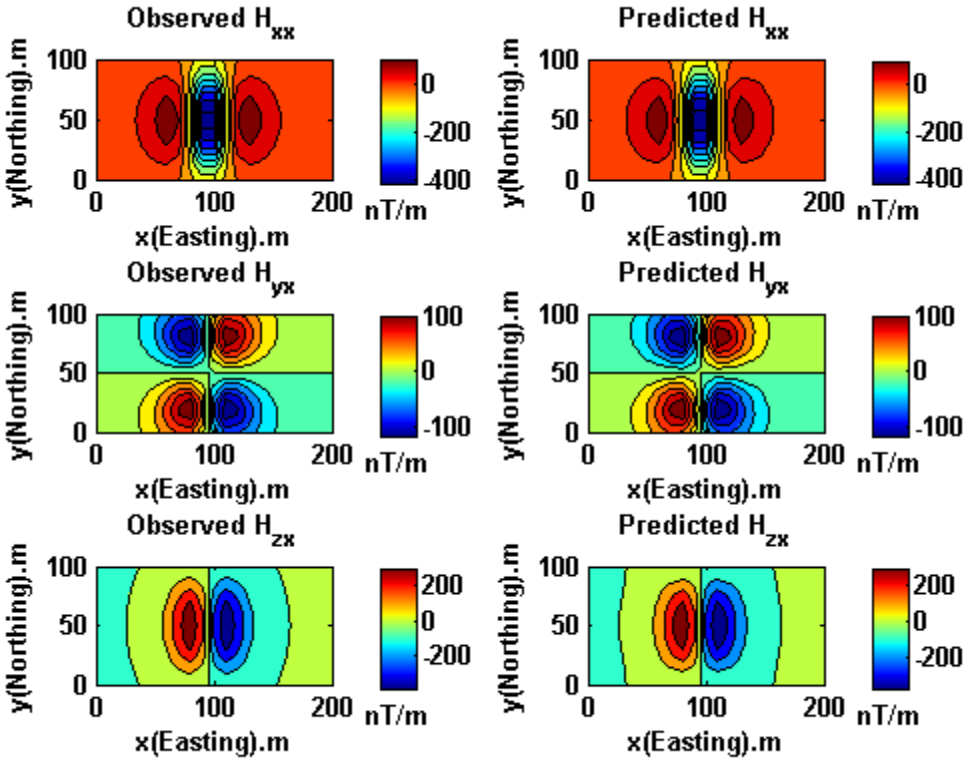

Figure 4.18. Data fitting of magnetic tensor field components for model 1.

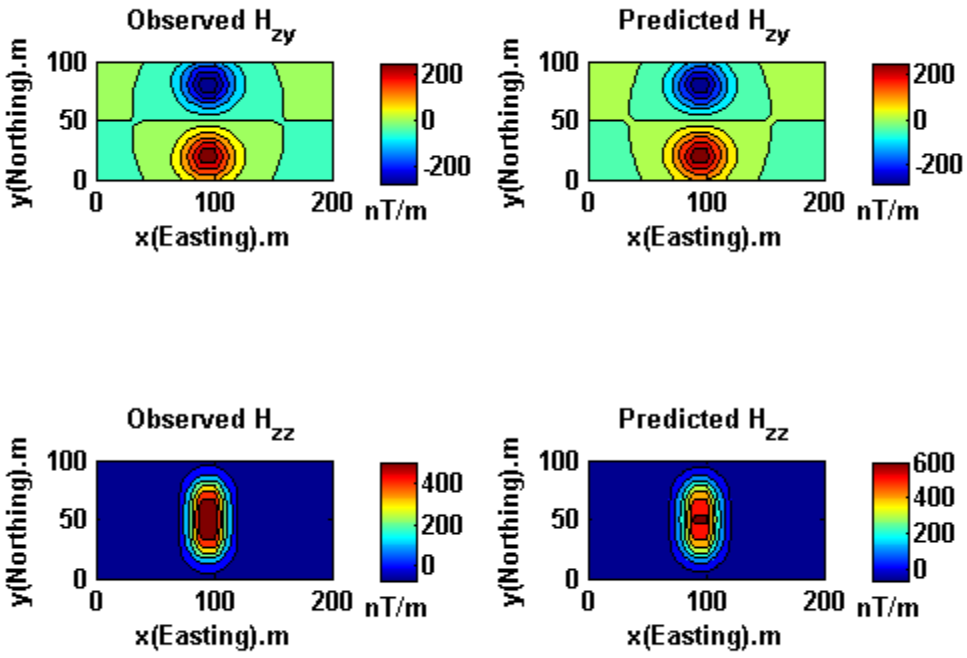

Figure 4.19. Data fitting of magnetic tensor field components for model 1.

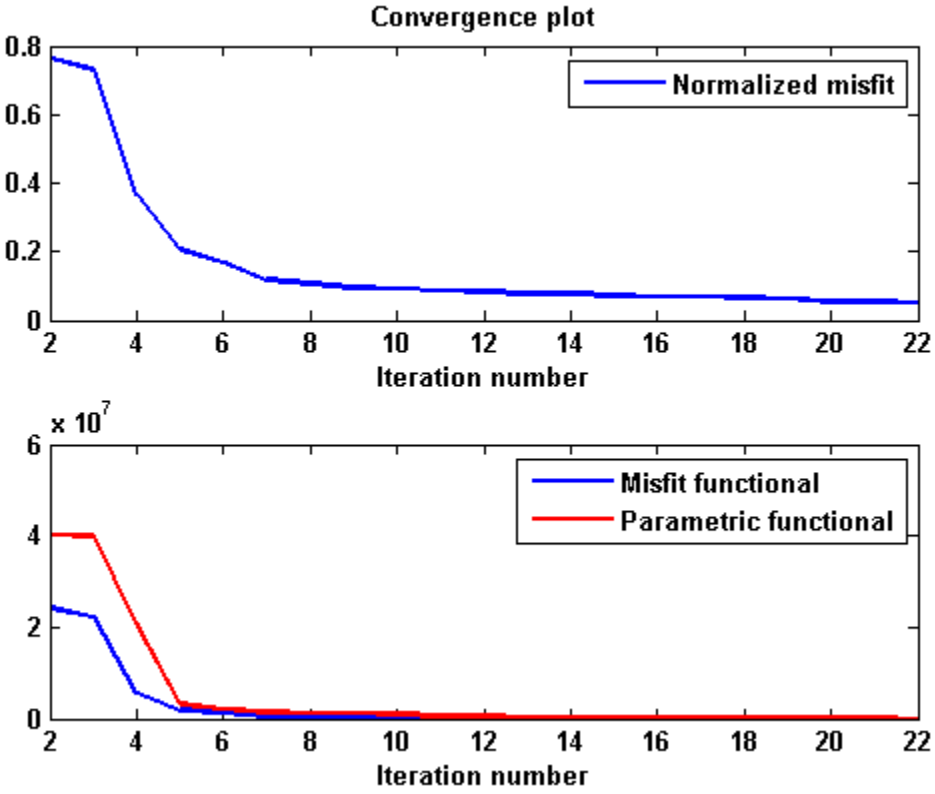

Figure 4.20. Convergence plot for magnetic tensor field inversion, model 1.

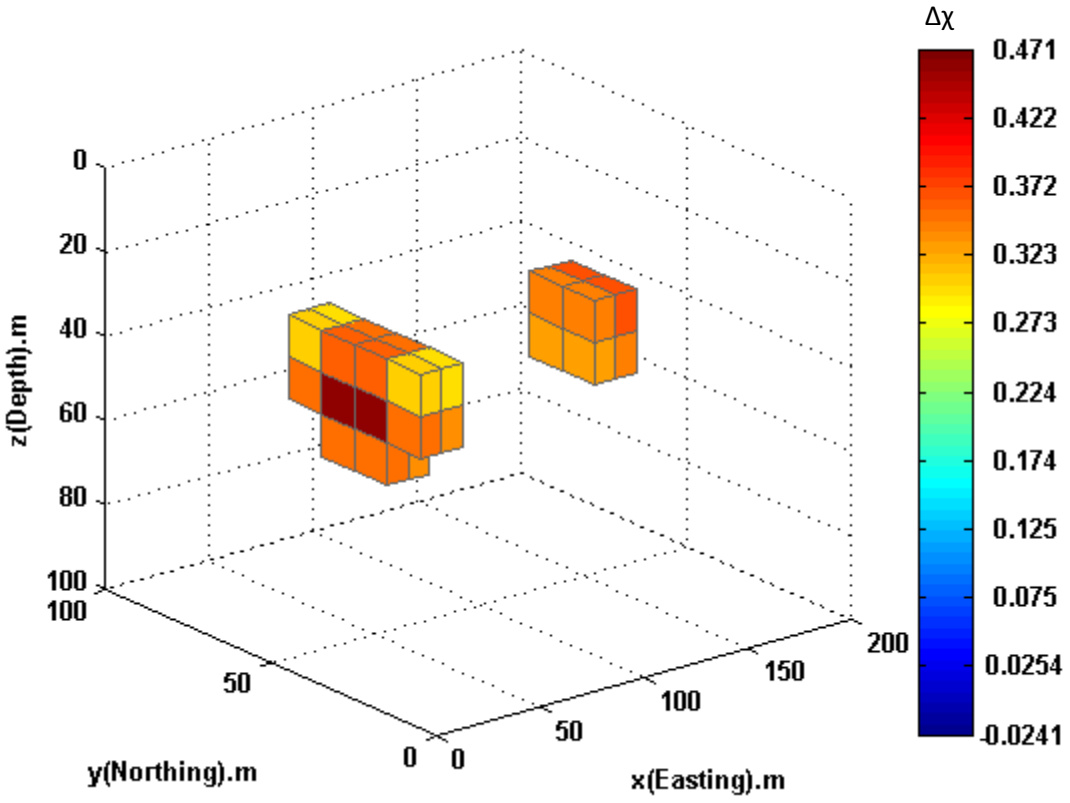

Figure 4.21. 3-D view of inversion result for magnetic tensor inversion, model 2.

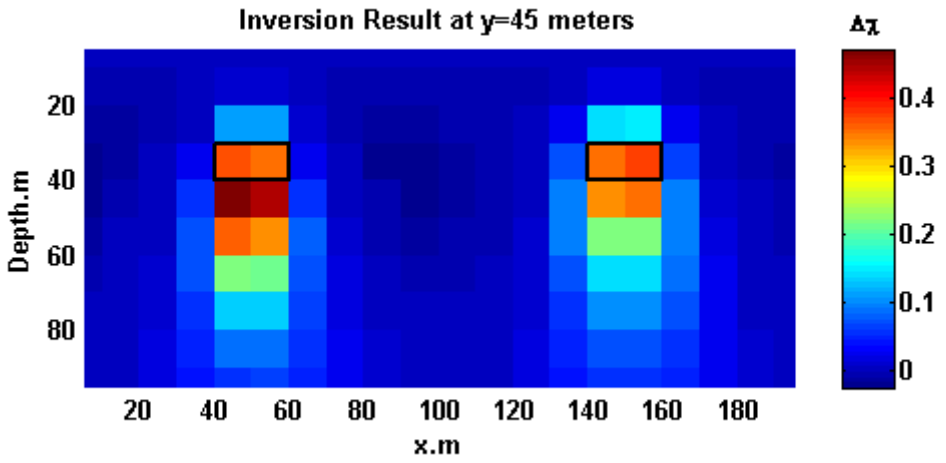

Figure 4.22. Vertical section of inversion result at y=45 meters for magnetic tensor inversion, model 2.

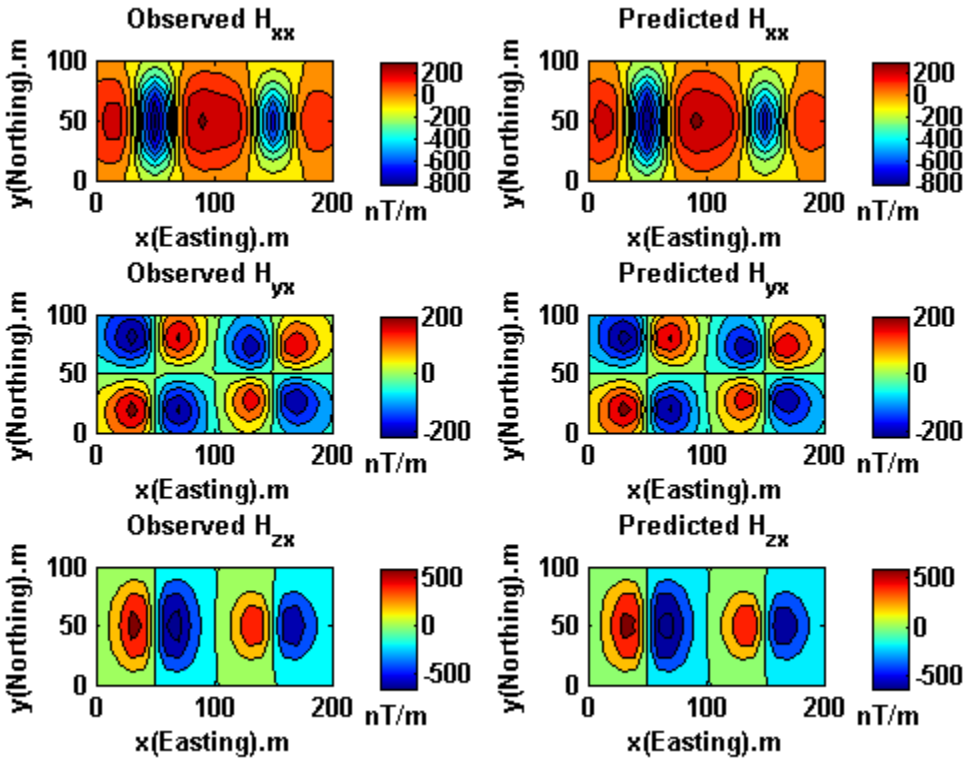

Figure 4.23. Data fitting of magnetic tensor field components for model 2.

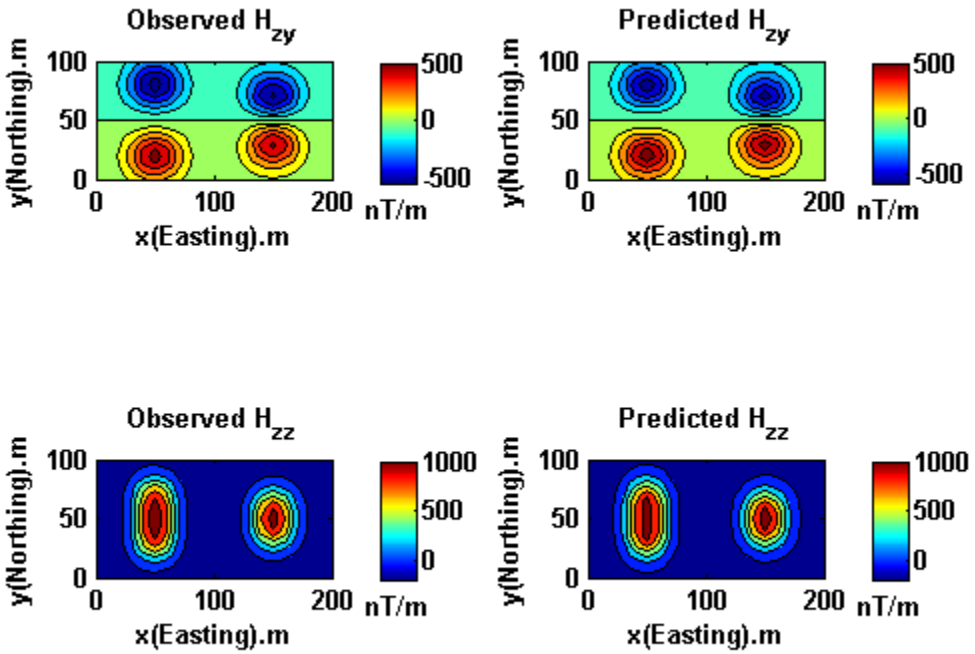

Figure 4.24. Data fitting of magnetic tensor field components for model 2.

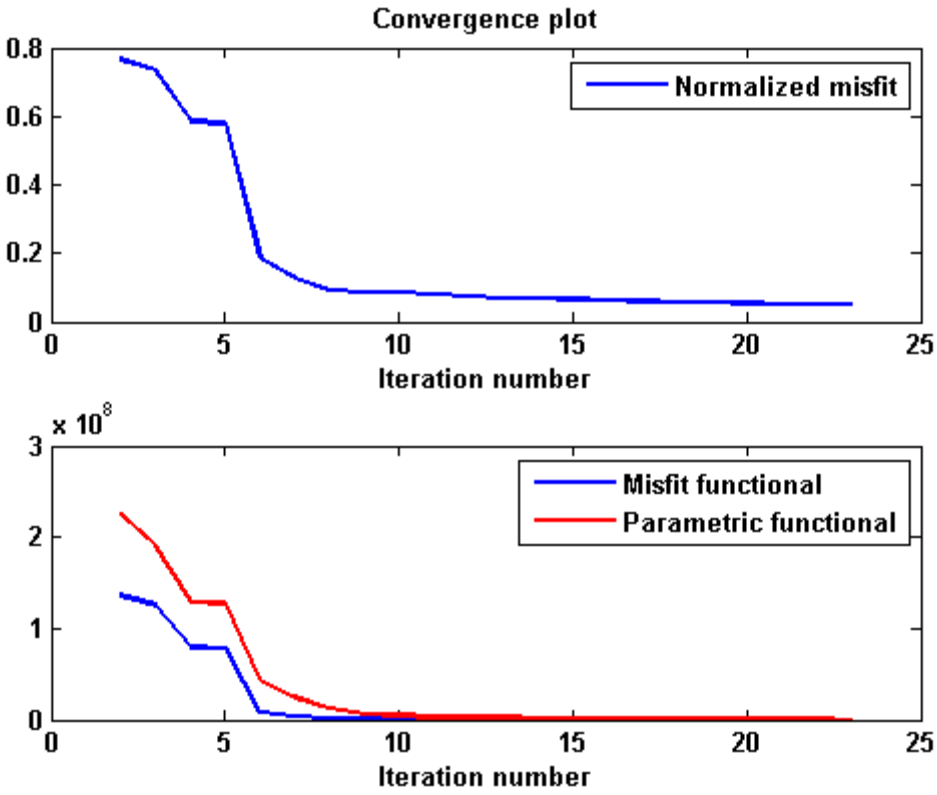

Figure 4.25. Convergence plot for magnetic tensor field inversion, model 2.

of normalized misfit and the lower panel indicates how Tikhonov parametric functional and misfit functional decreases with iteration number.

4.4.1.2.3 Model 3

This model is exactly the same as model 3 we used in the previous model study for magnetic vector field and the research domain is also the same. Figure 4.11 is an illustration of this model.

For this model, we simulated all magnetic tensor components. We used five independent components H_{xx}, H_{yx}, H_{zx}, H_{zy} and H_{zz} to do joint inversion. Figure 4.26 shows the 3-D image of the joint inversion result for model 3. Figure 4.27 shows the vertical section of the magnetic tensor field inversion result at y=45 meters and the black outline in this figure indicates the true model. From this figure, we can see that the magnetic body is well recovered from magnetic tensor field inversion. Figure 4.28 and Figure 4.29 show the data fitting for this inversion where the left panel indicates the observed magnetic tensor component and the right panel denotes the predicted data. The final normalized misfit between the observed data and the predicted data is 5%. Figure 4.30 is the convergence plot where the upper panel shows the behavior of normalized misfit and the lower panel indicates how Tikhonov parametric functional and misfit functional decreases with iteration number.

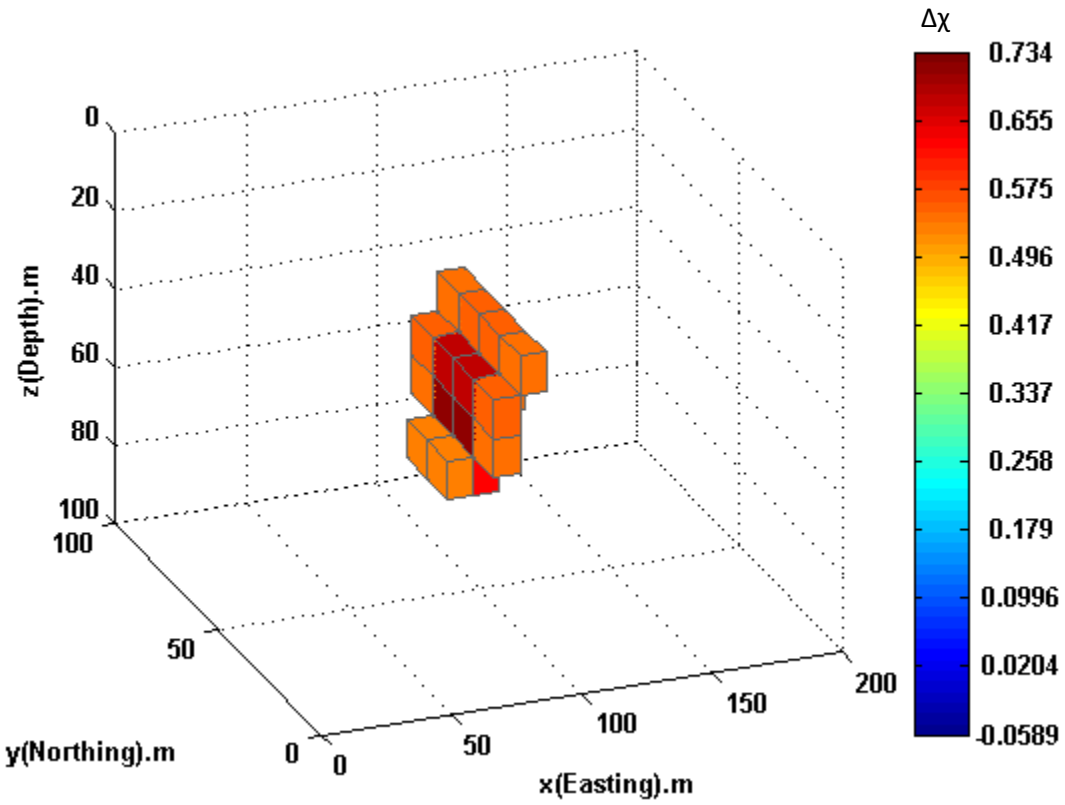

Figure 4.26. 3-D view of inversion result for magnetic tensor inversion, model 3.

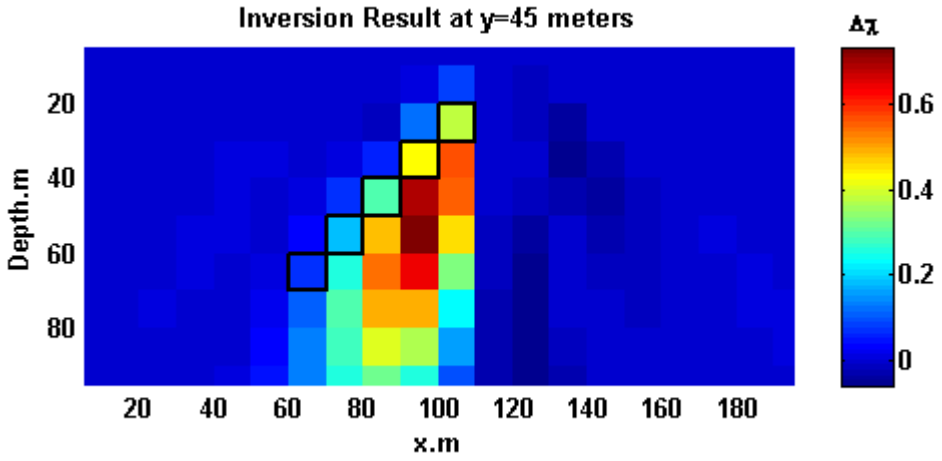

Figure 4.27. Vertical section of inversion result at y=45 meters for magnetic tensor inversion, model 3.

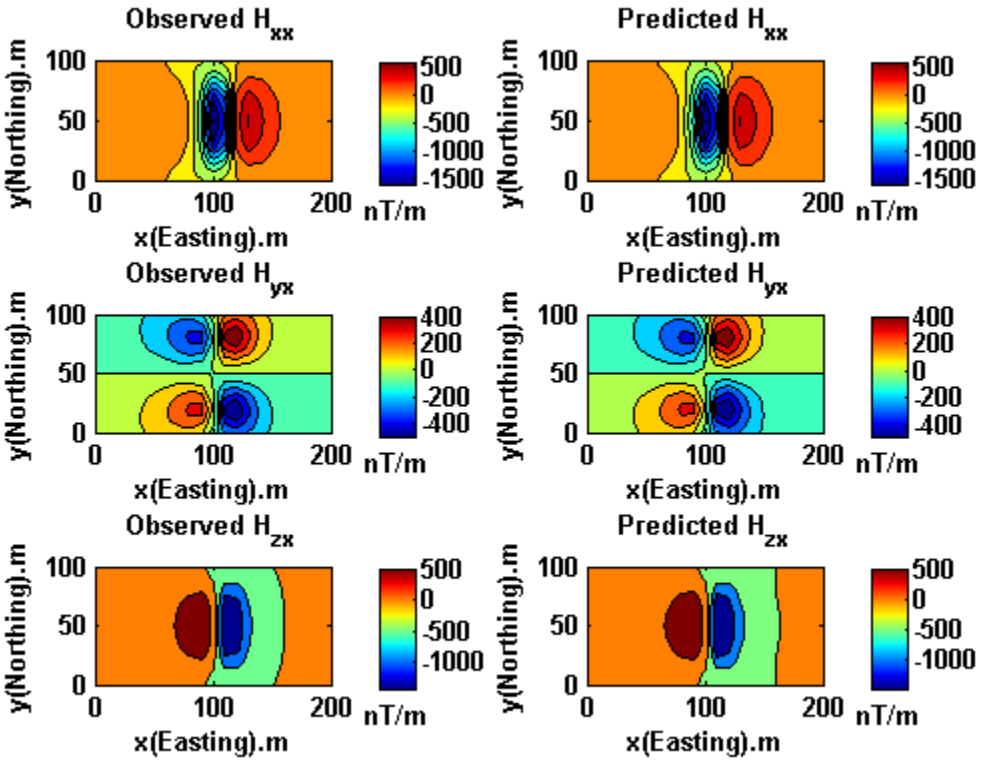

Figure 4.28. Data fitting of magnetic tensor field components for model 3.

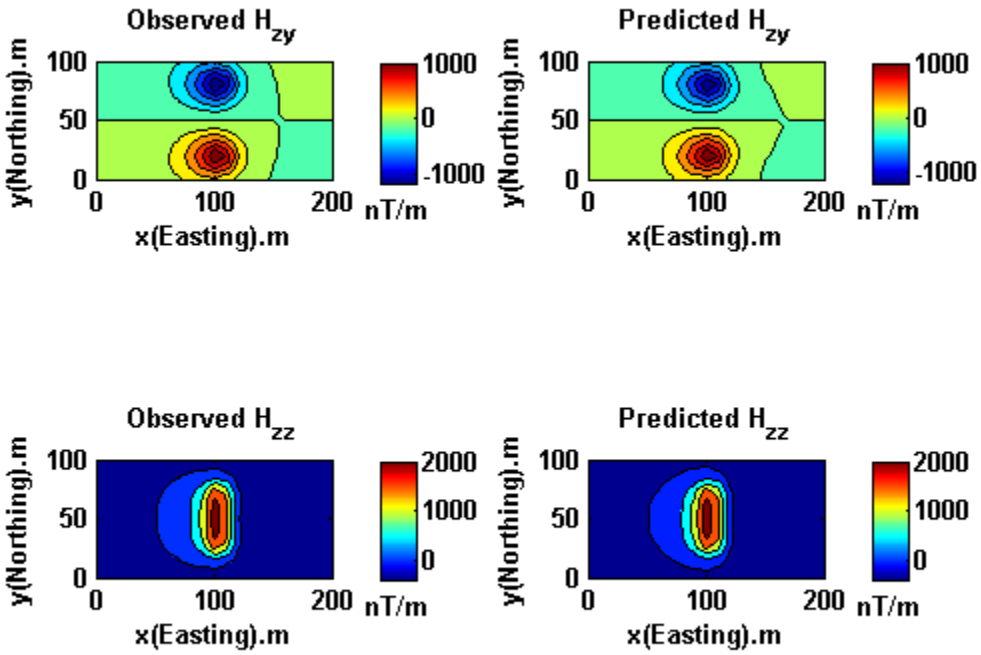

Figure 4.29. Data fitting of magnetic tensor field components for model 3.

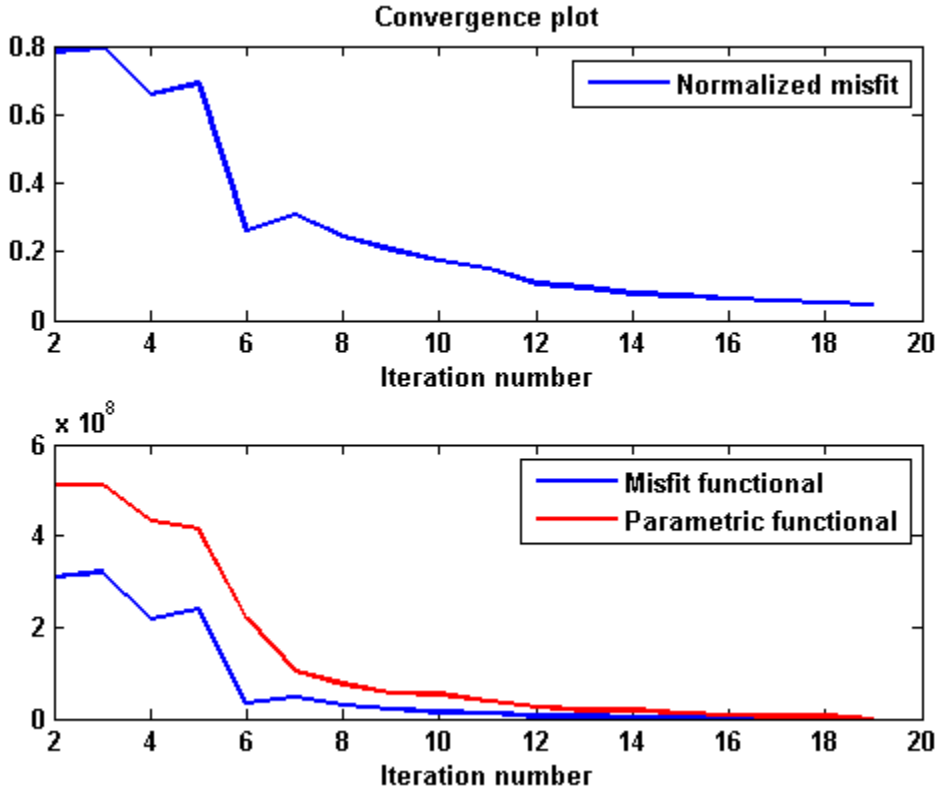

Figure 4.30. Convergence plot for magnetic tensor field inversion, model 3.

4.4.2 Model studies with topography

In this subsection, we will present several model studies for magnetic vector field inversion and magnetic tensor field inversion with topography. In the first part of this subsection, three models will be presented for magnetic vector field inversion. In the second part of this subsection, the same models as for magnetic vector field will be tested for magnetic tensor field inversion.

4.4.2.1 Model studies for magnetic vector field

4.4.2.1.1 Model 1

This is a 3-D model with one anomalous body located below the flat surface. The size of the anomalous body is 10m×60m×10m which extends from 90 m to 100 m in *x* (easting) direction, 20 m to 80 m in *y (northing)* direction and 24 m to 34 m in *z (downward)* direction. The size of the research domain is 200m×100m in *x* and *y* direction respectively and the depth reach 109 meters. The anomalous magnetic susceptibility is 1 in SI units. We consider that inclination of inducing magnetic field is 90 degrees and the declination of the inducing magnetic field is 0. Figure 4.31 is an illustration of this model with blue dots indicating points of observation. The curved surface in Figure 4.32 denotes the topography and the red block under the curved surface is the anomalous magnetic body.

For this model, we simulated all magnetic tensor components. We used five independent components H_{xx}, H_{yx}, H_{zx}, H_{zy} and H_{zz} to do joint inversion. Figure 4.33 shows the 3-D image of the joint inversion result for model 1. Figure 4.34 shows the vertical section of the magnetic tensor field inversion result at y=45 meters and the black

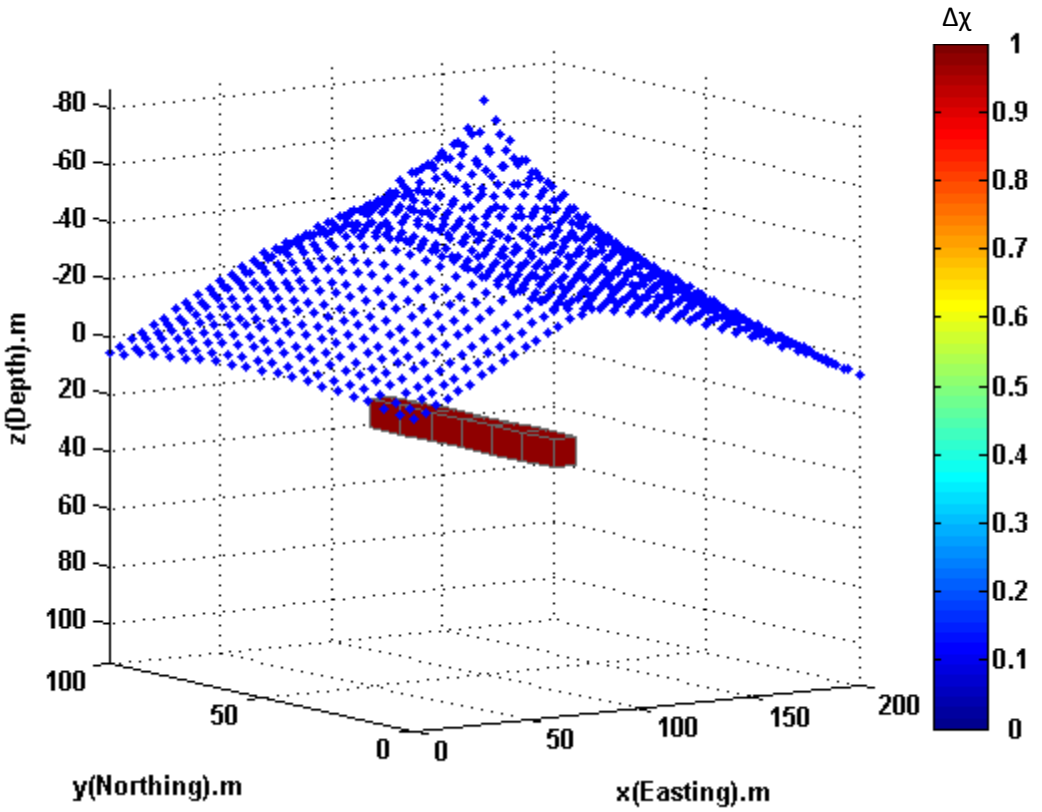

Figure 4.31. This figure shows model 1 with one anomalous magnetic body located below the subsurface. The blue dots in the surface denote the stations for magnetic vector field data measurement.

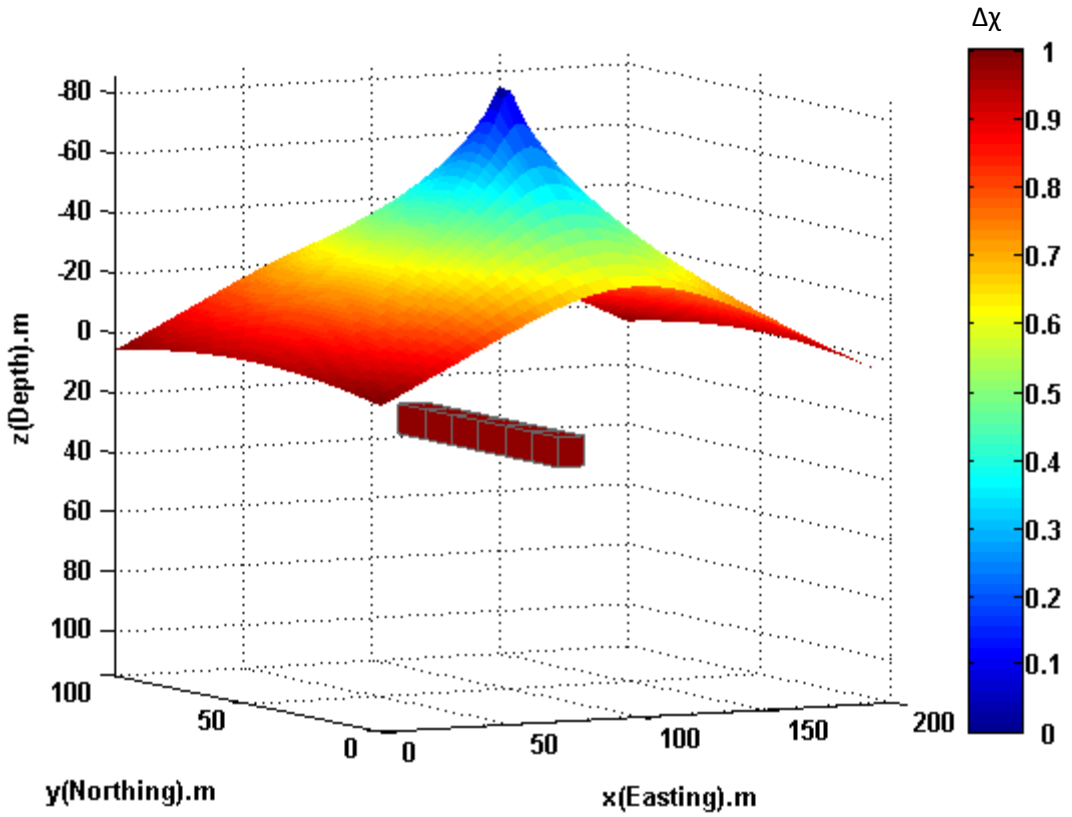

Figure 4.32. The curved surface in this figure indicates the topography with negative value denotes higher elevation and the red block indicates the magnetic body.

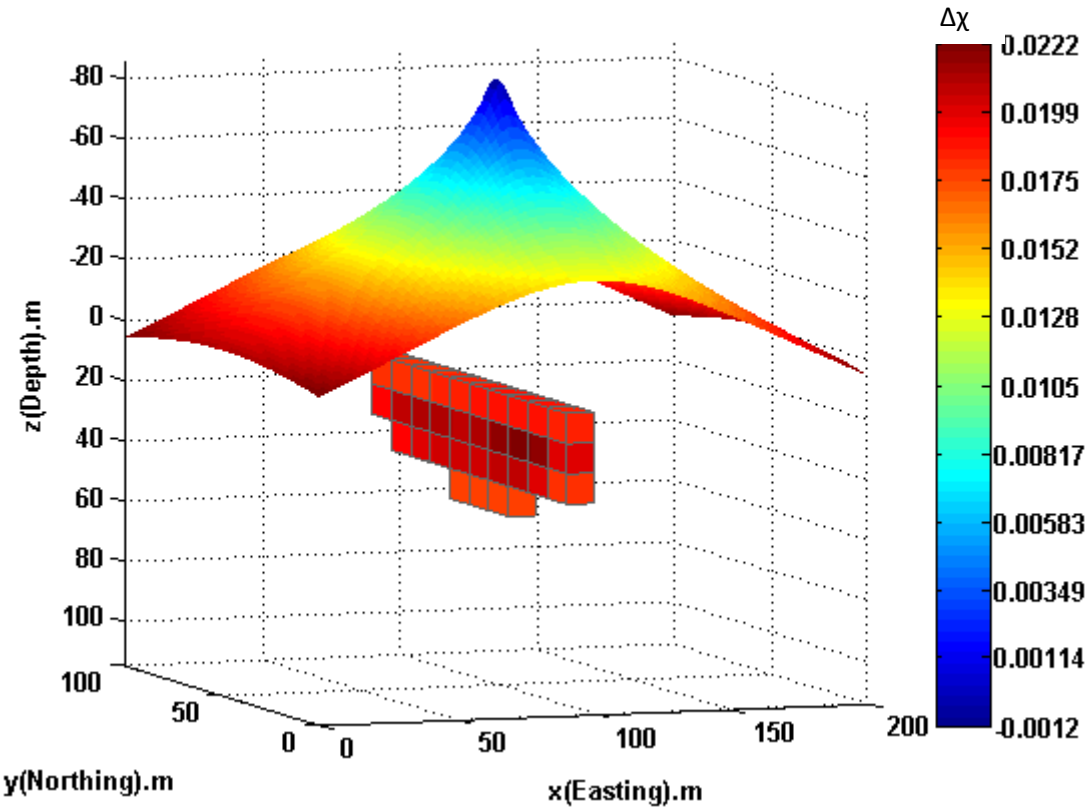

Figure 4.33. 3-D view of inversion result for magnetic vector inversion with topography, model 1.

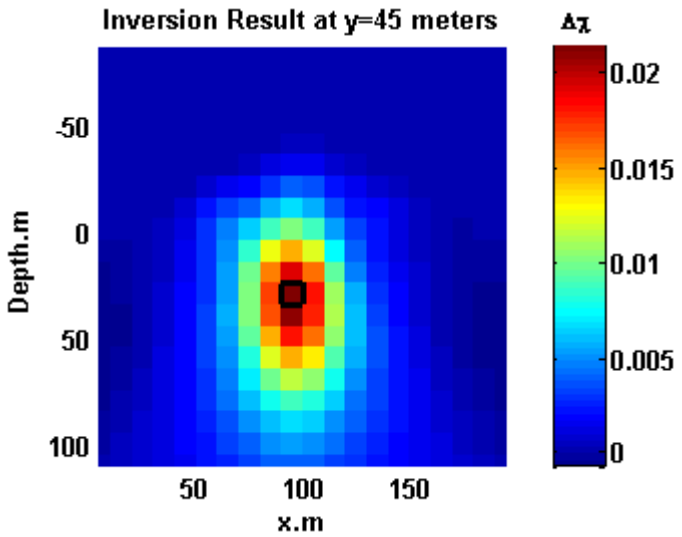

Figure 4.34. Vertical section of inversion result at y=45 meters for magnetic vector inversion with topography, model 1.

outline in this figure indicates the true model. From this figure, we can see that the magnetic body is well recovered from magnetic tensor field inversion. Also one can see that the inversion image is very compact by applying focusing inversion technique. Figure 4.35 shows the data fitting for this inversion where the left panel indicates the observed magnetic tensor component and the right panel denotes the predicted data. The final normalized misfit between the observed data and the predicted data is 3%. Figure 4.36 is the convergence plot where the upper panel shows the behavior of normalized misfit and the lower panel indicates how Tikhonov parametric functional and misfit functional decreases with iteration number.

4.4.2.1.2 Model 2

This is a 3-D model with one anomalous dyke located below the flat surface. The magnetic dyke extends from 60 m to 120 m in *x* (easting) direction, 20 m to 80 m in *y (northing)* direction and -6 m to 54 m in *z (downward)* direction. The size of the research domain is 200m×100m in *x* and *y* direction, respectively, and the depth reach 109 meters. The anomalous magnetic susceptibility is 1 in SI units. We consider that inclination of inducing magnetic field is 90 degrees and the declination of the inducing magnetic field is 0. Figure 4.37 is an illustration of this model with blue dots indicating points of observation. The curved surface in Figure 4.38 denotes the topography and the red block under the curved surface is the anomalous magnetic body.

For this model, we simulated all magnetic tensor components. We used five independent components H_{xx}, H_{yx}, H_{zx}, H_{zy} and H_{zz} to do joint inversion. Figure 4.39 shows the 3-D image of the joint inversion result for model 2. Figure 4.40 shows the vertical section of the magnetic tensor field inversion result at y=45 meters and the black

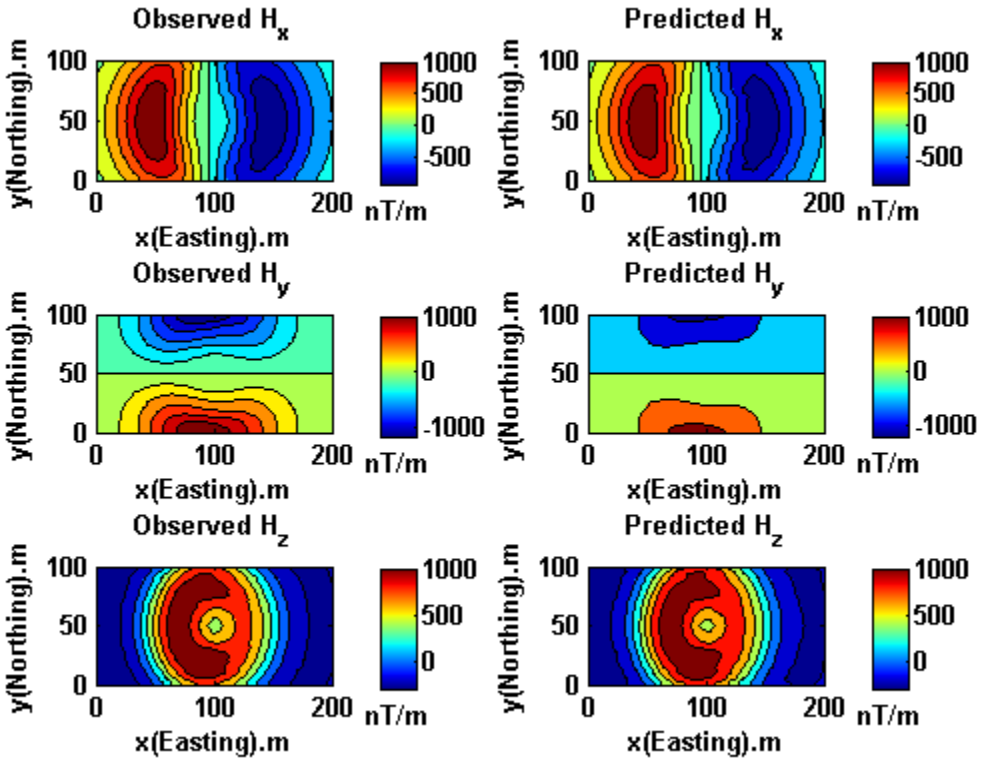

Figure 4.35. Data fitting of magnetic vector field components for model 1.

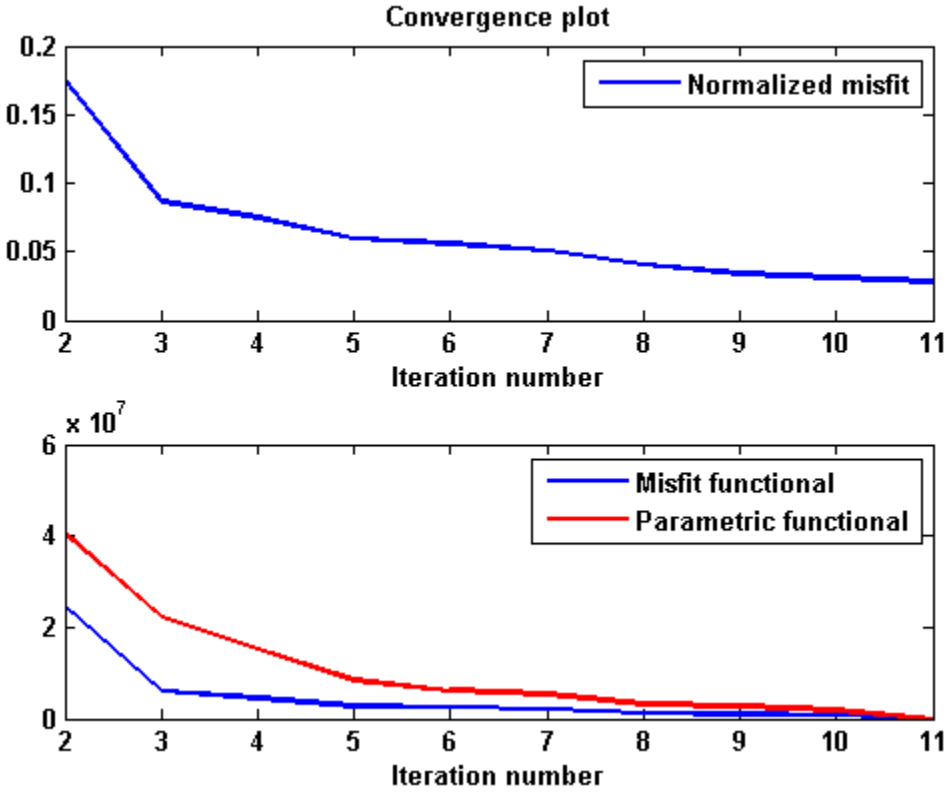

Figure 4.36. Convergence plot for magnetic vector field inversion with topography, model 1.

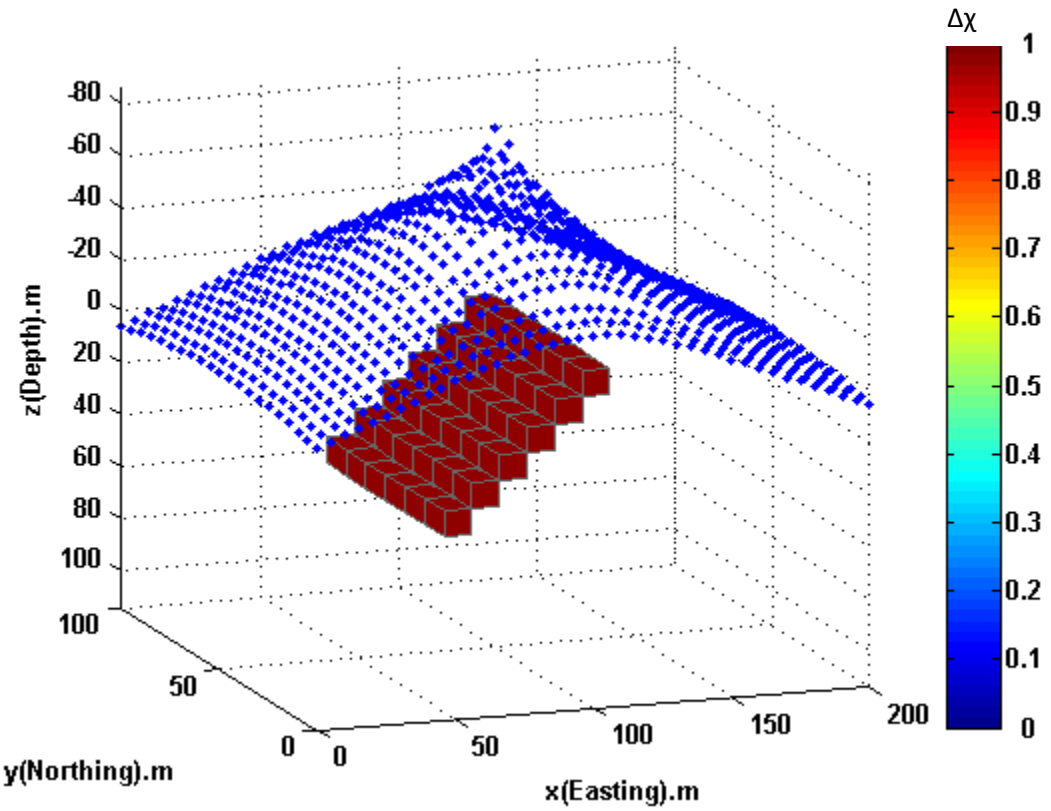

Figure 4.37. This figure shows model 2 with one anomalous magnetic dyke located below the subsurface. The blue dots in the surface denote the stations for magnetic vector field data measurement.

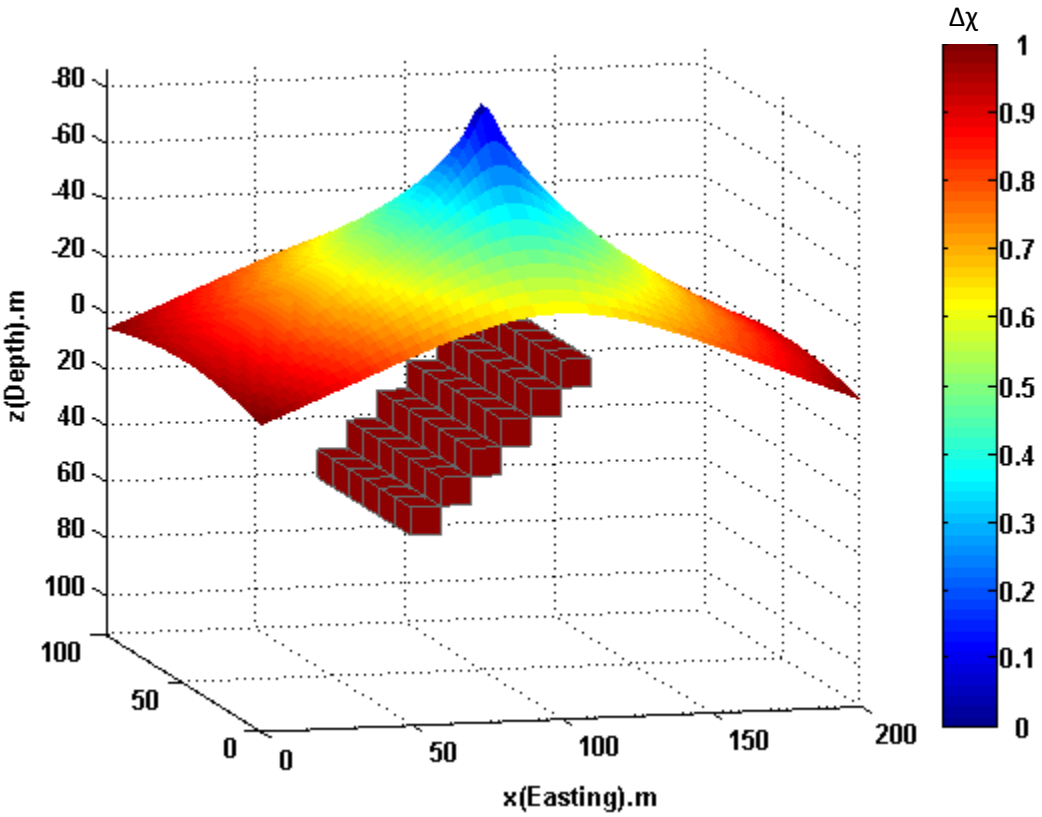

Figure 4.38. The curved surface in this figure indicates the topography with negative value denotes higher elevation and the red block indicates the magnetic body.

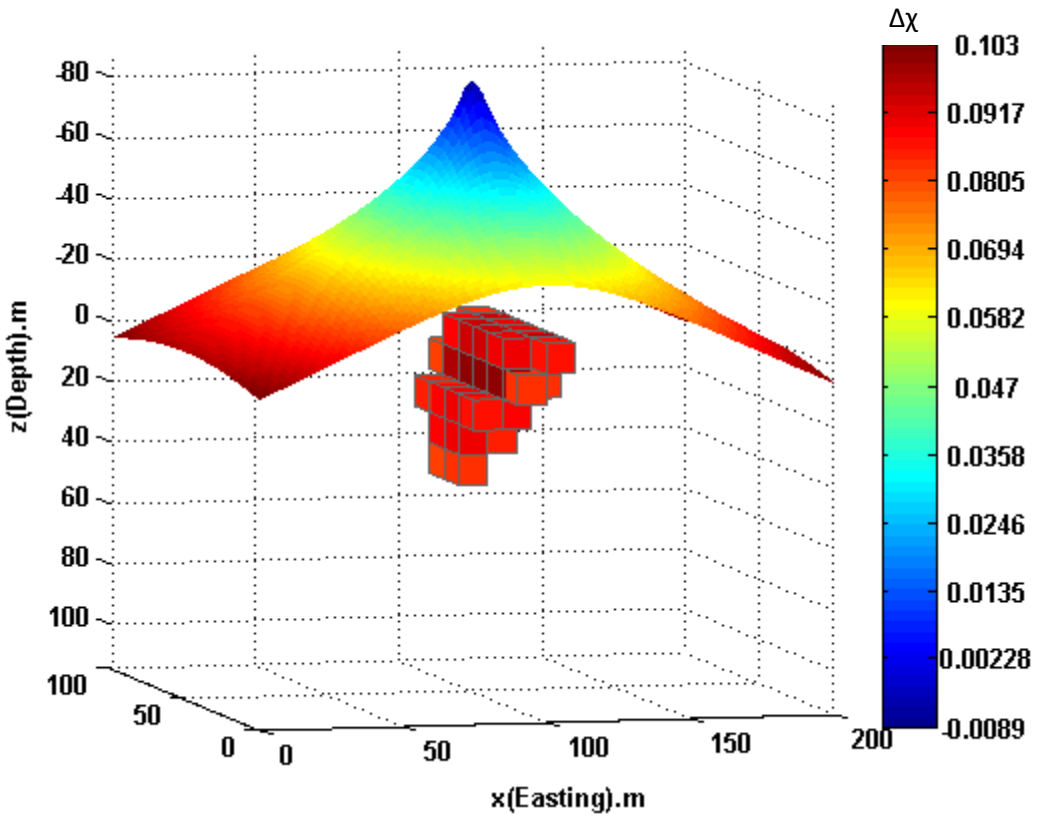

Figure 4.39. 3-D view of inversion result for magnetic vector inversion with topography, model 2.

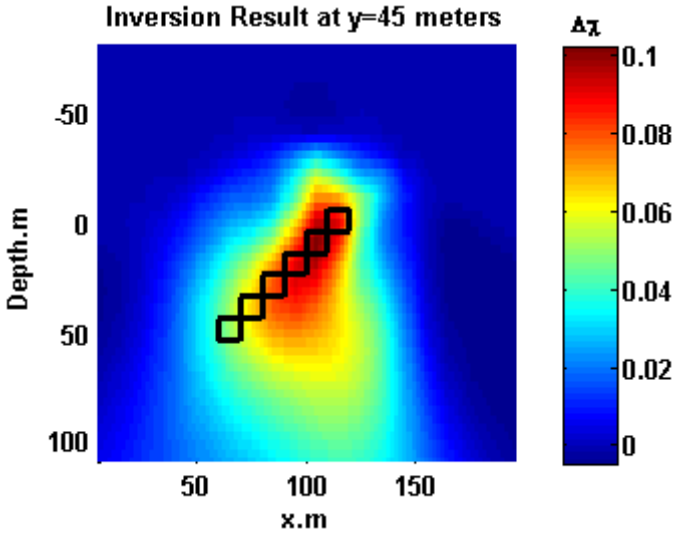

Figure 4.40. Vertical section of inversion result at y=45 meters for magnetic vector inversion with topography, model 2.

outline in this figure indicates the true model. From this figure, we can see that the magnetic body is well recovered from magnetic tensor field inversion. Figure 4.41 shows the data fitting for this inversion where the left panel indicates the observed magnetic tensor component and the right panel denotes the predicted data. The final normalized misfit between the observed data and the predicted data is 3%. Figure 4.42 is the convergence plot where the upper panel shows the behavior of normalized misfit and the lower panel indicates how Tikhonov parametric functional and misfit functional decreases with iteration number.

4.4.2.2 Model studies for magnetic tensor field

4.4.2.2.1 Model 1

This model is exactly the same as model 1 we used in the previous model study for magnetic vector field and the research domain is also the same. Figure 4.31 is an illustration of this model with blue dots indicates points of observation. The curved surface in Figure 4.32 denotes the topography and the red block under the curved surface is the anomalous magnetic body.

For this model, we simulated all magnetic tensor components. We used five independent components H_{xx}, H_{yx}, H_{zx}, H_{zy} and H_{zz} to do joint inversion. Figure 4.43 shows the 3-D image of the joint inversion result for model 1. Figure 4.44 shows the vertical section of the magnetic tensor field inversion result at y=45 meters and the black outline in this figure indicates the true model. From this figure, we can see that the magnetic body is well recovered from magnetic tensor field inversion. Also one can see that the inversion image is very compact by applying the focusing inversion technique. Figure 4.45 and Figure 4.46 show the data fitting for this inversion where the left panel

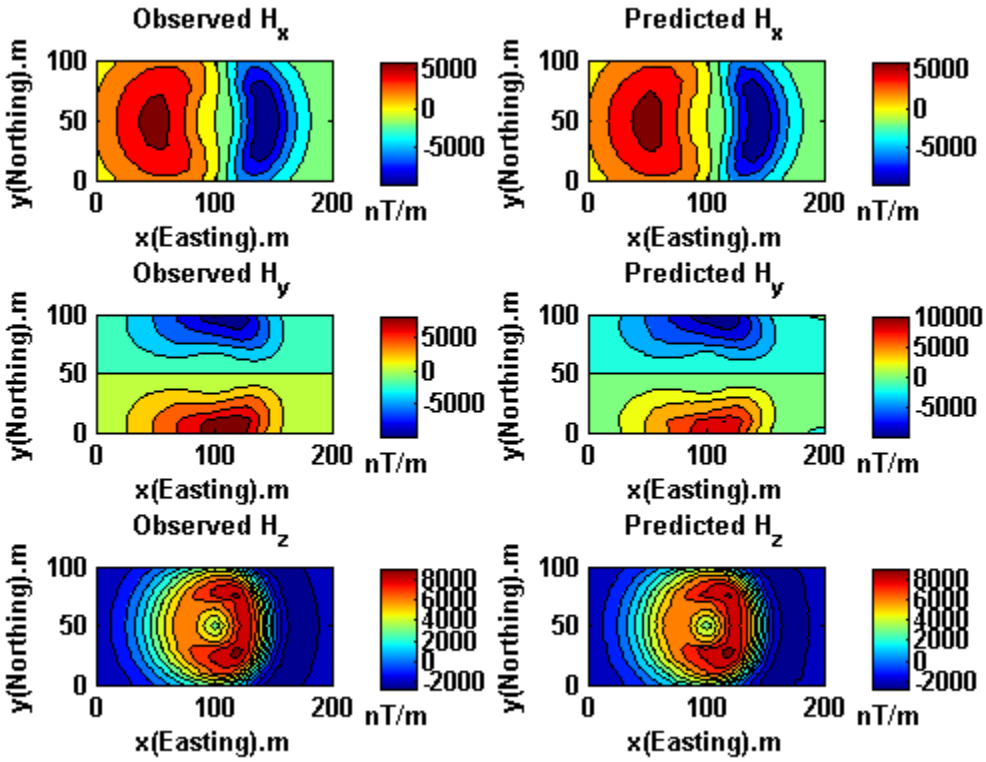

Figure 4.41. Data fitting of magnetic vector field components for model 2.

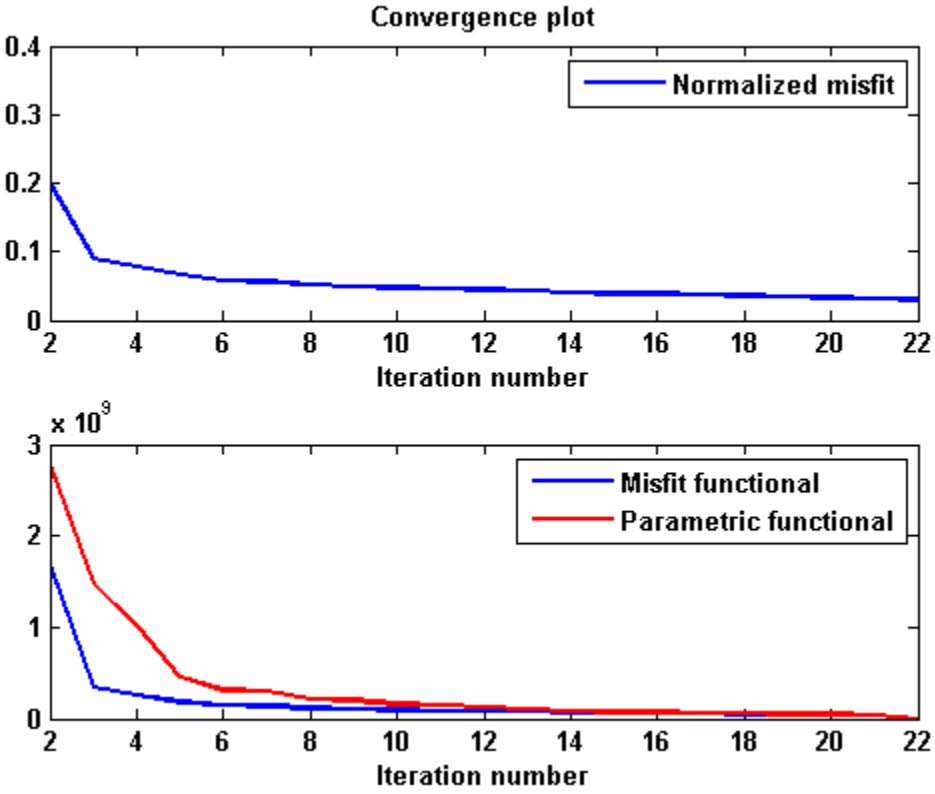

Figure 4.42. Convergence plot for magnetic vector field inversion with topography, model 2.

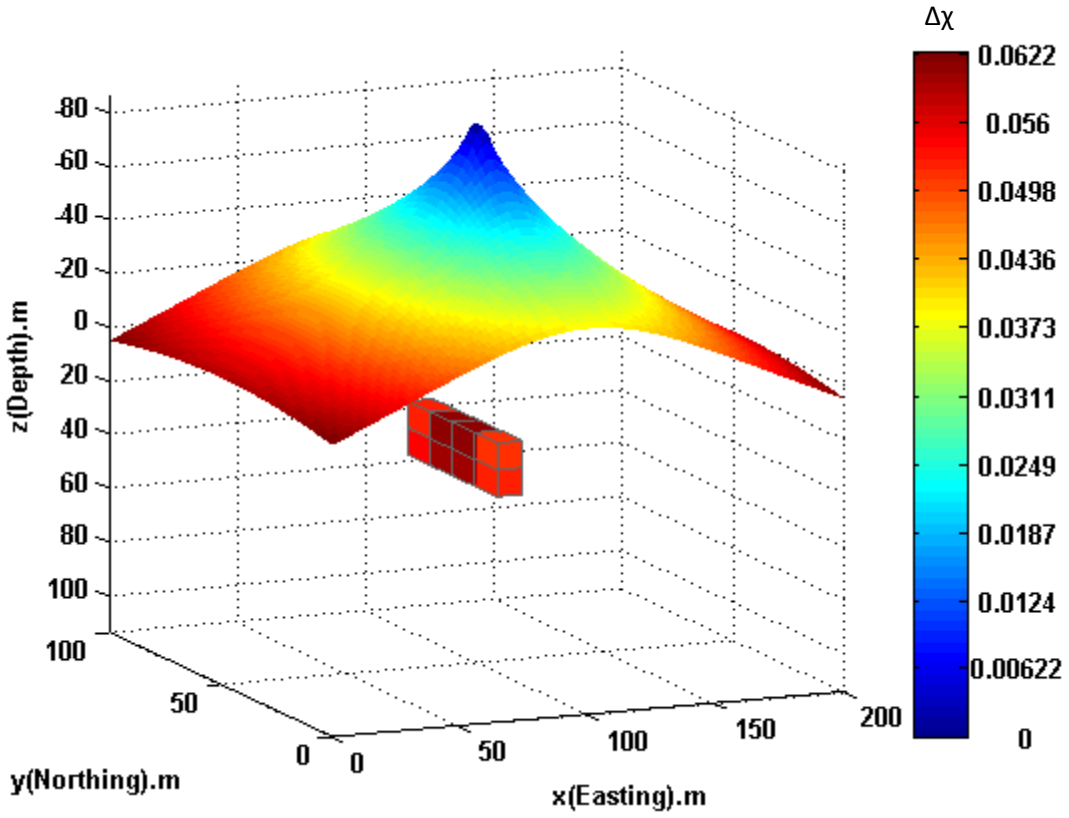

Figure 4.43. 3-D view of inversion result for magnetic tensor inversion with topography, model 1.

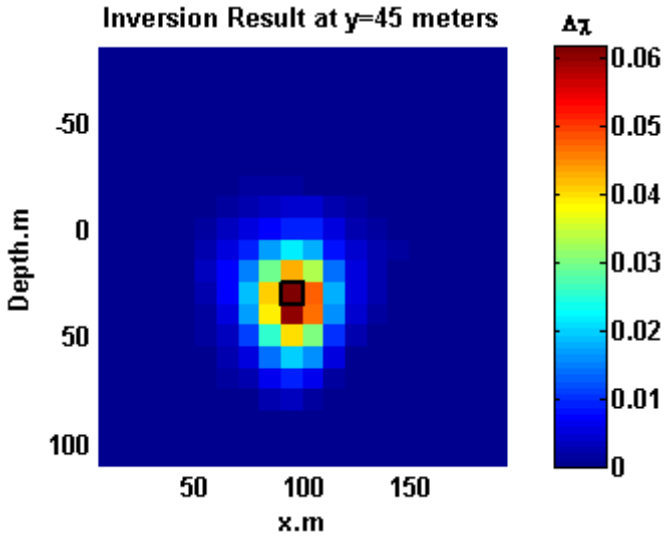

Figure 4.44. Vertical section of inversion result at y=45 meters for magnetic tensor inversion with topography, model 1.

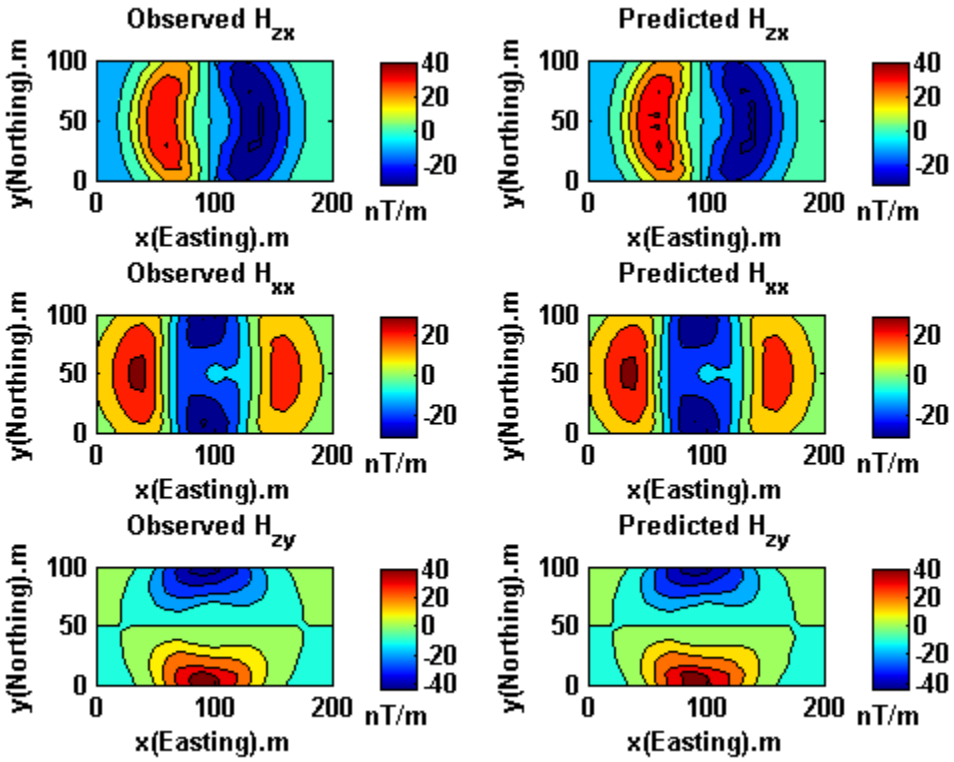

Figure 4.45. Data fitting of magnetic tensor field components for model 1.

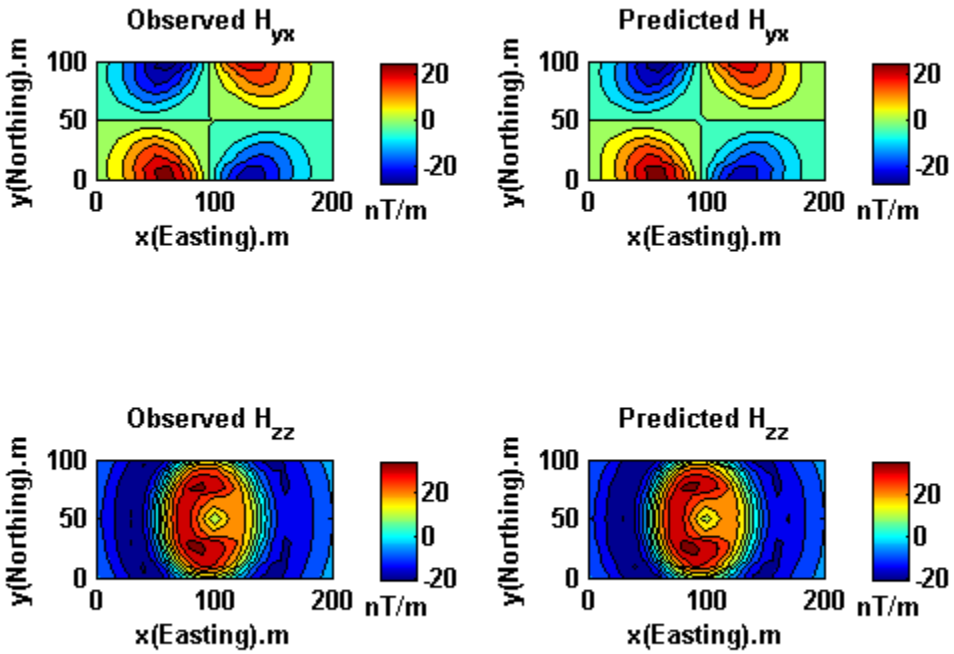

Figure 4.46. Data fitting of magnetic tensor field components for model 1.

indicates the observed magnetic tensor component and the right panel denotes the predicted data. The final normalized misfit between the observed data and the predicted data is 3%. Figure 4.47 is the convergence plot where the upper panel shows the behavior of normalized misfit and the lower panel indicates how Tikhonov parametric functional and misfit functional decreases with iteration number.

4.4.2.2.2 Model 2

This model is exactly the same as model 2 we used in the previous model study for magnetic vector field and the research domain is also the same. Figure 4.37 is an illustration of this model with blue dots indicating points of observation. The curved surface in Figure 4.38 denotes the topography and the red block under the curved surface is the anomalous magnetic body.

For this model, we simulated all magnetic tensor components. We used five independent components H_{xx}, H_{yx}, H_{zx}, H_{zy} and H_{zz} to do joint inversion. Figure 4.48 shows the 3-D image of the joint inversion result for model 1. Figure 4.49 shows the vertical section of the magnetic tensor field inversion result at y=45 meters and the black outline in this figure indicates the true model. From this figure, we can see that the magnetic body is well recovered from magnetic tensor field inversion. Also one can see that the inversion image is very compact by applying focusing inversion technique. Figure 4.50 and Figure 4.51 show the data fitting for this inversion where the left panel indicates the observed magnetic tensor component and the right panel denotes the predicted data. The final normalized misfit between the observed data and the predicted data is 3%. Figure 4.52 is the convergence plot where the upper and lower panels show misfit functional and Tikhonov parametric functional decrease with iteration number.

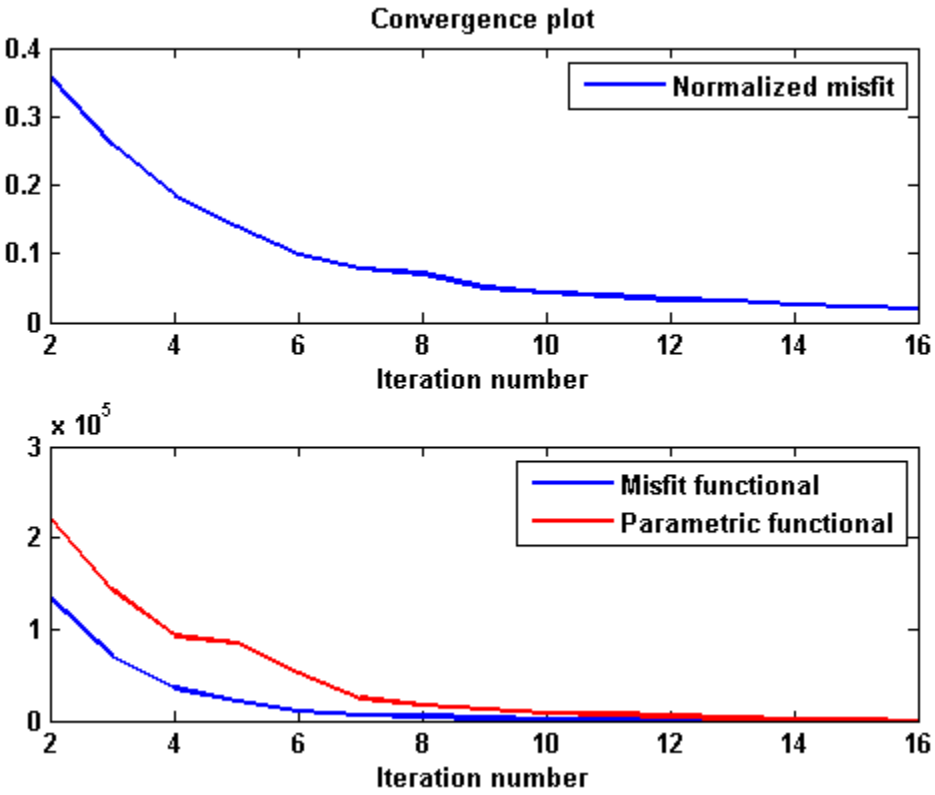

Figure 4.47. Convergence plot for magnetic tensor field inversion with topography, model 1.

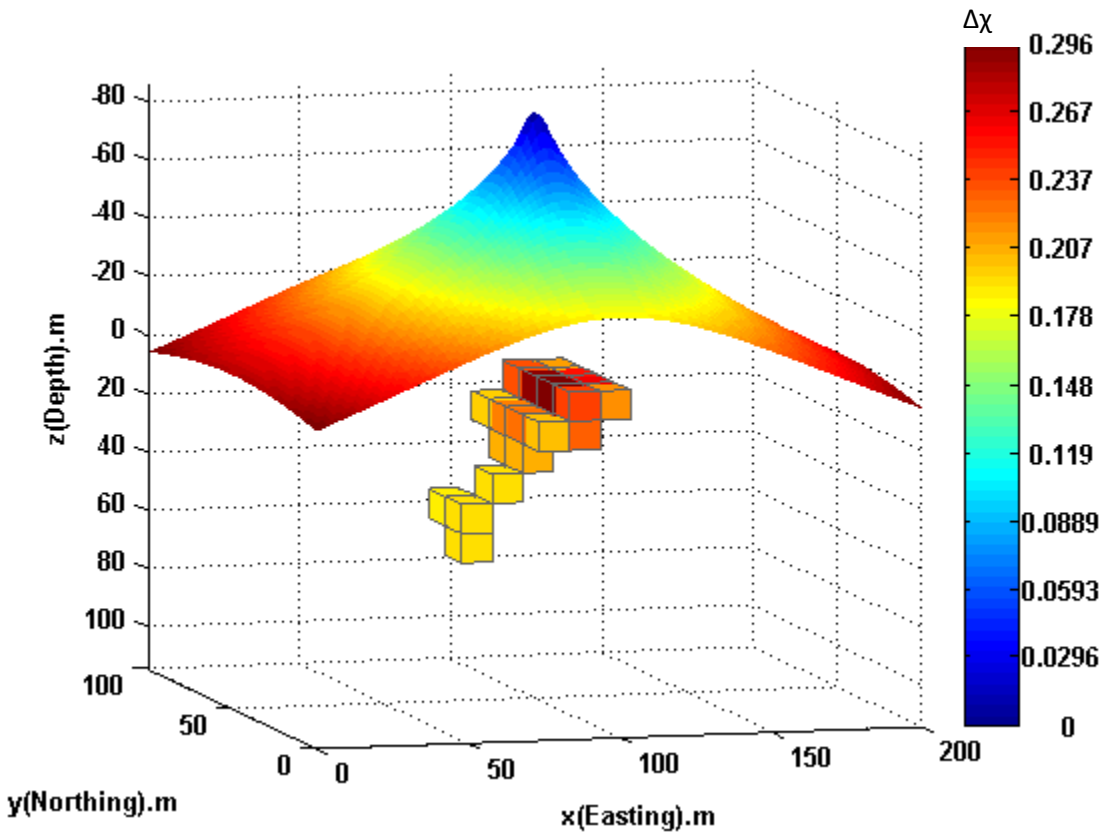

Figure 4.48. 3-D view of inversion result for magnetic tensor inversion with topography, model 2.

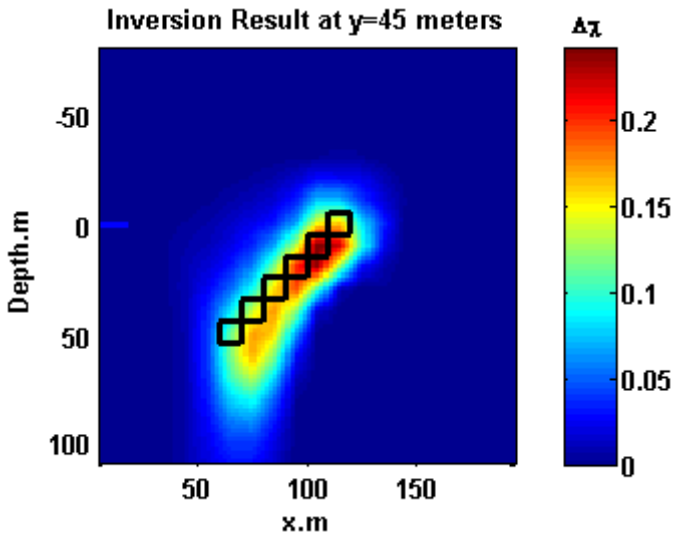

Figure 4.49. Vertical section of inversion result at y=45 meters for magnetic tensor inversion with topography, model 2.

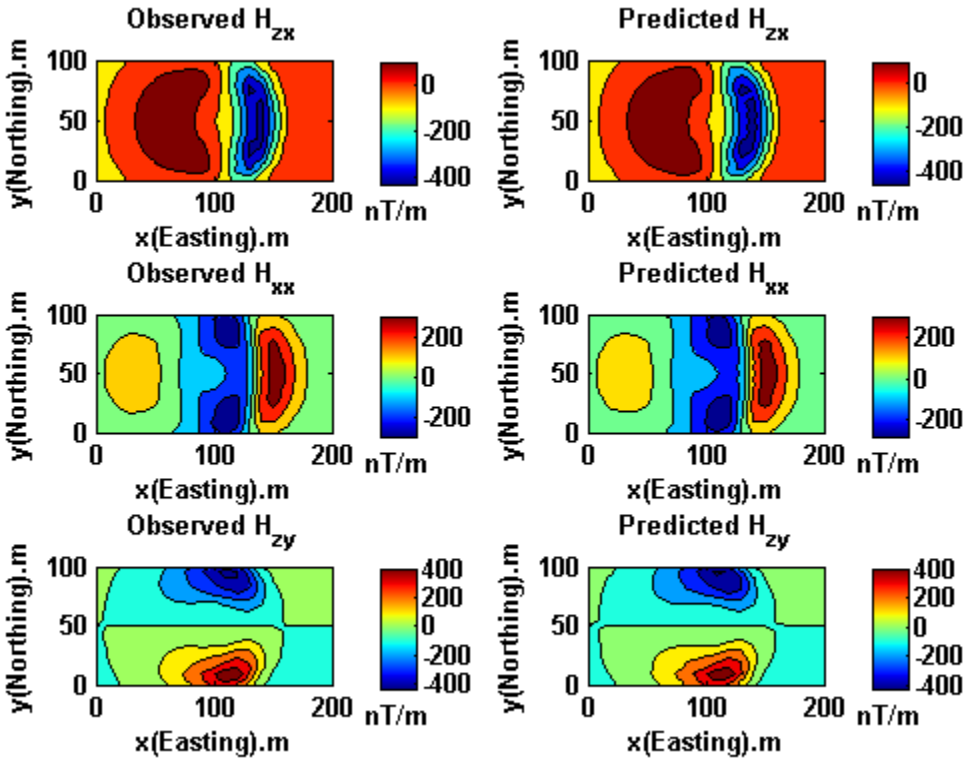

Figure 4.50. Data fitting of magnetic tensor field components for model 2.

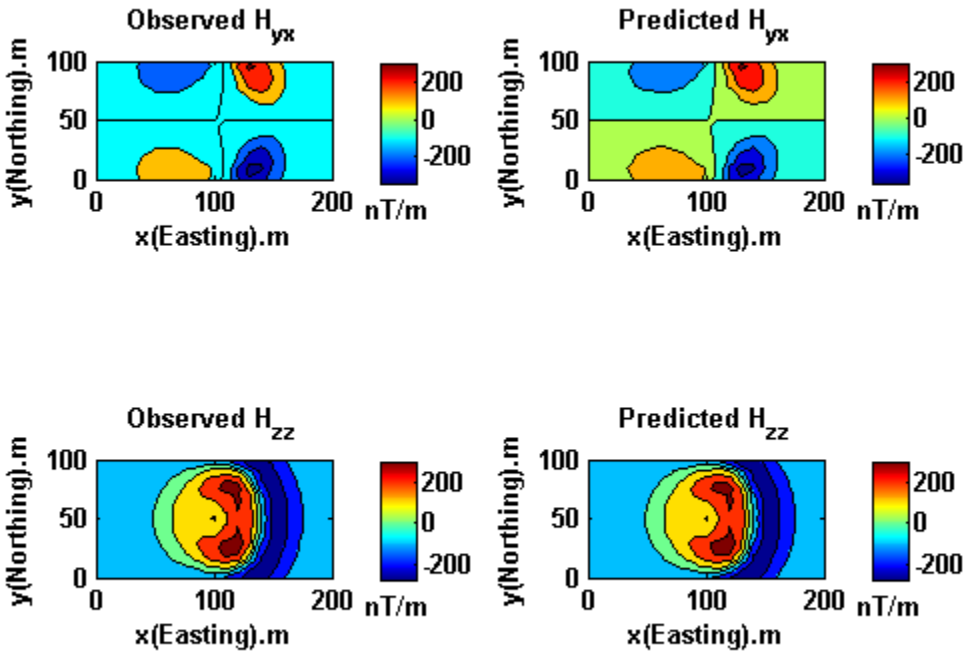

Figure 4.51. Data fitting of magnetic tensor field components for model 2.

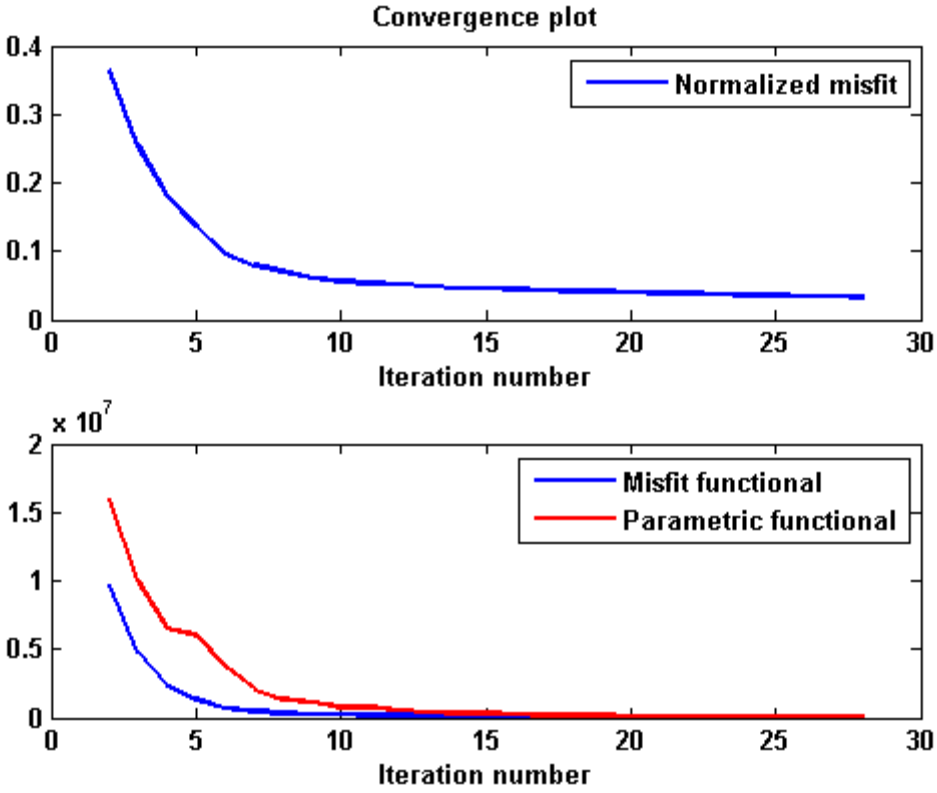

Figure 4.52. Convergence plot for magnetic tensor field inversion with topography, model 2.

4.4.2.3 Magnetic vector field inversion vs. magnetic tensor inversion

Previously, we have tested regularized focusing inversion of the magnetic vector field and magnetic tensor field for the same models. Theoretically, magnetic tensor field has higher sensitivity to anomalous body than magnetic vector field. As a result, the image we get from magnetic tensor field inversion should have higher resolution than we get from magnetic field inversion for the same model.

The left panel of Figure 4.53 shows the vertical sections of the inversion result we get from magnetic vector field inversion for two different models and the right panel shows the vertical section of the inversion result obtained from magnetic tensor field inversion of the same models. One can see from the figure that the anomalous magnetic bodies are well recovered from both magnetic field inversion and magnetic tensor field inversion. However, the images we get from magnetic tensor field inversion are much more compact than images obtained from magnetic field inversion for the same model. As a result, the inversion of all independent magnetic tensor components makes magnetic methods an effective way to do geophysical exploration.

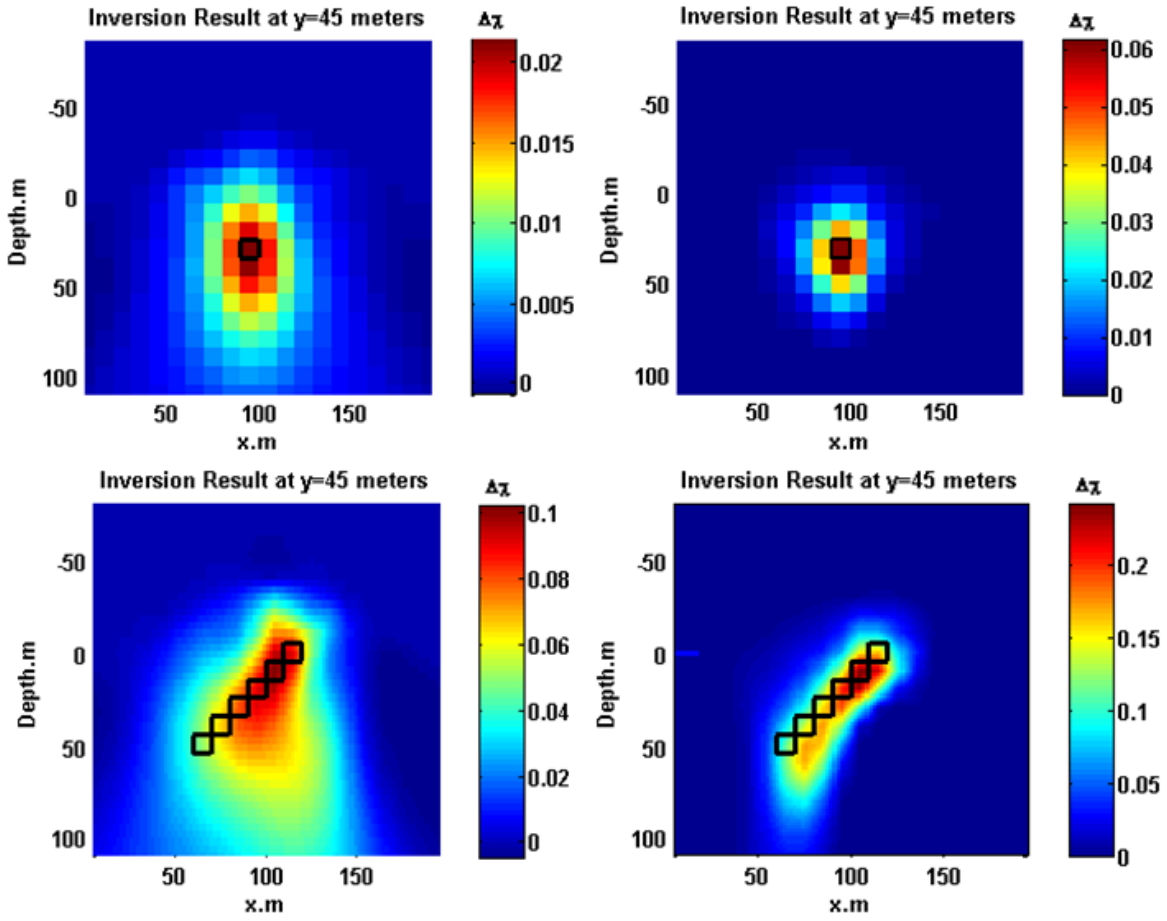

Figure 4.53. Comparison between magnetic vector inversion and magnetic tensor field inversion.

CHAPTER 5

CASE STUDIES

5.1 GETMAG system for measurement of magnetic tensor

The most appropriate sensors for measuring magnetic tensors are superconducting quantum interference devices (SQUIDs), which detect minute changes of flux threading a superconducting loop. They are therefore variometers rather than magnetometers, but they are vector sensors since only changes perpendicular to the loop are detected (Foley and Leslie, 1998; Foley et al., 1999; Lee et al., 2001). High-temperature superconducting (HTS) SQUIDs operate at liquid nitrogen temperatures (77K), overcoming operational difficulties related to the handling of liquid helium (4K) as required for low-temperature superconducting (LTS) SQUIDs.

Based on Tilbrook (2004), CSIRO's GETMAG magnetic gradiometer (Schmidt et al., 2004) is an integrated package of three rotating single-axial gradiometer sensors in an umbrella arrangement, as shown in Figure 5.1. This configuration has several distinct advantages. First, it reduces the required number of sensors and electronics. Second, the amount of cross-talk between sensors is reduced by employing different rotation frequencies. This shifts the measurement (rotation) frequency from quasi-DC to tens or hundreds of hertz, leading to a reduced intrinsic sensor noise and a reduced influence of

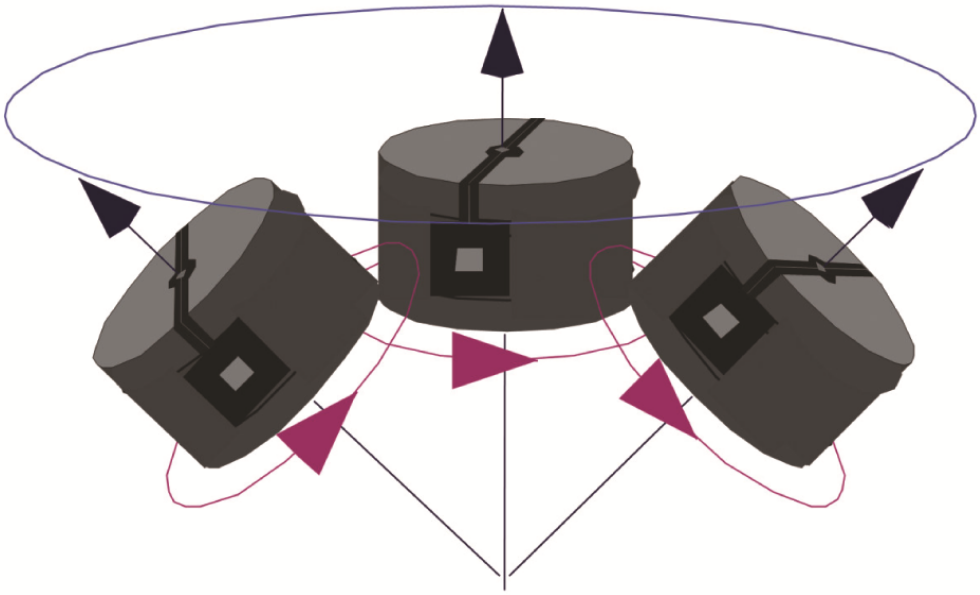

Figure 5.1. Schematic of CSIRO's GETMAG sensor configuration with the three rotating SQUID sensors in an umbrella configuration (from Schmidt et al., 2004)

low-frequency mechanical vibrations; thus the requirements for a suspension system for airborne deployment are significantly reduced. Thirdly, by implementing data extraction through Fourier analysis, magnetic vectors can be separated from magnetic tensors as the signals are centered at the fundamental and at twice the rotation frequency, respectively. Thus, with only three single-axial sensors, all vector and tensor components can be recovered.

5.2 Geological settings of Tallawang magnetite skarn

Schmidt et al. (2004) demonstrated CSIRO's GETMAG system with a field trial of three profiles (50 mN, 60 mN, and 120 mN) over a magnetite skarn deposit at Tallawang, near Gulgong in New South Wales, Australia (Figure 5.2).The deposit is roughly tabular, striking NNW and dipping steeply to the west. The survey was approximately perpendicular to strike, minimizing aliasing and effectively making the surveys 2-D. Figure 5.3 shows the geology of the Tallawang magnetite skarn where the upper panel is a plane view and the lower panel is the vertical section. In the lower panel of the geology, the slant lines indicate drilled borehole and the black area along the line denotes the percent of magnetite skarn where larger black area indicates higher percent of magnetite in the deposit.

The Tallawang magnetite skarn is located along the western margin of the Gulgong Granite, which was intruded during the Kanimblan Orogeny in the Late Carboniferous. In detail, the magnetite occurs in lenses thought to reflect replacement of a tightly folded host rock sequence (Tucklan Beds), and is additionally complicated by

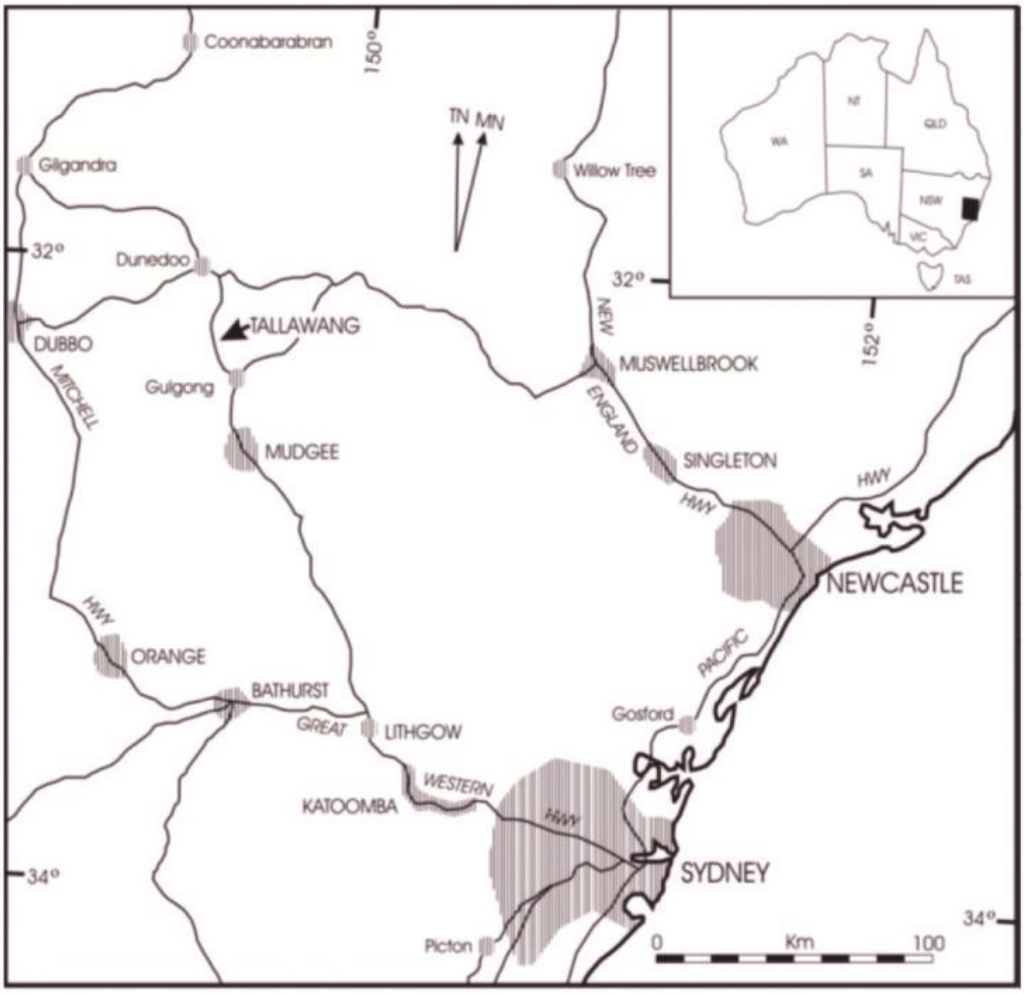

Figure 5.2. Location of the Tallawang magnetite skarn in New South Wales, Australia.

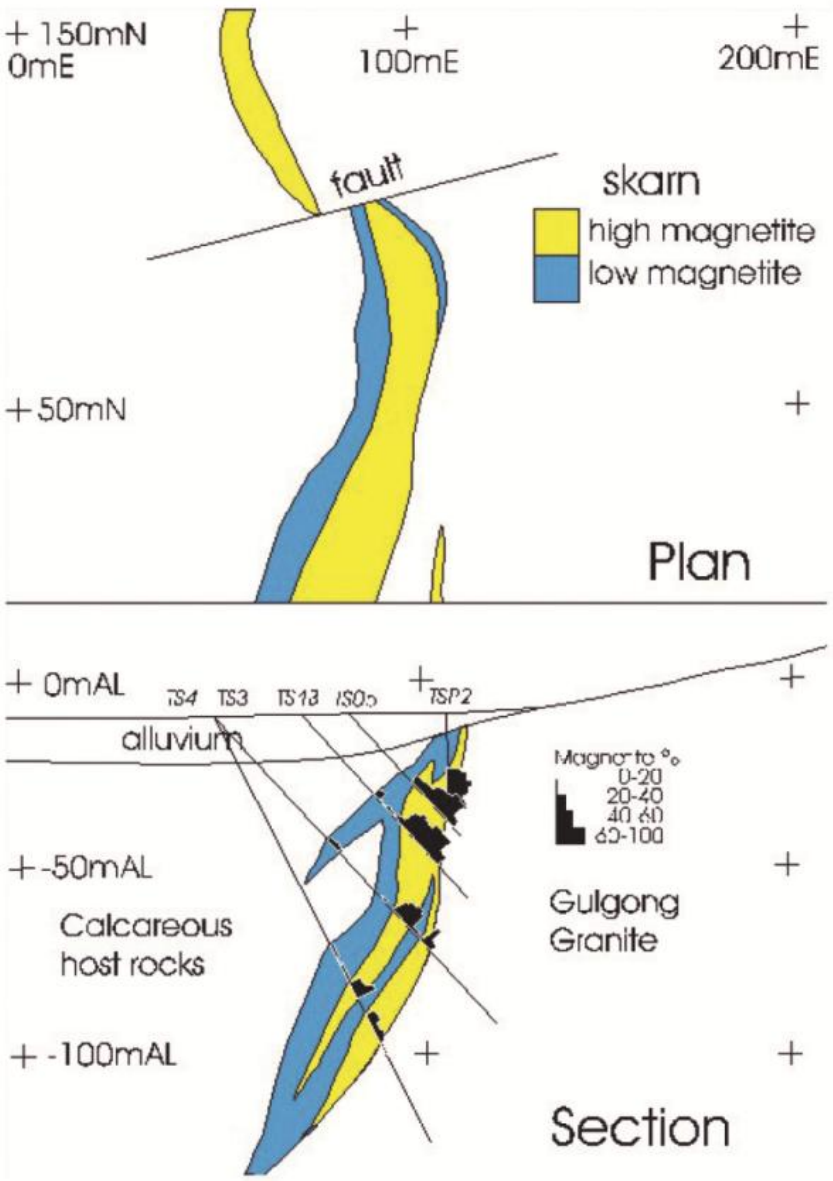

Figure 5.3. Geology of the Tallawang magnetite skarn (from Schmidt et al., 2004).

transverse faulting, causing east-west displacement of the magnetite zones. The magnetite body is well delineated by numerous drill holes, and the rock magnetic properties of the magnetite have been well characterized. The strongest samples possessed susceptibility of 3.8 SI (0.3 cgs) and remanence of 40 Am^{-1}, yielding Koenigsberger ratios (Qs) between 0.2 and 0.5. The mean direction of the remanence is WNW and steeply up. This direction may be the result of a dominant viscous remanent magnetization (VRM) in the direction of the recent geomagnetic field, and a reversed mid-Carboniferous component, dating from the time that the Gulgong Granite was intruded. The effective magnetization, projected onto a vertical plane perpendicular to strike, is directed steeply upward.

For the magnetite tensor data collected along three profiles in Tallawang magnetite skarn, we did both 2-D migration and 3-D regularized inversion for interpretation which will be shown in the subsequent sections.

5.3 Migration of Tallawang magnetic tensor data

For the magnetic tensor data collected over Tallawang magnetite skarn, we did 2-D migration for each profile and got the magnetic susceptibility distributions. The theory for 2-D magnetic tensor field migration with regard to magnetic susceptibility has been presented in Chapter 3.

Figure 5.4, Figure 5.5 and Figure 5.6 show the observed magnetic tensor data along each profile in the upper panel and the corresponding migration results in the lower panel.

We also overlapped the vertical section of the known geology with the migration image for the profile which locates 50 mN which is shown in Figure 5.7. The magnetite

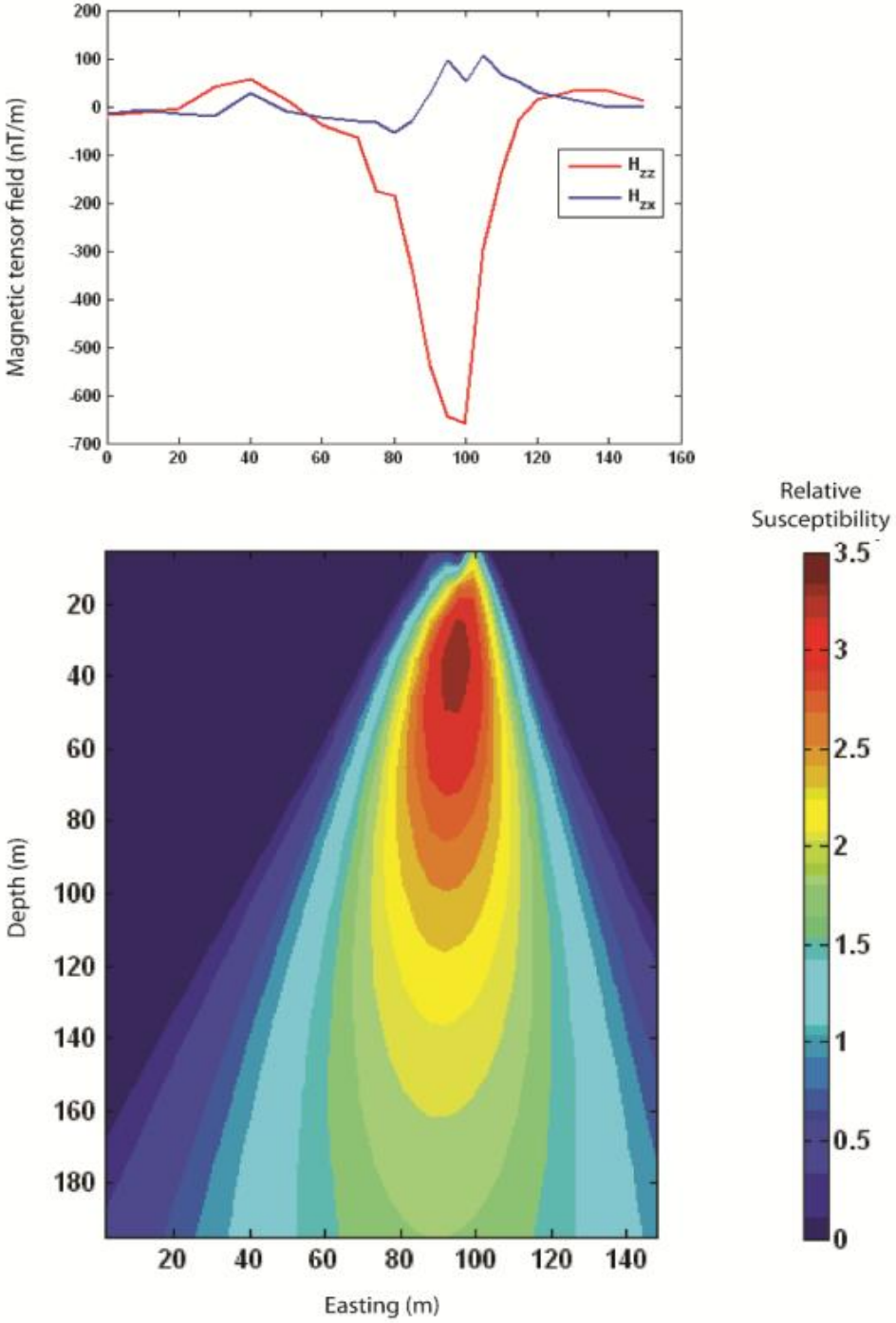

Figure 5.4. Magnetic tensor migration for GETMAG components H_{zx} and H_{zz} measured on line 50 mN over the Tallawang magnetite skarn.

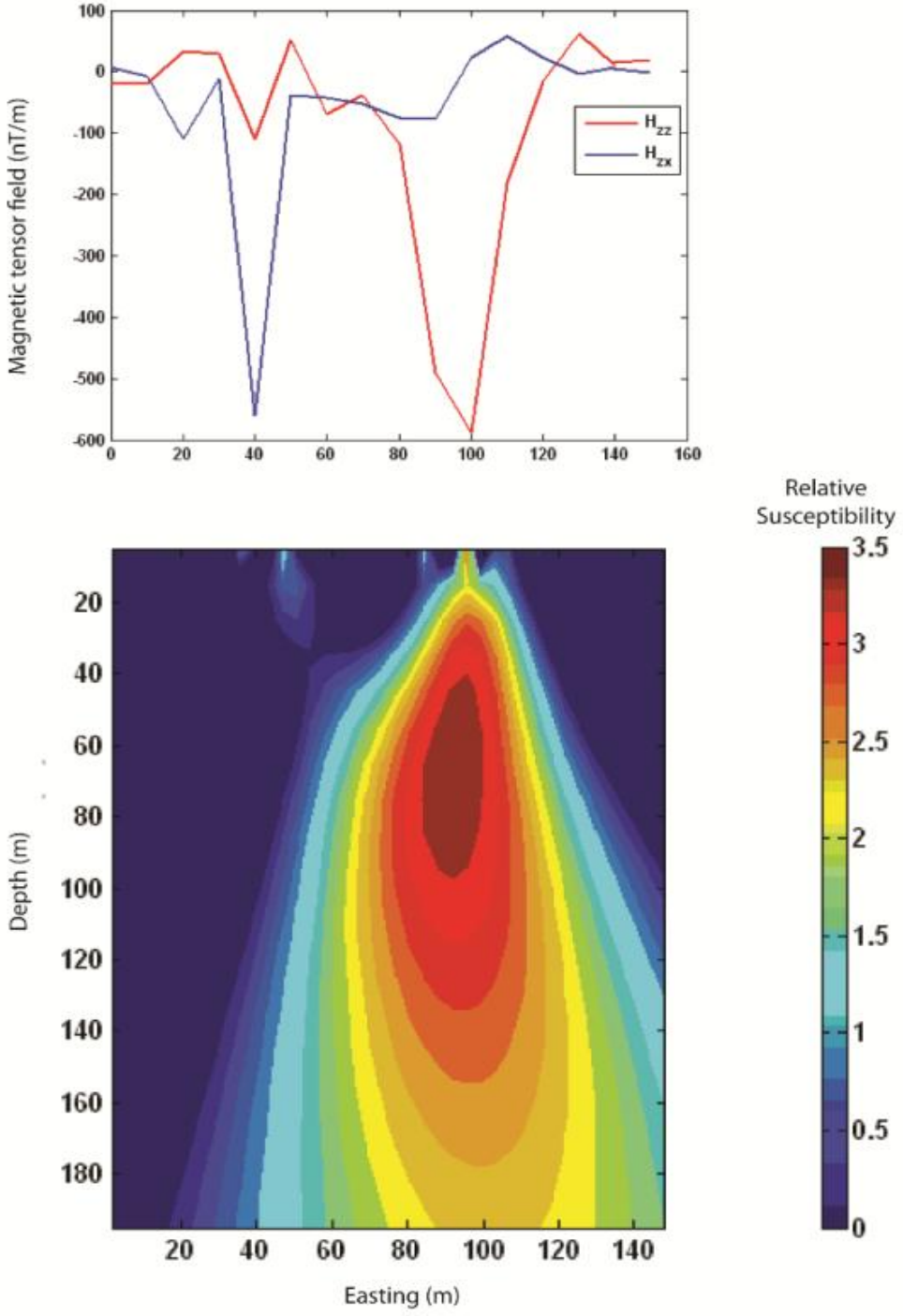

Figure 5.5. Magnetic tensor migration for GETMAG components H_{zx} and H_{zz} measured on line 50 mN over the Tallawang magnetite skarn.

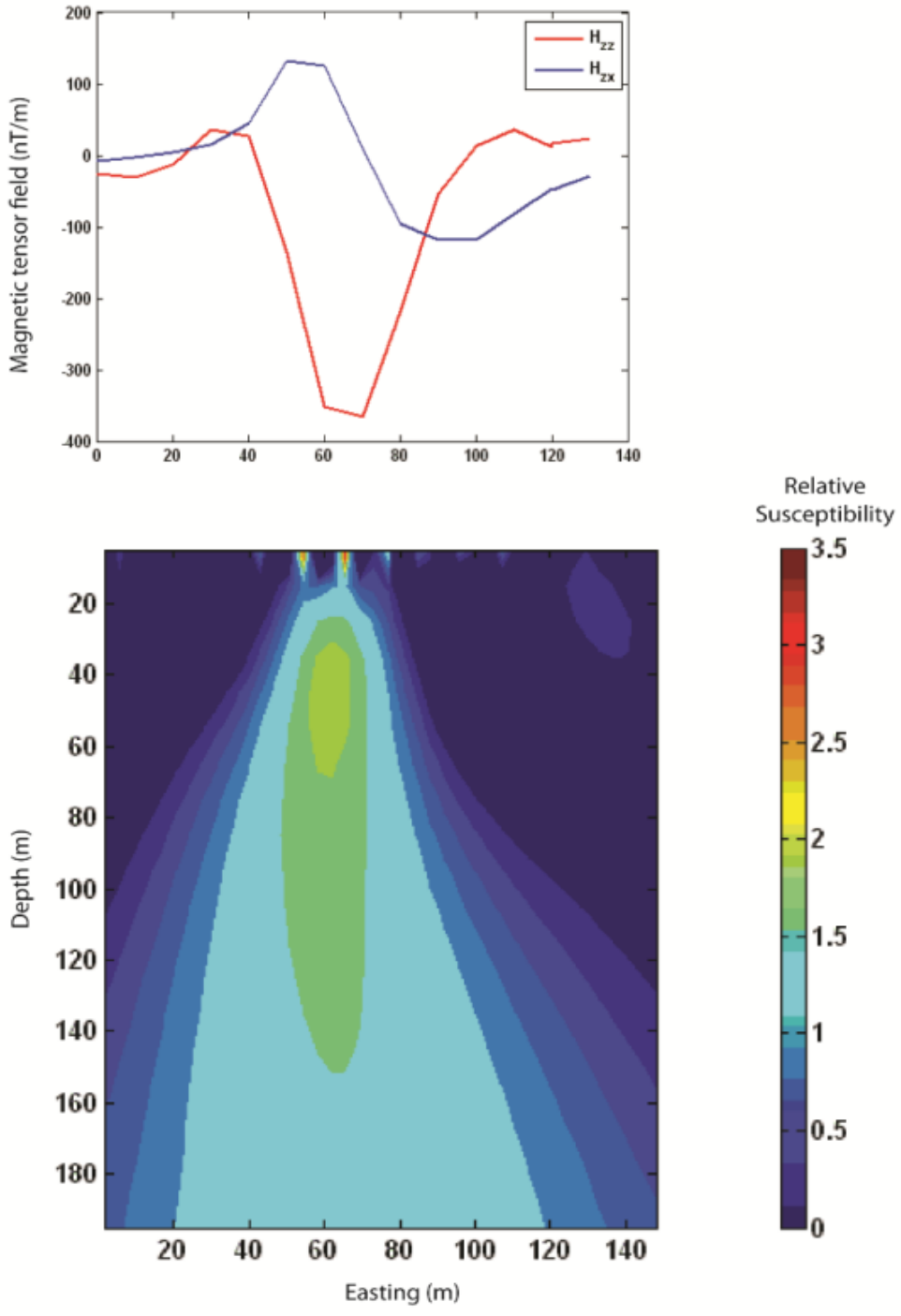

Figure 5.6. Magnetic tensor migration for GETMAG components H_{zx} and H_{zz} measured on line 50 mN over the Tallawang magnetite skarn.

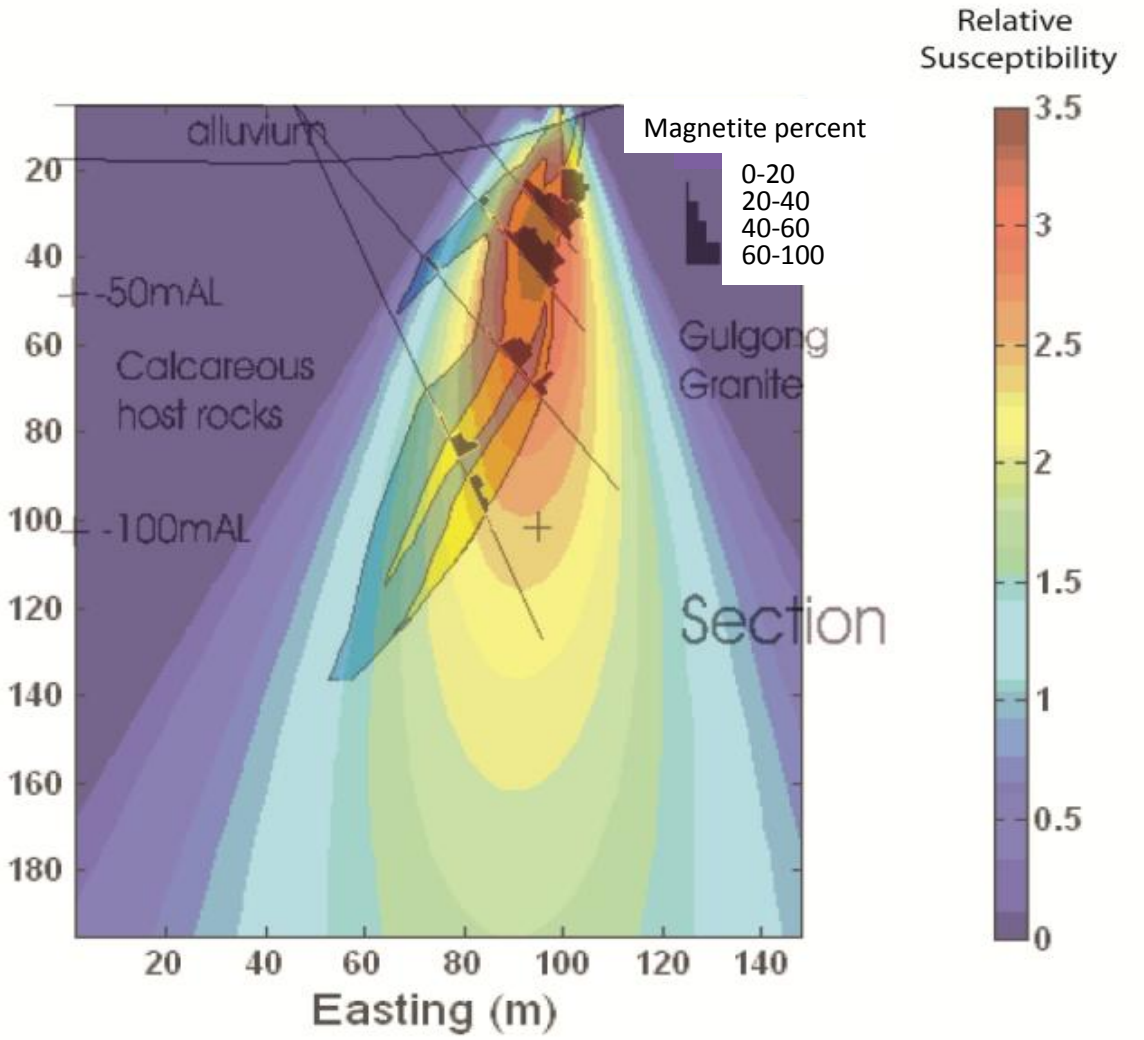

Figure 5.7. Inferred geology of the Tallawang magnetite skarn superimposed on the magnetic tensor migration image for GEGMAG components *Hzx* and *Hzz* measured on line 50 mN.

skarn deposit is recovered as a dike-like body whose top is about 10 m deep, with a maximum susceptibility at approximately 30 m depth, most probably fresh, unweathered magnetite with significant magnetization in contrast to the mantle of the weathered skarn. These results are in very good agreement with those obtained from Euler deconvolution (Schmidt et al., 2004) and the known geology. We note that our migration result is inherently 2-D, meaning that a local strike could not be recovered; thus the fault between profiles 60 mN and 120 mN is not indentified.

5.4 3-D regularized inversion of Tallawang magnetic tensor data

We have applied both 3-D regularized smooth inversion (using minimum norm stabilizer) and 3-D regularized focusing inversion (with minimum support stabilizer) to the three profiles of the GETMAG data to obtain 3-D susceptibility images. The theory of 3-D regularized inversion is discussed in Chapter 4. The data collected in this area are quite noisy especially for some magnetic components. As a result, we used four independent magnetic tensor components H_{yx}, H_{yy}, H_{yz} and H_{zz} to do joint inversion. Both focusing inversion and smooth inversion terminated at a common misfit of 25%.

The surface of the Tallawang deposit area is pretty flat. As a result, we will not consider topography in our inversion. The magnetization of the magnetite skarn is dominated by inducing magnetization. We will not consider remanent magnetization into inversion. In the inversion process, we enforced positive value of magnetic susceptibility in order to get a physically meaningful result. Figure 5.8 and Figure 5.9 show the observed and predicted data for focusing and smooth inversions, respectively.

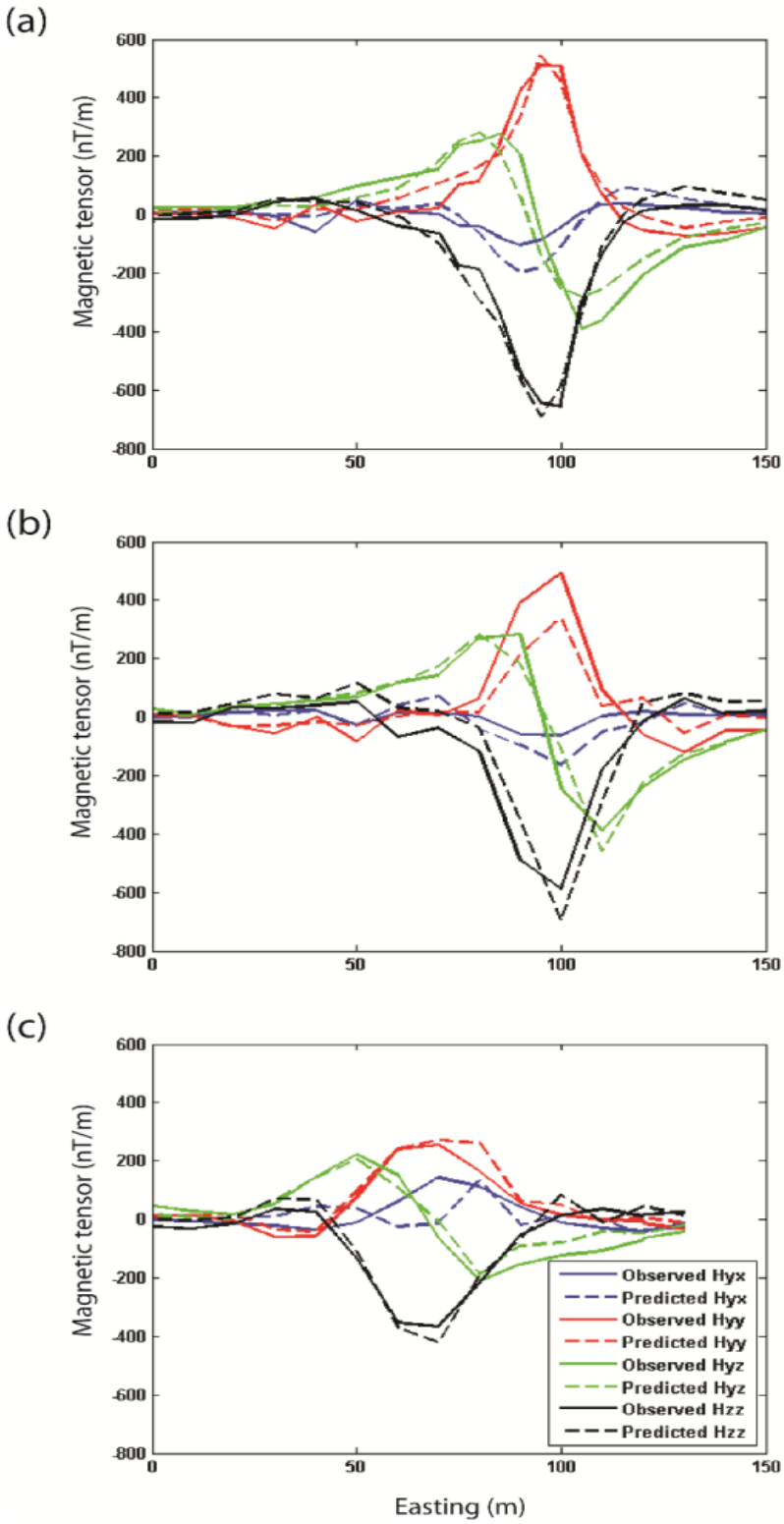

Figure 5.8. Observed (solid lines) and predicted (dashed lines) data for different magnetic tensor components along profiles (a) 50 mN, (b) 60 mN, and (c) 120 mN. The predicted mdata are those obtained from 3-D inversion with minimum support (focusing) regularization. The misfit between observed and predicted data is 25%.

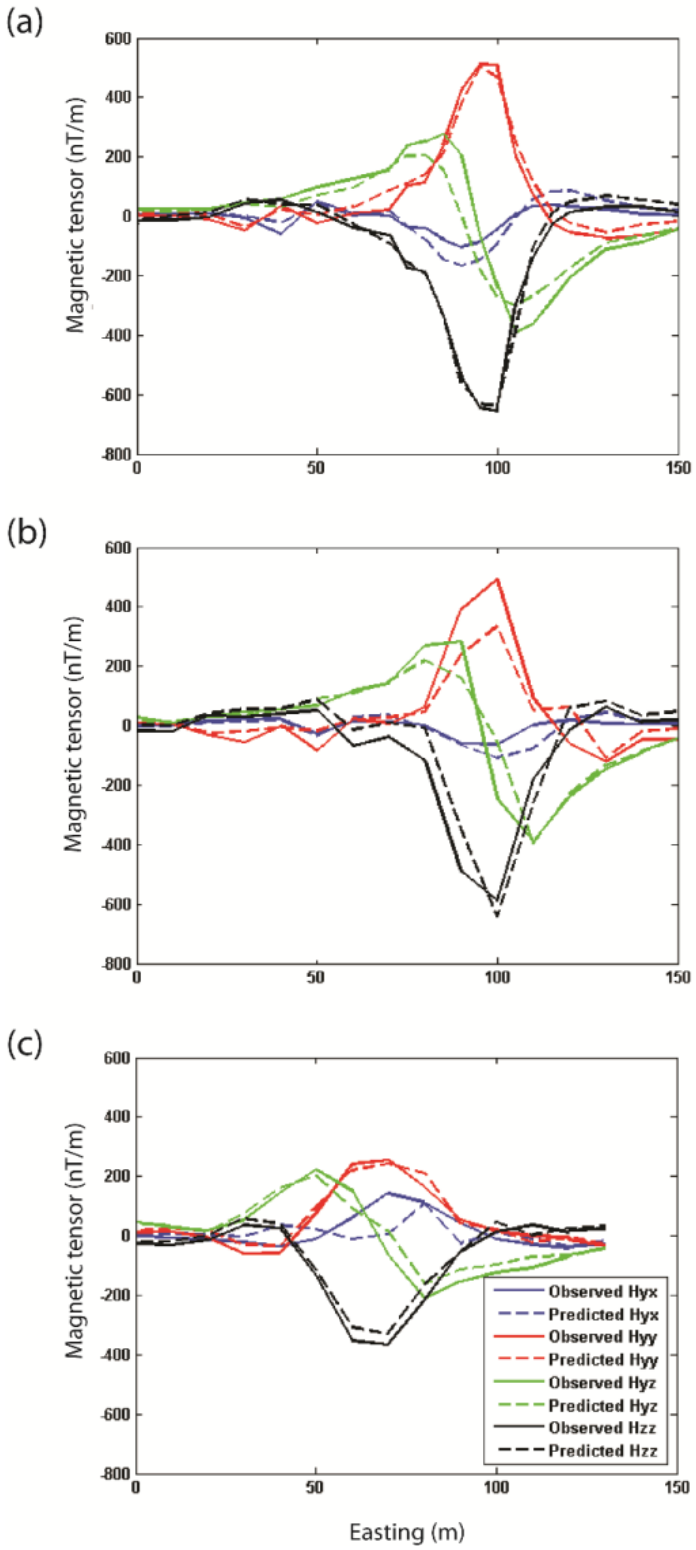

Figure 5.9. Observed (solid lines) and predicted (dashed lines) data for different magnetic tensor components along profiles (a) 50 mN, (b) 60 mN, and (c) 120 mN. The predicted mdata are those obtained from 3-D inversion with minimum norm (smooth) regularization. The misfit between observed and predicted data is 25%.

Figure 5.10a to Figure 5.10d show vertical and horizontal cross sections beneath each of the profiles and at 25 m depth as obtained from 3-D inversion with focusing regularization. Figure 5.10e to Figure 5.10h show vertical and horizontal cross-sections beneath each of the profiles and at 25 m depth, as obtained from 3-D inversion with smooth regularization. Both models satisfy the data to the same misfit, yet we can clearly see how focusing regularizations enables us to recover much sharper boundaries and higher contrasts than smooth regularization. Moreover, as we superimposed the geology which is shown in Figure 5.11, we can see excellent agreement between our focusing inversion results and the known geology where we have sensitivity. From the horizontal section of the inversion result, we can see that the fault over the skarn is still not recovered and the probable reason is that we just have three profiles which have limited sensitivity to the area nearby the fault. The inversion result will be much better if we have more profiles along the deposit.

5.5 Comparison between images produced by migration, smooth inversion, and focusing inversion

We have interpreted the Tallawang magnetic tensor data using 2-D migration, 3-D regularized focusing inversion, and 3-D regularized smooth inversion to obtain the magnetic susceptibility distribution. In this subsection, we will compare some results from these three techniques.

Figure 5.12, Figure 5.13 and Figure 5.14 show the vertical section at the same location obtained from 2-D migration, 3-D regularized focusing inversion and 3-D regularized smooth inversion. One can see that the shapes of the magnetic body

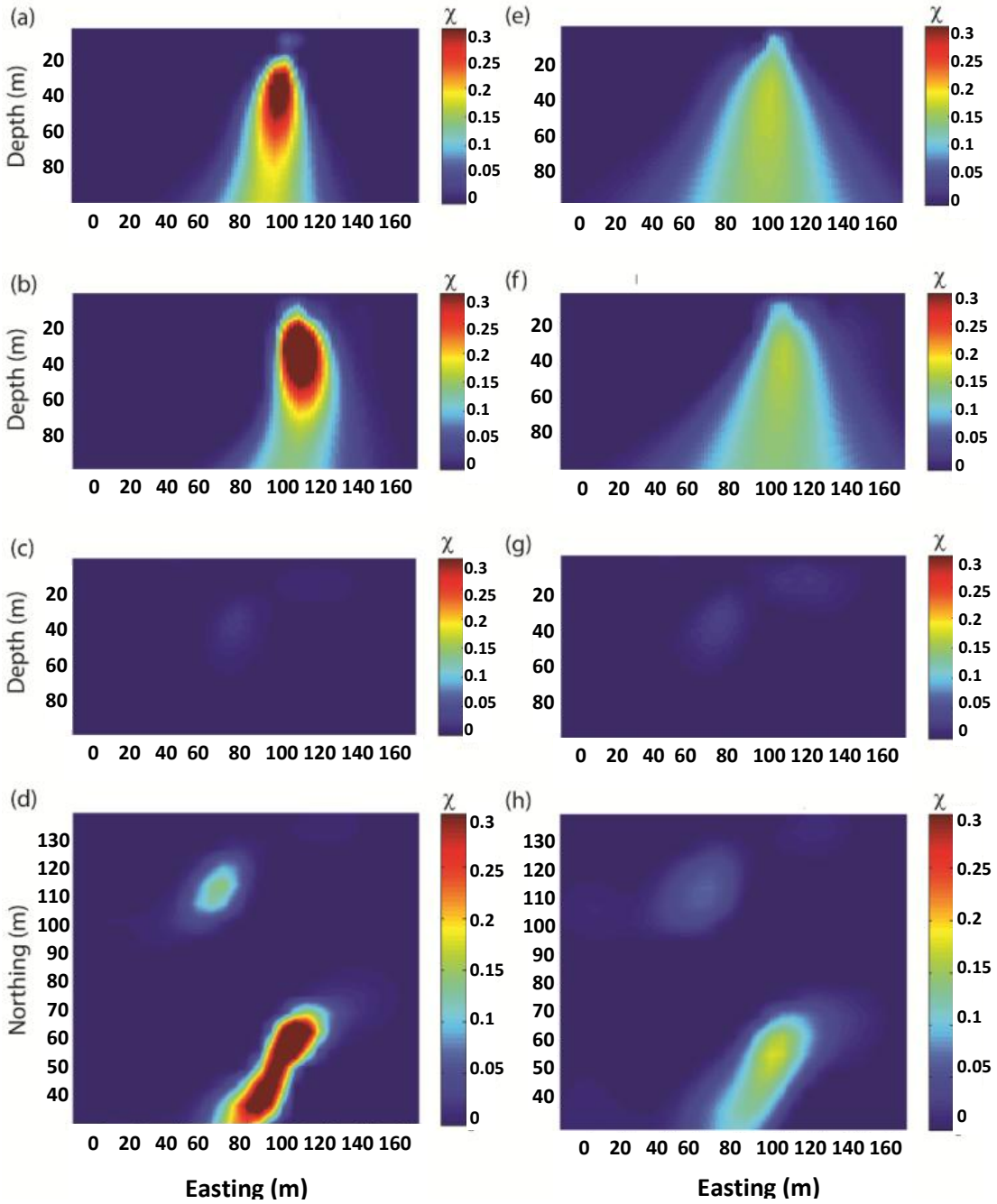

Figure 5.10. Results of 3-D inversion with minimum support (focusing) regularization for vertical cross sections along profiles (a) 50 mN, (b) 60 mN, and (c) 120 mN; and (d) horizontal cross section at 25 m depth. For comparison, results are also shown for 3-D inversion with minimum norm (smooth) regularization for vertical cross sections along profiles (e) 50 mN, (f) 60 mN, and (g) 120 mN; and (h) horizontal cross section at 25 m depth.

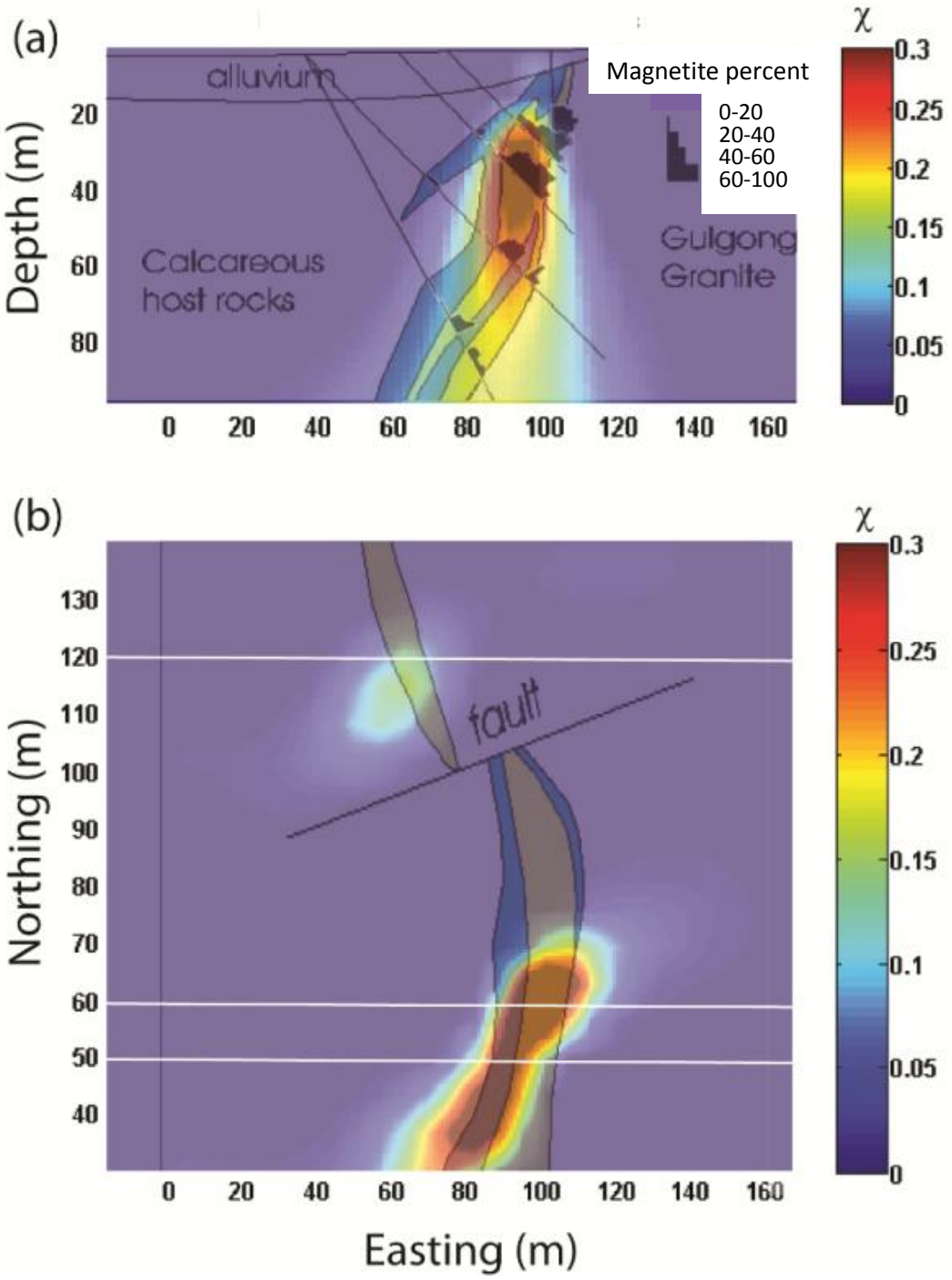

Figure 5.11. Geology of the Tallawang magnetite skarn superimposed on the susceptibility model recovered from 3-D inversion of GETMAG data using minimum support (focusing) regularization for (a) vertical cross section along profile 50 mN, and (b) horizontal cross section at 25 m depth.

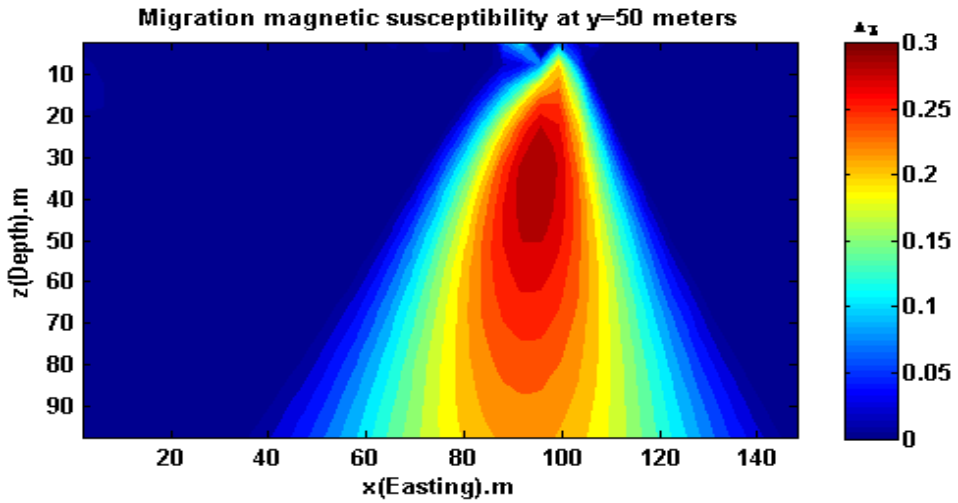

Figure 5.12. Vertical section at y=50 meters of magnetic susceptibility distribution obtained from 2-D migration.

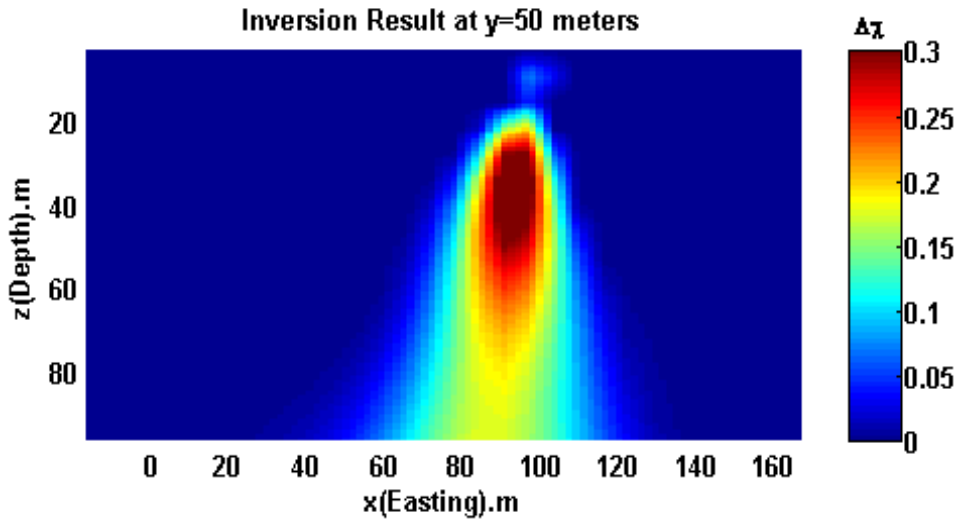

Figure 5.13. Vertical section at y=50 meters of magnetic susceptibility distribution obtained from 3-D regularized focusing inversion.

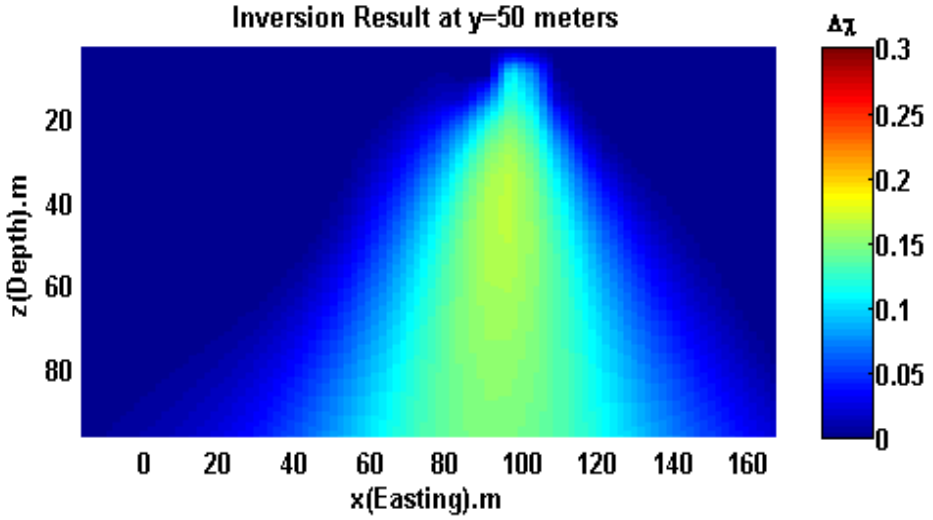

Figure 5.14. Vertical section at y=50 meters of magnetic susceptibility distribution obtained from 3-D regularized smooth inversion.

recovered from these three techniques are similar. Both 2-D migration and 3-D regularized smooth inversion generate smooth image. The images produced by 3-D regularized inversion are much more compact and closer to the real geology than those obtained from both 2-D migration and 3-D regularized smooth inversion.

Among these three techniques, 3-D regularized focusing inversion and smooth inversion are demanding more memory and compute time for the large matrix inversion involved in the inverse process. Both methods take about 25 minutes to get the desirable solution. Two dimensional migration shows high advantage in memory and compute time since it is a direct integral transformation from observed data to the magnetic susceptibility distribution which means that there is no need to compute Frechet derivative matrix which is usually relatively large and the number of cells is limited for a 2-D case. It takes about 10 seconds for each profile to obtain the distribution of migration magnetic susceptibility.

CHAPTER 6

CONCLUSIONS

In this study, we have introduced the theory of 2-D potential field migration and demonstrated its application to the rapid imaging of magnetic vector and tensor field data. We have shown that magnetic migration is equivalent to a special form of downward continuation for the complex conjugate of the observed magnetic fields. The sources of the migration field are a mirror image (with respect to the observational profile) of the true sources. Physically, the migration field can be obtained by moving the sources of the observed magnetic fields above the observational profile, and by then downward continuation the complex conjugate of the observed magnetic field data. The migration field contains remanent information about the original sources, so it can be used for imaging the susceptibility distribution in the subsurface. The remarkable feature of potential field migration is that, contrary to the conventional transforms such as downward continuation or the calculation of higher order derivatives, the method is very stable and produces robust images of subsurface structures.

In addition, the method does not require any a priori information about the type of the source of the magnetic field. We have applied our migration to GETMAG magnetic tensor data collected over a magnetite skarn at Tallawang in New South Wales, Australia, the results of which agree very well with both Euler deconvolution and the known

geology. Magnetic migration can be extended to a 3-D case, and this will be the subject of a subsequent paper.

Besides 2-D migration, we also developed the 3-D regularized focusing inversion algorithm for magnetic vector field and magnetic tensor field data. We also considered topography into synthetic magnetic forward modeling and inverse problem. Several synthetic models were tested for magnetic vector field data and magnetic tensor field data. Our model studies show that the anomalous bodies were recovered both from magnetic vector field inversion and magnetic tensor field inversion. The images produced by the regularized smooth inversion are much more compact than those obtained by the regularized smooth inversion. The inversion of all independent magnetic tensor components can significantly improve model resolution compared to the inversion of magnetic vector components. Our inversion code also shows robust property to recover the anomalous body and fast convergence even in the case of complicated topography.

We have also applied our 3-D inversion to GETMAG magnetic tensor data acquired over a magnetite skarn at Tallawang in New South Wales, Australia. Our results agree very well with the known geology of the area, and show how magnetic gradiometry can significantly improve the practical effectiveness of magnetic methods for exploration. For the GETMAG magnetic tensor data, we did both 3-D regularized focusing inversion and 3-D regularized smooth inversion. The magnetic anomaly was recovered from both regularized focusing inversion and smooth inversion. However, the images produced by 3-D regularized focusing inversion are much closer to the real geology, characterized by sharp boundaries, than those recovered by smooth inversion. In other words, we can say that the application of the regularized focusing inversion is preferable in order to recover

real geology. By comparing 3-D regularized inversion and 2-D migration, we found that migration can be used as a fast imaging technique, which consumes much less memory and compute time. The future work will be focused on 3-D migration of magnetic data to obtain a magnetic susceptibility distribution, which can be used as an initial or an a priori model for 3-D regularized inversion.

APPENDIX A

INTEGRATED SENSITIVITY OF MAGNEITC VECTOR FIELD

Following Zhdanov (2002), the integrated sensitivity of the magnetic vector field is calculated as:

$$s_H = \frac{||\delta H||_D}{|\delta \chi|}, \tag{AI.1}$$

where δH is the perturbation of the magnetic vector field resulting from a local perturbation of magnetic susceptibility. $\delta\chi = \chi(\ )ds$, within a differential element of area *ds*, located at the point $= x + \mathrm{i}z$ of the lower half-plane ($z < 0$):

$$\delta H = \delta H(\ ') = -2\frac{(l_x + il_z)H_0\chi(\ )ds}{(\ - \ ')^2}. \tag{AI.2}$$

Substituting equation (AI.2) into (AI.1), we find:

$$s_H = \frac{1}{|\chi(\ )|ds}\sqrt{\int_L \delta H(\ ')\delta H^*(\ ')d\ '} = 2H_0\sqrt{\int_L \frac{1}{|\ - \ '|^4}d\ '}, \tag{AI.3}$$

where L is a line of observations of the magnetic field. If the line of observations coincides with the horizontal axis, $\mathrm{z}' = 0$, the definite integral in equation (AI.3) can be evaluated as follows:

$$s_H = 2H_0\sqrt{\int_{-\infty}^{\infty}\frac{1}{[(x-x')^2+z^2]^4}d\ '} = 2H_0\sqrt{-\frac{1}{z^3}\int_{-\infty}^{\infty}\frac{1}{[\eta+1]^2}d\eta}, \tag{AI.4}$$

where the tabulated integral is given by

$$\int_{-\infty}^{\infty} \frac{1}{[\eta+1]^2}\, d\eta = \frac{\pi}{2}. \tag{AI.5}$$

Thus, we have:

$$s_H = 2H_0\sqrt{-\frac{1}{z^3}\frac{\pi}{2}} = H_0\sqrt{\frac{2\pi}{|z|^3}}, z < 0. \tag{AI.6}$$

Equation (AI.6) is the integrated sensitivity of the magnetic field to the local magnetization anomaly located at the depth $|z|$ in the lower half-plane ($z < 0$). We can see that the sensitivity is inversely proportional to the square root of the cube of the depth of magnetization.

APPENDIX B

INTEGRATED SENSITIVITYOF MAGNEITC TENSOR FIELD

Following Zhdanov (2002), the integrated sensitivity of the magnetic tensor field is calculated as:

$$s_T = \frac{||\delta H_T||_D}{|\delta\chi|}, \tag{AII.1}$$

where δH_T is the perturbation of the magnetic tensor field resulting from a local perturbation of magnetic susceptibility. $\delta\chi = \chi(\ )ds$, within a differential element of area *ds*, located at the point $\ = x + \mathrm{i}z$ of the lower half-plane ($z < 0$):

$$\delta H_T = \delta H_T(\ ') = -4\frac{(l_x + il_z)H_0\chi(\ )ds}{(\ - \ ')^3}. \tag{AII.2}$$

Substituting equation (AII.2) into (AII.1), we find:

$$s_T = \frac{1}{|\chi(\ )|ds}\sqrt{\int_L \delta H_T(\ ')\delta H_T{}^*(\ ')d\ '} = 4H_0\sqrt{\int_L \frac{1}{|\ - \ '|^6}d\ '}, \tag{AII.3}$$

where L is a line of observations of the magnetic field. If the line of observations coincides with the horizontal axis, $\mathrm{z}' = 0$, the definite integral in equation (AII.3) can be evaluated as follows:

$$s_T = 4H_0\sqrt{\int_{-\infty}^{\infty}\frac{1}{[(x-x')^2+z^2]^3}d\ '} = 4H_0\sqrt{-\frac{1}{z^5}\int_{-\infty}^{\infty}\frac{1}{[\eta+1]^3}d\eta}, \tag{AII.4}$$

where the tabulated integral is given by Gradshtein and Ryzhik (1994, equation 3.249):

$$\int_{-\infty}^{\infty} \frac{1}{[\eta+1]^3} d\eta = \frac{3\pi}{8}. \quad \text{(AII.5)}$$

Thus, we have:

$$s_T = 4H_0\sqrt{-\frac{1}{z^5}\frac{3\pi}{8}} = H_0\sqrt{\frac{6\pi}{|z|^5}}, z < 0. \quad \text{(AII.6)}$$

Equation (AII.6) is the integrated sensitivity of the magnetic tensor field to the local magnetization anomaly located at the depth $|z|$ in the lower half-plane ($z < 0$). We can see that the sensitivity is inversely proportional to the square root of the 5-th order of the depth of magnetization.

APPENDIX C

THE RRCG ALGORITHM IN LOGARITHMIC SPACE

Let's define the forward operator and the corresponding Frechet derivative in the space of logarithmic model parameters as $\mathbf{A_l}$ and $\mathbf{F_l}$.it is easy to see that the following relationship takes place:

$$\mathbf{A_l}\tilde{\mathbf{m}} = \mathbf{Am}. \tag{AIII.1}$$

We take the derivative of equation (AIII.1) with respect to **m** on both sides:

$$\frac{\delta(\mathbf{A_l}\tilde{\mathbf{m}})}{\delta\tilde{\mathbf{m}}} = \frac{\delta(\mathbf{Am})}{\delta\tilde{\mathbf{m}}}. \tag{AIII.2}$$

Equation (AIII.2) can be simplified as

$$\mathbf{F_l} = \mathbf{F}\frac{\delta(\mathbf{m})}{\delta\tilde{\mathbf{m}}}, \tag{AIII.3}$$

where **F** is the Frechet derivative in the space of original model parameters. In the case of linear operator, **F**=**A**.

From equation (4.13), we find:

$$\frac{\delta(m_i)}{\delta\tilde{m}_i} = \frac{m_i^+ - m_i^-}{(1+\exp(\tilde{m}_i))^2}\exp(\tilde{m}_i) = \frac{\Delta m}{(1+\exp(\tilde{m}_i))^2}\exp(\tilde{m}_i). \tag{AIII.4}$$

We can write the last equation using the matrix notation:

$$\frac{\delta(\mathbf{m})}{\delta\tilde{\mathbf{m}}} = \left(I + diag(\exp(\tilde{\mathbf{m}}))\right)^{-2} diag(\Delta\mathbf{m})\exp(\tilde{\mathbf{m}}). \tag{AIII.5}$$

By substituting equation (AIII.5) into equation (AIII.3), we find:

$$\mathbf{F_l} = \mathbf{F}\big(I + diag(\exp(\tilde{\mathbf{m}}))\big)^{-2} diag(\Delta\mathbf{m}) \exp(\tilde{\mathbf{m}}). \quad \text{(AIII.6)}$$

Equation (AIII.6) makes it possible to find the Frechet derivative in the space of the logarithmic model parameters directly if we know the Frechet derivative in the original space.

In the space of the logarithmic model parameters, the Tikhonov parametric functional can be written as follows:

$$P^{\alpha}(\tilde{\mathbf{m}}, d) = (\mathbf{A_l}\tilde{\mathbf{m}} - \mathbf{d})^T(\mathbf{A_l}\tilde{\mathbf{m}} - \mathbf{d}) \; +$$

$$\alpha\big(\mathbf{W}_e\mathbf{W}_m\tilde{\mathbf{m}} - \mathbf{W}_e\mathbf{W}_m\tilde{\mathbf{m}}_{apr}\big)^T\big(\mathbf{W}_e\mathbf{W}_m\tilde{\mathbf{m}} - \mathbf{W}_e\mathbf{W}_m\tilde{\mathbf{m}}_{apr}\big). \quad \text{(AIII.7)}$$

Here

$$\mathbf{W}_e = \mathbf{diag}[w_e] = \mathbf{diag}\left[\frac{1}{(\tilde{m}_i^2 + e^2)^{1/2}}\right], \quad \text{(AIII.8)}$$

and

$$\mathbf{W}_m = \mathbf{diag}(\mathbf{F}^T\mathbf{F})^{1/4}. \quad \text{(AIII.9)}$$

In equation (AIII.7), the misfit part can be calculated in the original model space instead of the space of logarithmic model parameters, since identity (AIII.1) takes place.

Again, let's set

$$\mathbf{W} = \mathbf{W}_e\mathbf{W}_m, \mathbf{m}^w = \mathbf{W}\tilde{\mathbf{m}} = \mathbf{W}_e\mathbf{W}_m\tilde{\mathbf{m}}, \mathbf{A}_\mathbf{l}^w = \mathbf{A_l}\mathbf{W}^{-1} = \mathbf{A_l}\mathbf{W}_m^{-1}\mathbf{W}_e^{-1}$$

and $\mathbf{F}_{\mathbf{l}w} = \mathbf{F_l}\mathbf{W}^{-1} = \mathbf{F_l}\mathbf{W}_m^{-1}\mathbf{W}_e^{-1}$

Then equation (AIII.7) can be rewritten in the space of the weighted model parameters as follows:

$$P^{\alpha}(\mathbf{m}^w, d) = (\mathbf{A}_\mathbf{l}^w\mathbf{m}^w - \mathbf{d})^T(\mathbf{A}_\mathbf{l}^w\mathbf{m}^w - \mathbf{d})$$

$$+\alpha\big(\mathbf{m}^w - \mathbf{m}_{apr}^w\big)^T\big(\mathbf{m}^w - \mathbf{m}_{apr}^w\big). \quad \text{(AIII.10)}$$

The algorithm for reweighted regularized conjugate gradient minimization of parametric functional (AIII.10) in the space of the weighted logarithmic model parameters can be described as follows:

$$\mathbf{r}_n^w = \mathbf{A}_\mathbf{l}^w \mathbf{m}_n^w - \mathbf{d} = \mathbf{A}_\mathbf{l} \tilde{\mathbf{m}}_n - \mathbf{d} = \mathbf{A}\mathbf{m}_n - \mathbf{d}, \quad \text{(AIII.11)}$$

$$\mathbf{l}_{wn}^{\alpha_n} = \mathbf{F}_{lwn}^T \mathbf{r}_n^w + \alpha_n(\mathbf{m}_n^{wn} - \mathbf{m}_{apr}^{wn}), \quad \text{(AIII.12)}$$

$$\beta_n^{\alpha_n} = \| \boldsymbol{l}_{wn}^{\alpha_n} \|_M^2 / \| \boldsymbol{l}_{w(n-1)}^{\alpha_{n-1}} \|_M^2, \tilde{\boldsymbol{l}}_{wn}^{\alpha_n} = \boldsymbol{l}_{wn}^{\alpha_n} + \beta_n^{\alpha_n} \boldsymbol{l}_{w(n-1)}^{\alpha_{n-1}}, \tilde{\boldsymbol{l}}_{w0}^{\alpha_0} = \boldsymbol{l}_{w0}^{\alpha_0}, \quad \text{(AIII.13)}$$

$$k_n^{\alpha_n} = (\tilde{\boldsymbol{l}}_{wn}^{\alpha_n\,T} \tilde{\boldsymbol{l}}_{wn}^{\alpha_n}) / \left[\tilde{\boldsymbol{l}}_{wn}^{\alpha_n\,T} (\mathbf{F}_{lwn}^T \mathbf{F}_{lwn} + \alpha_n \mathbf{I}) \tilde{\boldsymbol{l}}_{wn}^{\alpha_n} \right], \quad \text{(AIII.14)}$$

$$\mathbf{m}_{n+1}^{w_n} = \mathbf{m}_n^{w_n} - k_n^{\alpha_n} \tilde{\boldsymbol{l}}_{wn}^{\alpha_n}, \tilde{\mathbf{m}}_{n+1} = \mathbf{W}_n^{-1} \mathbf{m}_{n+1}^{w_n} = \mathbf{W}_m^{-1} \mathbf{W}_e^{-1} \mathbf{m}_{n+1}^{w_n}, \quad \text{(AIII.15)}$$

$$\mathbf{m}_{n+1}^{w_{n+1}} = \mathbf{W}_{e(n+1)} \mathbf{W}_m \tilde{\mathbf{m}}_{n+1}, \mathbf{s}_{n+1}^{w_{n+1}} = \left(\mathbf{m}_{n+1}^{w_{n+1}} - \mathbf{m}_{apr}^{w_{n+1}} \right) and$$

$$\mathbf{s}_{n+1}^{w_n} = \left(\mathbf{m}_{n+1}^{w_n} - \mathbf{m}_{apr}^{w_n} \right), \quad \text{(AIII.16)}$$

$$\gamma = \left|\left| \mathbf{s}_{n+1}^{w_{n+1}} \right|\right|^2 / \left|\left| \mathbf{s}_{n+1}^{w_n} \right|\right|^2, \alpha_{n+1} = \alpha_n, if\ \gamma \leq 1$$

$$and\ \alpha_{n+1} = \alpha_n / \gamma, if \gamma > 1. \quad \text{(AIII.17)}$$

$$\mathbf{m}_{n+1} = \left(I + diag(\exp(\tilde{\mathbf{m}}_{n+1})) \right)^{-2} (\mathbf{m}^- + diag(\exp(\tilde{\mathbf{m}}_{n+1})) \mathbf{m}^+). \quad \text{(AIII.18)}$$

The above iteration process is terminated when the misfit reaches the given level ε_0:

$$\phi(\mathbf{m}_N) = ||\mathbf{r}_n||^2 \leq \varepsilon_0. \quad \text{(AIII.19)}$$

REFERENCES

Berkhout, A. J., 1980, Seismic Migration-Imaging of Acoustic Energy by Wave Field Extrapolation: Elsevier, Amsterdam.

Bhattacharyya, B. K., 1980, A generalized multibody model for inversion of magnetic anomalies: Geophysics, 29, 517--531.

Claerbout, J. F, 1985, Imaging the Earth's Interior: Blackwell Scientific Publications, Oxford.

Foley, C. P., and K. E. Leslie, 1998, Potential use of High Tc SQUIDs for airborne electromagnetic: Exploration Geophysics, 29, 30-34.

Foley, C. P., K. E. Leslie, R. Binks, C. Lewis, W. Murray, G. J. Sloggett, S. Lam, B. Sankrithyan, N. Savvides, A. Katzaros, K. H. Muller, E. E. Mitchell, J. Pollock, J., Lee, D. L. Dart, R. R. Barrow, M. Asten, A. Maddever, G. Panjkovic, M. Downey, C. Hoffman, and R. Turner, 1999, Field trials using HTS SQUID magnetometers for ground-based and airborne geophysical applications: IEEE Transactions on Applied Superconductivity, 9, 3786--3792.

Gradshtein, I. S., and I. M. Ryzhik, 1994, Table of Integrals, Series, and Products: Academic Press, San Diego.

Lee, J. B., R. J. Turner, M. A. Downey, A. Maddever, D. L. Dart, C. P. Foley, R. Binks, C. Lewis, W. Murray, G. Panjkovic, and M. Asten, 2001, Experience with SQUID magnetometers in airborne TEM surveying: Exploration Geophysics, 32, 9-13.

Li, Y., and D. W. Oldenburg, 1996, 3-D inversion of magnetic data: Geophysics, 61, 394-408.

Li, Y., and D. W. Oldenburg, 1998, 3-D inversion of gravity data: Geophysics, 63, 109-119.

Li, Y., and D. W. Oldenburg, 2003, Fast inversion of large-scale magnetic data using wavelet transforms and a logarithmic barrier method: Geophysical Journal International, 152, 251-265.

Portniaguine, O., and M. S. Zhdanov, 1999, Focusing geophysical inversion images: Geophysics, 64, 3, 874-887.

Portniaguine, O., and Zhdanov, M. S., 2002, 3-D magnetic inversion with data compression and image focusing: Geophysics, 67, 1532-1541.

Rompel, A. K. K., 2009, Geologic applications of FTMG: presented at 11th SAGA Biennial Technical Meeting and Exhibition, Swasiland.

Schmidt, P. W., and D. A. Clark, 1998, The calculation of magnetic components and moments from TMI data - a case study from the Tuckers igneous complex, Queensland: Exploration Geophysics, 29, 609-614.

Schmidt, P. W., and D. A. Clark, 2006, The magnetic gradient tensor - its properties and uses in source characterization: The Leading Edge, 25, 75-78.

Schmidt, P., D. Clark, K. E. Leslie, M. Bick, D. L. Tilbrook, and C. P. Foley, 2004, GETMAG - a SQUID magnetic tensor gradiometer for mineral and oil exploration: Exploration Geophysics, 35, 297-305.

Schneider, W. A., 1978, Integral formulation for migration in two and three dimensions: Geophysics, 43 (2), 49-76.

Stolz, R., V. Zakosarenko, M. Schulz, A. Chwala, L. Fritzsch, H. G. Meyer, and E. O. Kostlin, 2006, Magnetic full-tensor SQUID gradiometer system for geophysical applications: The Leading Edge, 25, 178-180.

Tilbrook, D. L., 2004, The design of a new concept HTSC axial gradiometer: Physica C, 407, 1-9.

Wynn, W. M., C. P. Frahm, P. J. Carroll, R. H. Clark, J. Wellhoner, and M. J. Wynn, 1975, Advanced superconducting gradiometer/magnetometer arrays and a novel signal processing technique: IEEE Transactions on Magnetics, 11, 701-707.

Zhdanov, M. S., 1988, Integral Transforms in Geophysics: Springer-Verlag, New York.

Zhdanov, M. S., 2002, Geophysical Inverse Theory and Regularization Problems: Elsevier, Amsterdam.

Zhdanov, M. S., 2009, Geophysical Electromagnetic Theory and Methods: Elsevier, Amsterdam.

Zhdanov, M. S., X. Liu, and G. Wilson, 2010, Potential field migration for rapid 3-D imaging of entire gravity gradiometry surveys: First Break, 28 (11), 47-51